UNIVERSITY OF CALIFORNIA, SAN DIEGO

Interannual Variability in the North Pacific Ocean from Observations and a Data-Assimilating Model

A dissertation submitted in partial satisfaction of the
requirements for the degree Doctor of Philosophy
in
Oceanography

by

Elizabeth M. Douglass

Committee in charge:

Dean Roemmich, Co-chair
Detlef Stammer, Co-chair
Bruce Cornuelle
Peter Franks
Juan Lasheras
Arthur Miller

2007

The dissertation of Elizabeth M. Douglass is approved, and it is acceptable in quality and form for publication on microfilm:

Co-chair

Co-chair

University of California, San Diego

2007

TABLE OF CONTENTS

LIST OF FIGURES

LIST OF TABLES

ACKNOWLEDGMENTS

I am very grateful to my advisors Dean Roemmich and Detlef Stammer for their help and guidance during my time at Scripps. Dean provided invaluable direction and encouragement throughout the process, particularly with respect to understanding and analyzing the data, while Detlef was helpful as I encountered the obstacles of working with a model. They provided opportunities for me to attend conferences and other experiences such as time at sea, while keeping me focused on the goal of completing this dissertation.

Bruce Cornuelle was always available for discussions about the model, the optimization, and any troubles I might be having, in addition to reinforcing the importance of watching the sun set over the ocean. Art Miller, Peter Franks, and Juan Lasheras, my other committee members, were all helpful in providing comments and encouraging me throughout this project.

Ibrahim Hoteit here at Scripps and Armin Köhl in Hamburg, Germany, provided endless help with the mechanics of running the model, guiding me through the pitfalls of what can be an arduous process. I am extremely grateful for their willingness to listen to my often-confused questions and help make some sense out of the madness. In the same way, John Gilson was able to answer any questions I had with regard to the XBT data and processing. Without their help this dissertation probably would not have been completed.

Many thanks are also due to Phil Moses and Caroline Papadopoulos for providing computer support. Phil made sure I always had disk space and access to the programs I needed on both my work computer and my laptop, while Caroline provided support in my use of the computational resources of the Center for Observations, Modeling and Prediction (COMPAS), and also assisted in use of the the supercomputer used for running the optimization, a resource provided by the National Center for Supercomputing Applications. The importance of their help in this regard cannot be overstated.

Thanks are also due to my officemate of 5 years, Alex Ruane, for always

being available for discussion, whether about science or baseball. Similar thanks go to Sarah Zedler, Jessica Kleiss, Odelle Hadley, and many other Scripps students who make this institution such a great place for science and also fun.

Chapter 2 appears with minor modifications as Douglass, E., D. Roemmich, and D. Stammer, Interannual variability in northeast Pacific circulation, *Journal of Geophysical Research*, **111**, C04001, doi:10.1029/2005JC003015. Copyright 2006 by the American Geophysical Union.

Chapter 3 will be submitted with minor modifications as Douglass, E., D. Roemmich, and D. Stammer, Data-sensitivity of the ECCO state estimate in a regional setting.

Chapter 4 is in preparation and will be submitted as Douglass, E., D. Roemmich, and D. Stammer, Interannual variability in North Pacific heat and freshwater budgets.

This work was supported by ONR (NOPP) ECCO grants N00014-99-1-1049, NOAA Grant NA17RJ1231 (GODAE, Argo) and by the NASA Ocean Surface Topography Science Working Team through JPL Contract 961424. The HR-XBT data were collected through support from NSF Grant OCE00-95248. The participation of many commercial vessels, officers and crew, and SIO shipriders in the HR-XBT program is gratefully acknowledged. Re-analysis surface forcing fields from the National Center for Environmental Prediction/National Center for Atmospheric Research (NCEP/NCAR) are obtained through a computational grant at NCAR. Computational support from the Scripps Observations and Modeling Center (COMPAS) is gratefully acknowledged. Computing resources used in running the optimization were provided by the National Center for Supercomputing Applications. The global state estimates were provided by the ECCO Consortium for Estimating the Circulation and Climate of the Ocean funded by the National Oceanographic Partnership Program (NOPP).

VITA

August, 1978	Born, Des Moines, Iowa
2000	B.S., Magna cum laude, Physics Villanova University
2000-2001	Americorps National Service Minneapolis, Minnesota
2001-2007	Graduate Student Researcher Scripps Institution of Oceanography University of California, San Diego
2007	Doctor of Philosophy Scripps Institution of Oceanography University of California, San Diego

PUBLICATIONS

Douglass, E., D. Roemmich and D. Stammer, Interannual variability in northeast Pacific circulation., *J. Geophys. Res, 111*, C04001, 2006.

Douglass, E., D. Roemmich and D. Stammer, Data-sensitivity of the ECCO state estimate in a regional setting, to be submitted.

Douglass, E., D. Roemmich and D. Stammer, Interannual variability in North Pacific heat and freshwater budgets, in preparation.

FIELDS OF STUDY

Major Field: Physical Oceanography

Studies in Applied Mathematics.
Professor S. Llewellyn-Smith, G. Ierley, and W. Young

Studies in Physical Oceanography.
Professor M. Hendershott, L. Talley, P. Robbins, and D. Roemmich

Studies in Linear and Non-Linear Waves
Professors M. Hendershott, H. Melville, and R. Guza

Studies in Fluid Mechanics
Professor C. Winant

Studies in Geophysical Fluid Dynamics
Professor P. Cessi and R. Salmon

Studies in Data Analysis
Professor R. Pinkel, S. Gille and D. Rudnick

Studies in Biological Oceanography
Professor P. Franks

Studies in Atmospheric Thermodynamics
Professor R. Somerville

Studies in Ocean State Estimation
Professor D. Stammer

ABSTRACT OF THE DISSERTATION

Interannual Variability in the North Pacific Ocean
from Observations and a Data-Assimilating Model

by

Elizabeth M. Douglass
Doctor of Philosophy in Oceanography
University of California, San Diego, 2007
Professor Dean Roemmich, Co-chair
Professor Detlef Stammer, Co-chair

Interannual variability of the volume, heat, and freshwater circulation in the North Pacific Ocean is explored through a joint analysis of observations and the output from a data-assimilating model. High-resolution repeated expendable bathythermograph (XBT) transects provide an observational basis for analysis of transport of volume, heat, and freshwater in the North Pacific. The Estimating the Climate and Circulation of the Ocean (ECCO) Consortium uses the adjoint method to constrain an ocean circulation model with observations, producing dynamically consistent time-varying ocean state estimates. These state estimates provide a context in which the detailed information from the observations can be used for analysis of the mean and variability of ocean circulation.

An initial analysis of volume transport in the Northeast Pacific demonstrates that comparisons between a global ocean state estimate and the data are useful in understanding the large-scale gyre interactions, as well as connections with larger scale signals. To improve the accuracy of the ocean state estimate in the North Pacific, several experiments are performed with the ECCO model in

a regional setting. First, we withhold subsets of the data from the assimilation to emphasize the importance of including all available data in order to obtain an accurate state estimate. Separately, we determine that increasing the weights on the subsurface data increases the accuracy of the subsurface estimate with minimal cost to the accuracy of the surface estimate. This new North Pacific state estimate is used to develop heat and freshwater budgets. A trans-Pacific XBT track defines the southern boundary of a closed region, and in that region the balance between cross-track advective transport and surface fluxes gives an estimate of the time-varying storage of heat and freshwater. The mean estimates of transport and storage compare well with previous research. In addition, estimates of the magnitude of variability are provided. The freshwater budget is found to be relatively stable, while the heat budget has large interannual variability. Connections between the variability of the heat storage in the North Pacific and the El Niño/Southern Oscillation climate signal are found.

1

Introduction

The large-scale circulation of the ocean is a critical component in the global environment. Observing this system and understanding the dynamics governing it on time scales from days to decades is a central aspect of oceanographic research. On time scales of decades, the ocean acts as a heat reservoir, and changes in its heat content are one of the signals of long-term global climate change. On interannual time scales, the climate signal of El Niño is conveyed from its origin in the Tropical Pacific to other locations through oceanic and atmospheric teleconnections. Annually and interannually, ocean circulation affects the distribution of heat and nutrients, which in turn impact biological productivity. The interconnections between ocean circulation and climate underscore the need for a more complete understanding of the dynamics controlling them.

Observations are essential to developing our understanding of these processes. Ocean-going research vessels, autonomous floats, and gliders make *in situ* measurements of temperature, salinity, nutrients, and velocity throughout the water column, while satellites monitor surface properties from space. Spatial and temporal resolution, accuracy, and cost vary widely between systems, and each technique has its place in understanding different aspects of the ocean. The most accurate representation of the ocean state will not come from any one particular dataset, but from a synthesis of all available data into a consistent product which

emphasizes the benefits of each type of data and minimizes its limitations.

Numerical models provide another tool with which to expand our understanding. These range from simple box models of individual processes to global coupled atmosphere-ocean circulation models. Models have the advantage of full temporal and spatial resolution, limited only by computer power. The main disadvantage is that no model is capable of simulating the broad range of temporal and spatial scales on which processes take place in the ocean. As a result, in large-scale simulations of ocean circulation, subgrid-scale processes must be parameterized. Understanding the assumptions inherent in these parameterizations is essential to determining how a models results fit into the broader system.

Ocean state estimation synthesizes observations with numerical models in an attempt to use each to their fullest advantage and produce dynamically consistent, time-varying ocean state estimates. The Estimating the Climate and Circulation of the Ocean (ECCO) Consortium (Stammer et al., 2002a) provides such state estimates. Using a framework built on the MIT general circulation model, and using the adjoint method to constrain the estimate with observations, ECCO has produced dynamically consistent global state estimates with horizontal resolution of 1° and regional estimates with even higher resolution, spanning time periods of up to 50 years (Stammer et al., 2002b, 2003, 2004; Wunsch and Heimbach, 2007; Köhl et al., 2007). The development and analysis of a regional ECCO state estimate for the North Pacific is one of the goals of this dissertation.

In chapter 2, a global, 1° ECCO state estimate is compared with a long-term, high resolution expendable bathythermograph (XBT) dataset in an analysis of the circulation of the Northeast Pacific Ocean. The contrast between model and data estimates of circulation in the region of interest highlights the difficulties of comparing smooth, lower-resolution model output with sparse, point-wise measurements of temperature and salinity in a region of the ocean where subsampled mesoscale features complicate synoptic estimates of ocean structure. Despite these difficulties, similarities between model and data estimates are found in the

structure and variability of the currents in the system and their volume transport. Time-scales, magnitudes, and forcing mechanisms associated with the different modes of variability observed in the region are discussed. This section is an example of the synthesis of the model and the data and the results we can obtain from such a synthesis.

Chapter 3 focuses on the development of the ECCO state estimate and the details of the assimilation process. The relative influence of each type of data is explored by withholding subsets of data from the assimilation and then comparing the resulting state estimates both to the constraining data and to data not used as constraints. The results of these experiments emphasize that excluding data from the assimilation is detrimental to the final result. An additional experiment was performed to determine the merits of adjusting the weights applied to the data. In the ECCO assimilation process, the cost of each type of data is proportional to the number of observations, and the weight associated with those observations. The high spatial and temporal coverage provided by satellites means that the number of surface measurements is much greater than the number of subsurface measurements. Consequently, surface measurements have higher relative influence on the model solution. In our experiment, the weights on the subsurface data are increased in order to increase their relative influence in the assimilation. Because the model has 1° horizontal resolution and does not resolve mesoscale features, the danger of this experiment is the unintentional projection of aliased eddy features onto the large-scale estimation. This could result in unrealistic results either in the state estimate or in the forcing fields associated with it. In this case, however, the increase in weights on subsurface data decreased the model-data misfit, particularly in the subsurface data, without adding unphysical or otherwise unacceptable features to the result. Additionally, this improvement was accomplished without too much loss of accuracy in the surface data. The conclusion of chapter 3 is that an increase in the weights on the subsurface data in the regional model in the North Pacific could produce an estimate to be used for more accurate analysis of

the mean and time-varying dynamics of the North Pacific.

The lessons learned in the previous two chapters are brought together in an analysis of heat and freshwater transport in the North Pacific in Chapter 4. The state estimate used in this section results from the regional assimilation with increased weights on subsurface data developed in Chapter 3. The analysis is similar to that in Chapter 2, expanded to include heat and freshwater transport in addition to volume circulation. The region of analysis is expanded to the full North Pacific, bounded at the south by a trans-Pacific high-resolution XBT transect. By combining model and data estimates of advective transport with surface fluxes, time-varying budgets of heat and freshwater can be calculated. The freshwater budget is relatively stable, but the heat budget has significant variability on time scales of 2-3 years. Further analysis of the dynamics of the heat budget demonstrates connections with El Niño. This analysis of variability from 1992-2004 is more complete than could be performed using data alone. Using state estimation to synthesizing disparate datasets in a dynamically consistent way provides a clear picture of interannual variability on the scale of the full basin, which both falls within range of previous estimates of heat and freshwater transport, and elucidates time-scales and magnitudes of variability which would be more difficult to study without the spatial and temporal coverage provided by the ocean state estimate. Additionally, direct comparisons with the high-resolution XBT transect at the southern boundary of the region provides insight into issues of temporal and spatial aliasing and high-resolution variability which are smoothed in the 1°, monthly model output. This is an example of using observations and a regional model to enhance our understanding of the large-scale circulation, its variability, and possible connections to the larger global environment.

2

Interannual Variability in Northeast Pacific Circulation

2.1 Introduction

The present work investigates the mean state and interannual variability of the circulation of the eastern North Pacific. As shown schematically in Figure 2.1, the eastward-flowing North Pacific Current (NPC) supplies source water for both the subpolar gyre and the subtropical gyre. The Gulf of Alaska and the California Current region are both important upwelling zones with high productivity. A description of the large-scale circulation of the northeast Pacific region is an important step toward understanding the biologically and economically important elements that are imbedded in it.

Historically, coastal processes and their impacts on economically important fisheries have been the focus of much research in the Northeast Pacific (Royer, 1998; Hickey, 1998; Chelton et al., 1982). For example, the collapse of the California sardine fishery in the 1940s resulted in the establishment of the California Cooperative Oceanic Fisheries Investigations (CalCOFI) program (Bograd and Lynn, 2003). This project now provides one of the longest continuous oceanographic time-series available. Other research in the region focuses on the Pacific

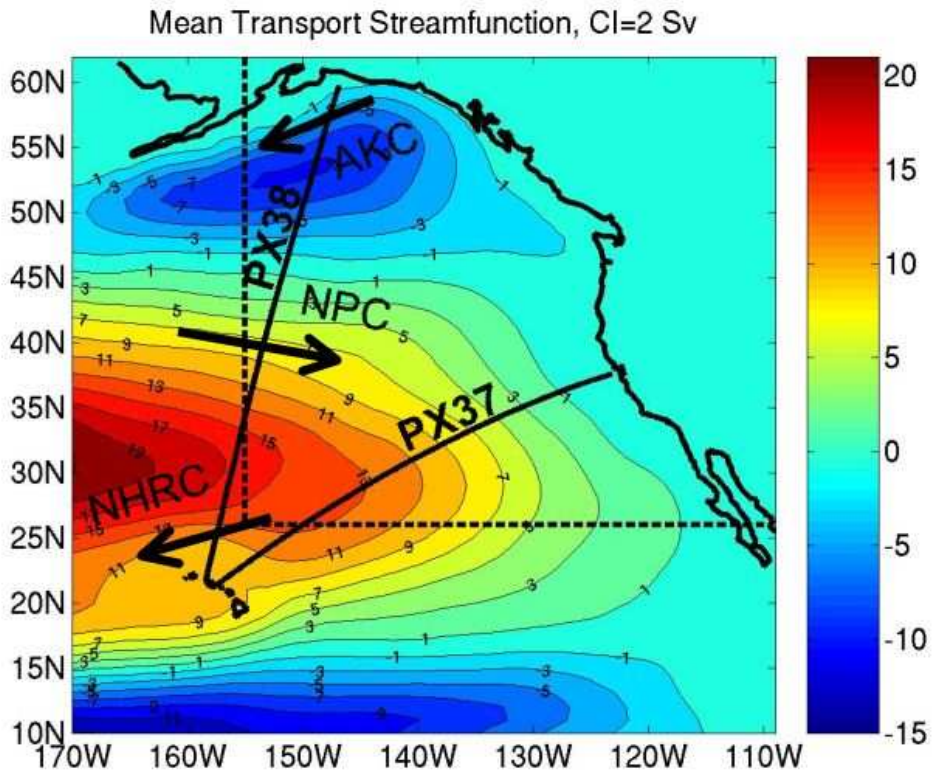

Figure 2.1: Area of study. Shown is the mean transport streamfunction in the top 800 m as it results from the ECCO 1° optimized solution (see text for details). XBT lines, shown as solid, define the edges of the part of the NE Pacific under consideration (the "box"). Line PX37 is from Honolulu, HI, to San Francisco, CA, and line PX38 is from Honolulu, HI, to Valdez, AK. The main components of circulation along PX38 are indicated. These include the North Pacific Current (NPC), Alaska Current (AKC), and North Hawaiian Ridge Current (NHRC). The dashed lines indicate a square box used to estimate the effects of spatial interpolation on the calculations.

Decadal Oscillation (PDO), a large-scale climate phenomenon affecting much of the North Pacific Ocean (Mantua et al., 1997). One motivation for the study of the PDO was the covariability between salmon catches in Alaska and those in Washington and Oregon.

Most previous *in situ* studies in this region consist of individual hydrographic transects or short-term surveys which provide synoptic views of the large-scale circulation (Reed, 1984; Musgrave et al., 1992). These studies provide very little information on long-term variability. The CalCOFI dataset described above has long temporal extent, but its spatial coverage is limited. Another long time series of *in situ* data in this region is a hydrographic line of 13 stations from British Columbia to Ocean Station Papa (located at 50° N, 145° W), known as Line P, which has been occupied regularly since 1959. These data have been used for a variety of studies from short-term observations of El Niño effects (Freeland, 2002) to 25-year analyses of dynamic height variability (Tabata et al., 1986). Like CalCOFI, the spatial extent of Line P is small relative to the two-gyre system considered here.

In a notable study on long-term variability in the northeast Pacific, Chelton and Davis (1982) examined coastal sea level and observed a coherent rise and fall on interannual time scales along the full North American coast. This led the authors to hypothesize "a quasi-permanent transport of the West Wind Drift in the central North Pacific which bifurcates in the eastern North Pacific either with most of the transport turning northward or most of the transport turning southward" as a possible mode of long-term variability in this region. This concept is represented schematically in Figure 2.2(a): the input through the North Pacific Current is constant, but the bifurcation of the transport varies on interannual time scales. Other possible modes of variability are also presented. In Figure 2.2(b), variability in the two gyres (and therefore across the XBT lines) is a direct result of variability in the source waters in the NPC. Changes in the volume of source water are split proportionately between the two gyres; the bifurcation does not change.

In Figure 2.2(c), in the upper layer, transport into the region differs from transport out of the region. In this case, the upper-layer volume changes on interannual time scales, as net volume is either stored in the box or exported from the region.

In this study we examine the circulation of the North Pacific and the connections between the subtropical and subpolar gyres in the context of these interannual modes of variability. The study is based on a joint analysis of observational data and output from a global ocean circulation model constrained by most of the available ocean observations from 1992 to 2002. Each mode of variability will be considered, independently and in combination with the others, in order to determine its relative contribution to the total variability, and to characterize variability in this region as fully as possible.

In situ data, remotely sensed data, and model output are used in this analysis. Each of these contributes to the overall description of the region but has its limitations. *In situ* data provide direct measurements of some aspects of the circulation, at specific times and locations, with known uncertainty. The main dataset here consists of two repeated tracks of XBT data, a zonal section from San Francisco, CA, to Honolulu, HI, and a meridional section from Valdez, AK, to Honolulu, HI. These lines are referred to as PX37 and PX38, respectively (Figure 2.1). Along these lines, spatial resolution is high, but elsewhere, *in situ* measurements are sparse. Remotely sensed data are also available. These data have good spatial and temporal coverage and resolution, but provide information only at the surface; information about the subsurface structure must be inferred indirectly. A third information source, model output, also has good spatial and temporal coverage, but resolution is lower than data. In an attempt to reduce uncertainties, models have been developed that assimilate data while maintaining dynamical consistency. Here, the results from the "Estimating the Climate and Circulation of the Ocean" (ECCO) data assimilation effort (Stammer et al., 2002b) will be used; see Köhl et al. (2007) for a detailed description of the model and the assimilation approach. At this point, uncertainties of the estimates are unknown

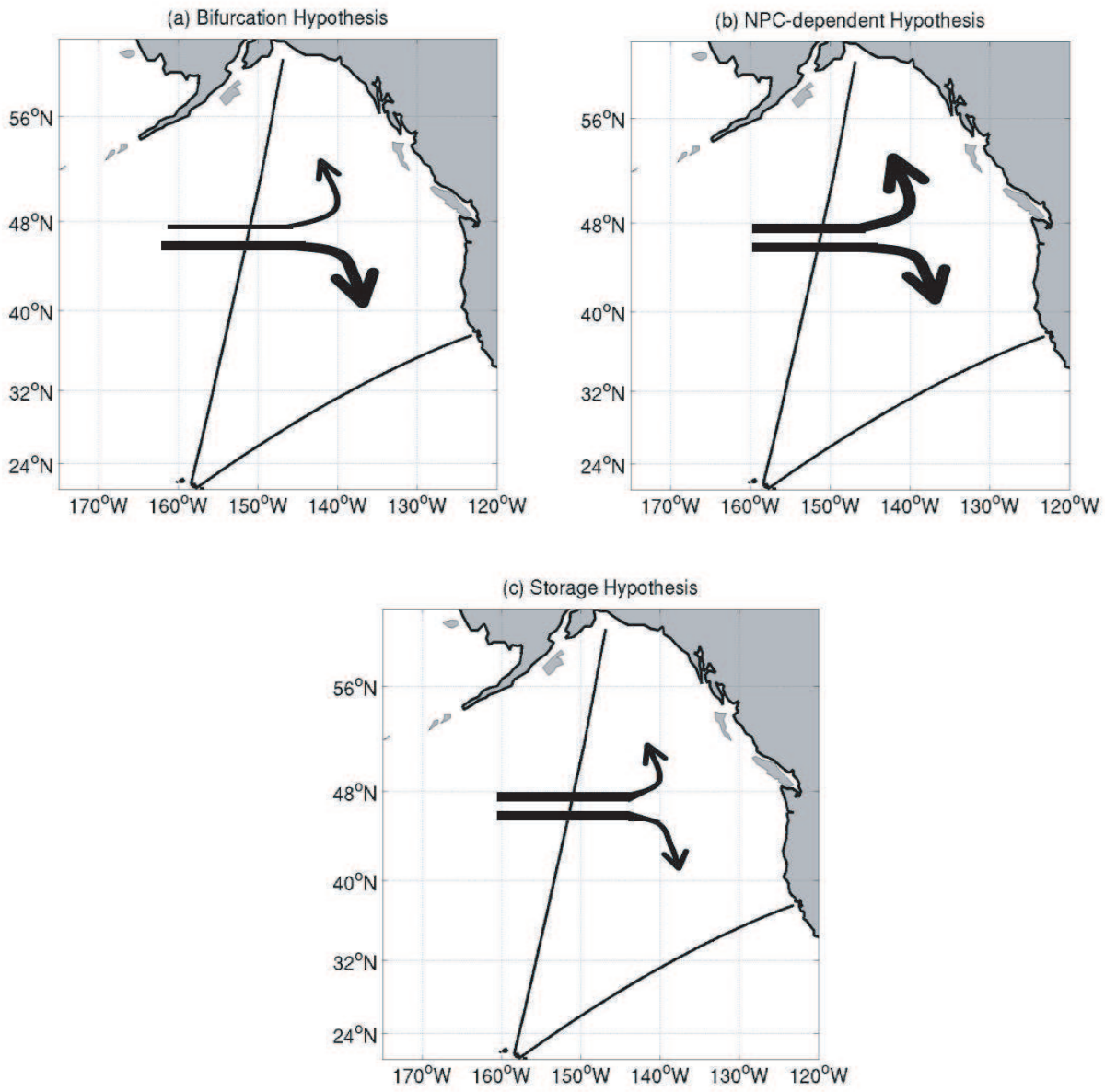

Figure 2.2: Possible modes of variability of the north-east Pacific. In (a), the amount of incoming water remains constant, but the ratio of transport going north to that going south, changes in time; output variability depends on the bifurcation. In (b), the volume of water entering the box changes, and transport in each of the two gyres changes proportionately. In this case the north/south ratio is constant and output variability depends only on input variability. In (c), the volume of upper-layer water leaving the box is not the same as the volume entering the box. In this case upper-layer storage in the box or net outflow occurs.

and difficult to determine, due to limitations in computer resources. One aspect of the present study is therefore to determine the model's skill where observations are available, in order to subsequently use the model to study components of the ocean circulation that are otherwise difficult to observe. For that purpose, the data and the model output are compared within our study region. They are then used in a combined interpretation to obtain the most comprehensive representation of the region's circulation.

The structure of the paper is as follows: in Section 2, we describe the data and model results. Section 3 presents methods of comparing the model output with the data. Section 4 describes the mean state of the circulation as well as its variability, as derived from both model and data. Discussion of the results is in Section 5, and conclusions are presented in Section 6.

2.2 Data and Model

2.2.1 XBT and Satellite Data

The primary *in situ* data source in this analysis is the High Resolution Expendable Bathythermograph (HR_XBT) Program. XBTs are deployed from merchant ships along commercial shipping routes. The data consist of temperature profiles, with a nominal depth of 800 m, having high along-track resolution of 30-50 km in the open ocean and 10 km near boundaries or interesting features, such as the rough topography of the Hawaiian Ridge. The temporal resolution of approximately four cruises per year is only marginally adequate to resolve the seasonal cycle, but should be sufficient to resolve low-frequency variability, with the caveat that temporal aliasing and eddy noise can mask long-period changes. On each cruise, there are occasional expendable conductivity-temperature-depth (XCTD) casts, which provide salinity information for the calculation of density. Their spatial resolution is lower, approximately one cast per 500 km. Processing of all profiles and interpolation onto a uniform grid with resolution of 10 m depth

by 0.1° latitude (for meridional sections) or longitude (for zonal sections), over a depth range of 800 m, is described in detail by Gilson et al. (1998). Data collection began in 1991 on line PX37 and 1993 on line PX38 and continues to the present; data through 2002 are used in this analysis.

Satellite altimetry, which provides high temporal and spatial coverage unavailable from *in situ* data, is also employed in this project. Sea surface height (SSH) has been measured continuously by TOPEX/Poseidon (T/P) since 1992. Precise geoid information is not yet available, so absolute SSH cannot be determined. However, SSH anomaly is well suited for studies of variability. The present study is based on a merged SSH product from T/P, ERS-1, ERS-2, and Jason, provided by Aviso (Ducet et al., 2000). This product is an objective analysis in space and time of all those data sets onto a regular spatial grid with 1/3-degree resolution and a time step of seven days. For our analysis, we created monthly mean fields by averaging the seven-day grids.

2.2.2 Model

The model output used here is obtained by the ECCO Project by constraining the ECCO model with most of the available basin- and global-scale data sets. The goal of ocean data assimilation is to synthesize *in situ* and satellite data with the dynamics embedded in ocean models to obtain the best possible dynamically consistent description of the changing ocean. Stammer et al. (2002b) provide details of the assimilation approach. The assimilation was performed on a global 1° grid over the period 1992 through 2002 by bringing the ECCO model into consistency with the ocean data using the model's adjoint. Data constraints included satellite altimetry, surface drifter velocities, and hydrographic information from conductivity-temperature-depth sensors (CTDs), moorings, and floats (Köhl et al., 2007). In addition, monthly means of temperature and salinity were constrained by the Levitus 1994 hydrographic fields (Levitus and Boyer, 1994; Levitus et al., 1994). The model's initial conditions and daily surface forcing fields were adjusted

to bring the model into consistency with most available datasets. The model drift in temperature and salinity over the 11 year period was also constrained at each grid point to avoid numerical drift away from observed hydrographic conditions.

The ECCO model output used here is provided on a global 1° grid as monthly averages over the 11-year period. Temperature, salinity, sea surface height, and all components of the velocity field are included in the output. Because the surface forcing required to bring the model into consistency with the data is estimated during the assimilation procedure, surface wind stress, heat flux and freshwater flux are also part of the solution. See Stammer et al. (2004) for a discussion of the quality of the estimated surface fluxes.

2.3 Approach

Comparisons between data and model results are an essential step in gaining an understanding of the skill of the model as well as its limitations. However, performing a meaningful comparison is complicated. The inherent differences between what was measured and what the model resolves must be considered. The ocean contains variability from processes taking place on a wide range of spatial and temporal scales, and XBT casts are quasi-synoptic point measurements. In contrast, model fields have 1° spatial resolution; eddies and other mesoscale features are not resolvable on these scales. Temporal variability is further reduced by the use of monthly means. Thus the model fields are significantly smoother than the data in both time and space. In addition, although some drift in temperature or transport might occur in the ocean, constraints reduce the drift in the model. It is important to keep this in mind when evaluating the model's performance against long time-scales in the data (see Köhl et al. (2007) for a detailed discussion of long-term changes in the model).

Velocity is calculated from XBT casts by combining temperature measurements with historical salinity, corrected with XCTDs, to determine density

(see Gilson et al. (1998) for details). Horizontal density gradients are used to calculate cross-track geostrophic velocities, as:

$$-\Phi' = \int_0^p \delta dp = \int_0^p \left(\frac{1}{\rho(S,T,p)} - \frac{1}{\rho(35,0,p)} \right) dp \tag{2.1}$$

$$\begin{aligned} u_g(p) - u_g(p_0) &= \left(\frac{1}{f}\right)\left(\frac{\partial}{\partial x}(\Phi'(p) - \Phi'(p_0))\right) \\ v_g(p) - v_g(p_0) &= \left(\frac{-1}{f}\right)\left(\frac{\partial}{\partial y}(\Phi'(p) - \Phi'(p_0))\right) \end{aligned} \tag{2.2}$$

Here ρ is the density, p is the pressure, and f is the Coriolis parameter. For comparison, model temperature and salinity fields were interpolated onto the same locations as the data. The interpolated model fields were used to calculate geostrophic model velocities, which are directly comparable to the geostrophic velocities calculated from the data. In addition, the model has complete velocity fields that include an ageostrophic component. For each XBT track, the component of model velocity perpendicular to the track was extracted, and compared with the geostrophic velocities calculated from the model and the data. These comparisons reveal both the magnitude of ageostrophic components such as Ekman flow, and the difference between data and model results.

Geostrophic velocities are calculated relative to a "level of known motion" (p_0 in Equation 2.2) of 800 m, the nominal maximum depth of the XBTs. Velocities were calculated relative to zero flow at 800 m, and also relative to model velocity at 800 m. The model's vertical velocity fields were used to determine which of these two calculations resulted in a more physically consistent picture. If upper-layer volume is converging in the box, vertical transport should be downward, out of the box. This would lead to anticorrelation between horizontal and vertical transport. Correlations were higher when the reference velocity was taken from the model fields. As a result, all transports shown below are calculated relative to the model's velocity at 800 m. Figure 2.3 shows the magnitude and variability of the component of transport resulting from the velocity at 800 m.

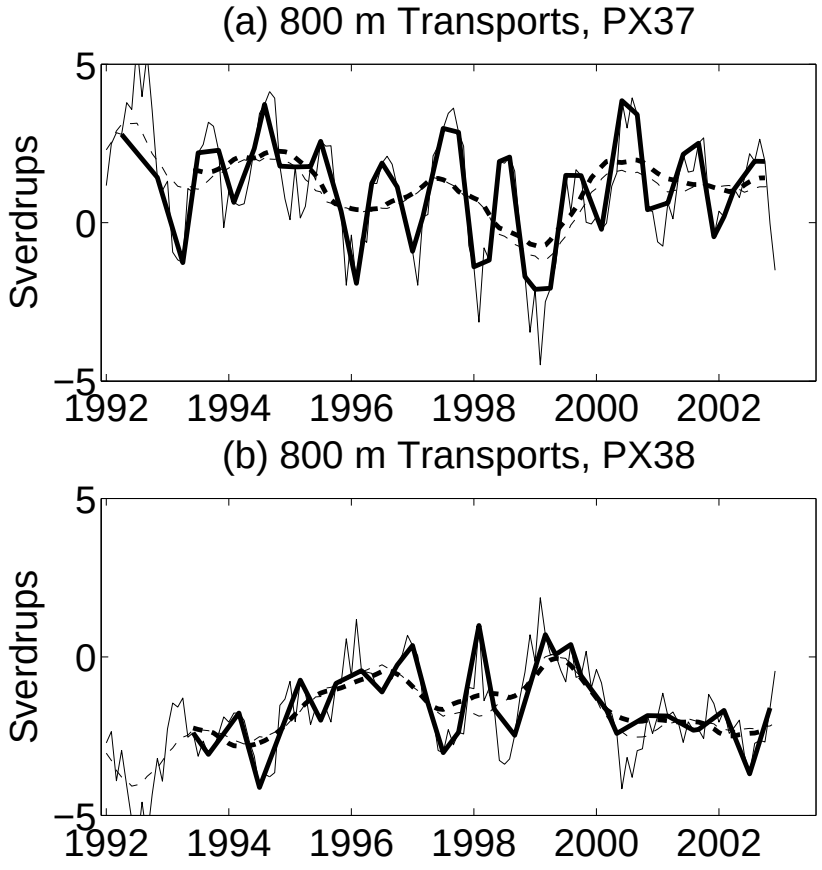

Figure 2.3: Component of transport resulting from using the model velocity at 800 m as a reference velocity instead of zero, across lines (a) PX37 and (b) PX38. In each case, the thin solid line shows the time series of monthly transport estimates. The thick solid line shows the same time series, subsampled at only those months when XBT data are available. The thin and bold dashed lines show the same results for the full and subsampled time series after smoothing using a 12-month running mean.

Ocean velocities and the associated transport can be decomposed into a geostrophic component (T_g), an Ekman component (T_{Ek}), and a residual ageostrophic component (T_a).

$$T = T_g + T_{Ek} + T_a \tag{2.3}$$

The left-hand side (T) can be calculated directly from model velocity fields. However, only the first term on the right-hand side can be determined from the data. Geostrophic volume transport is the flux of volume through an area due to geostrophic velocities.

$$T_g = \int_A \vec{v_g} \cdot \vec{dA} \tag{2.4}$$

The second term on the right-hand side, the Ekman transport (T_{Ek}), can be calculated from the ECCO-estimated wind stress according to:

$$\vec{T_{Ek}} = (T^x_{Ek}, T^y_{Ek}) = (\frac{\tau^y}{\rho f}, \frac{-\tau^x}{\rho f}) \tag{2.5}$$

Here, ρ is seawater density, f is the Coriolis parameter, and τ^y and τ^x are the components of wind stress. For our analysis, the wind stress was interpolated to the XBT lines, the Ekman transport was calculated at each location along the line, and the component of this transport normal to the ship track was subsequently extracted. This cross-track Ekman transport (T_{Ek}) has a magnitude of 1.4±0.65 Sv (1 Sv = 1 Sverdrup = 10^6 m^3/s) on line PX37 and 0.56±0.68 Sv on line PX37. The non-Ekman ageostrophic component of transport (T_a) was computed as the residual that remains after the geostrophic (T_g) and Ekman (T_{Ek}) parts were removed from the total transport (T). T_a is small, with a magnitude of only -0.55±0.36 Sv on line PX37 and -0.16±0.39 Sv on line PX38.

In the remainder of this paper, cross-track volume transports are estimated in three ways for each calculation.

$$T_1 = \int_{-800}^{0} v^m dA \tag{2.6}$$

$$T_2 = \int_{-800}^{0} (v^d_g + v^m(-800)) dA + T_{Ek} \tag{2.7}$$

$$T_3 = \int_{-800}^{0} (v_g^m + v^m(-800))dA + T_{Ek} \tag{2.8}$$

The first estimate, T_1, is based on the cross-track component of the model's full velocity field (v^m). The second estimate, T_2, uses geostrophic velocities from the data (v_g^d), relative to model results at 800 m ($v^m(-800)$), to determine cross-track transport. Ekman transport (T_{Ek}), determined from the model's wind stress, is added to this quantity at each time step. For the final estimate, T_3, geostrophic velocities calculated from model output (v_g^m), relative to model results at 800 m, are used to estimate transport. As with the estimate from data, an Ekman component is added.

Model output is linearly interpolated in space to the locations of the XBT casts using the month closest to the time of the observations. During the comparisons of results from the model and the data, only those months when XBT data are available are considered. During 1992-2002, 42 sections along line PX37 and 30 sections along line PX38 were recorded. Although the cruises are approximately evenly spaced in time, it is possible that some features of the flow are misrepresented or missed entirely as a result of the low sampling rate. An estimate of temporal aliasing in the XBT dataset can be obtained by comparing the full time series of model output with the same time series subsampled at the months when data are available. In general, the main features of the time series are retained by the subsampled series. We note, however, that this estimate does not include the effects of mesoscale eddies.

Since this analysis is focused on interannual variability, it is helpful to accentuate lower frequencies by filtering out higher frequency components. Monthly estimates were produced through linear interpolation of the data and high-frequency variability was subsequently removed with a 12-point running filter. Model output was processed the same way: it was subsampled to the months when XBT data are available and smoothed with a 12-month filter. The following discussion will be based on those smoothed results.

2.4 Circulation

Figure 2.1 shows the mean transport streamfunction in the top 800 m, as calculated from model output. Transport from the full model velocity field is integrated across the region, relative to zero at the coast, according to

$$\Psi(x,y) = \int_{coast}^{y} T_u(x,y')dy' = -\int_{coast}^{x} T_v(x',y)dx' \tag{2.9}$$

The streamfunction is computed over all months when XBT data are available during the eleven-year period covered by the model, 1992-2002. The expected two-gyre structure is evident, with the eastern half of the anti-cyclonic subtropical gyre covering the basin between latitudes of about 15° N and 45° N, and the cyclonic subpolar gyre mostly contained within the Gulf of Alaska. About 15 Sv are transported by the subtropical gyre, while the subpolar gyre carries about 9 Sv. Because transport from the XBT data can only be computed across ship tracks, the spatial structure depicted in the figure cannot be compared to data directly. Comparisons are limited to cross-track transports.

Figure 2.4 shows upper-layer (0 - 800 m) cross-track volume transport as a function of time. Transport across line PX38 (around 9 Sv), transport across line PX37 (around -9 Sv), and total lateral transport into the box (PX37+PX38) are shown. Each quantity is estimated from the full model field, from the data using geostrophy, and from the model using geostrophy (see eqs. 2.6-2.8). Positive values indicate flow into the box (northward flow across PX37 or eastward flow across PX38). The large magnitude of interannual variability in the region is apparent. Net transport across PX38 is positive, dominated by the eastward-flowing NPC, while net transport across PX37 is negative, dominated by the subtropical gyre exporting water from the region. Data-based estimates of the time-mean gyre transport determined from cross-track transports give results similar to those from the model transport streamfunction in Figure 2.1: about 18 Sv in the subtropical gyre and about 9 Sv in the subpolar gyre. The net upper layer transport into the box estimated from the full velocity fields has a mean value of 1.03 Sv and a

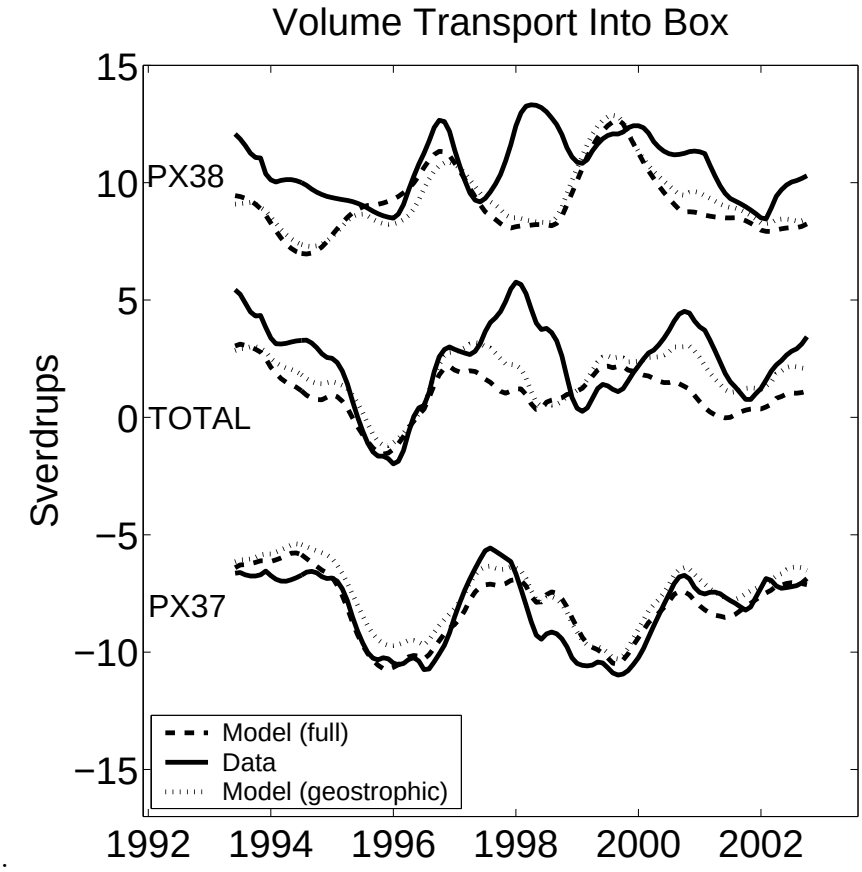

Figure 2.4: Volume transport into the box. The top three lines are different transport estimates across PX38 above 800 m, the bottom three lines are respective transport estimates across PX37, and the middle three lines are the net transport estimates above 800 m into the box. Dashed lines are transport estimates resulting from the model full velocity fields, solid lines represent estimates from geostrophic velocities calculated from data, and dotted lines are transport estimates based on geostrophic velocities calculated from the model. All geostrophic estimates use the model's velocity as a reference level at 800 m. Ekman transport, calculated from model wind stress, has been added to the geostrophic estimates of transport and are part of the full model estimates as well.

standard deviation of 1.02. The downwelling of -1.00±0.88 Sv calculated from the model's vertical velocity fields confirms that in the time-mean, volume is balanced in the box. Geostrophic estimates of horizontal transport are significantly larger: 2.39 ± 1.79 Sv in the data, and 1.73 ± 1.09 Sv in the model. This suggests that the full flow fields are required for budget estimates.

Across line PX37, geostrophic upper-layer transport in the model closely matches that in the data, with a root-mean-square (RMS) difference of 0.88 Sv. The estimate from the full model velocity also agrees well with the data, with an RMS difference of 0.77 Sv. In contrast, there are substantial differences between model- and data-based transport estimates across PX38. The geostrophic model estimate is slightly closer to the data (RMS difference of 1.91 Sv) than the estimate using the full velocity field (RMS difference of 2.08 Sv). A local minimum in the model estimate in 1994 is not seen in the data, while a peak in the data estimate during 1998 is entirely missing from the model estimates. These disparities result in large differences in total transport.

In order to examine the differences between the data and the model along line PX38, we divided the line into three segments, distinguished by the direction of flow (see Figure 2.1), and calculated transport for each section. The northernmost section is the Alaska Current (AKC). This westward-flowing current, north of about 54^oN, is the upper arm of the subpolar gyre. South of the AKC, the North Pacific Current (NPC) is the broad section of eastward flow. The lower boundary of the AKC, defined as the point separating westward AKC flow from eastward NPC flow, is constant in time. The flow turns west again south of about 30^oN, in the North Hawaiian Ridge Current (NHRC). To find the boundary between the NHRC and the NPC, transport was integrated along the track, starting from Hawaii. The minimum in integrated transport marks the point where the currents change from flowing westward to flowing eastward, and thus, the southern edge of the NPC. This location is highly variable, especially for data estimates of transport. If the boundary between the NPC and the NHRC is not determined

correctly, discrepancies could appear in the transport estimates that do not reflect the information in either the data or the model.

Figure 2.5 shows transport estimates for all three sections. In the AKC, shown in Figure 2.5(a), there is reasonable agreement between model and data results. Both tendency and magnitude agree for most of the time series. The RMS difference between the data and model geostrophic estimates is 0.56 Sv, and instantaneous differences rarely exceed one Sverdrup. This region shows the largest differences between the estimate from the full model field and the model geostrophic estimate, indicating the local importance of friction terms.

Differences are larger in the NPC (Figure 2.5(b)). The main difference between the estimates is that the magnitude of the data estimate is approximately 4 Sv larger than either model estimate. The slopes are similar throughout the time series, and all three estimates capture a large increase in transport between 1995 and 1999. The standard deviation of the difference between the model geostrophic estimate of transport and the data estimate is 0.81 Sv. The large bias but small standard deviation suggests that there is no fundamental difference between model and data in the structure of variability. Details of the location of the boundaries between the currents could lead to the bias.

In the southernmost segment of PX38, the NHRC, both a bias and a structural difference are evident (Figure 2.5(c)). The data estimate is biased high, by approximately 2 Sv. It is interesting to note that in this case, as in the NPC, the magnitude of the data estimate is larger than the magnitude of the model estimates. However, when the sum of NHRC and NPC transport across PX38 is considered, the magnitudes of data and model estimates are similar (see Figure 2.4). Unlike the NPC, the slopes of the estimates do not match for the NHRC. The most significant discrepancy occurs in 1998, when the magnitude of transport surges in the model estimate but decreases sharply in the data estimate. We note that it is this discrepancy in the NHRC estimate that leads to the large difference between model and data estimates of total transport (see Figure 2.4). In this

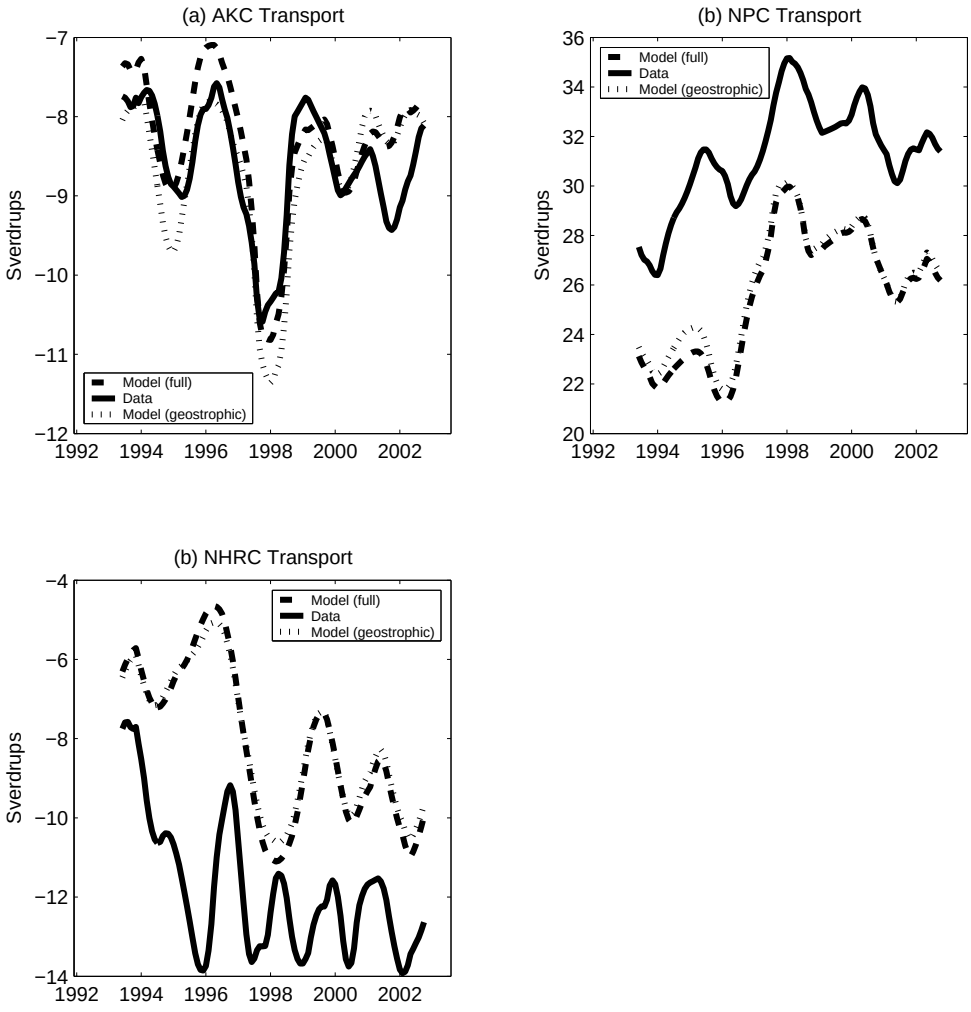

Figure 2.5: Volume transport above 800 m across the three sections of PX38. (a) is the transport through the Alaska Current (AKC), (b) is the North Pacific Current (NPC) and (c) is the North Hawaiian Ridge Current (NHRC). See Figure 2.1 for the location of these currents. Dashed lines are transports estimates resulting from the full model velocity fields, solid lines are based on geostrophic + Ekman transport from data, and dotted lines represent geostrophic + Ekman transport from model output.

region, the synoptic nature of *in situ* data could have a large effect on data-based estimates. Previous observations have demonstrated that "the NHRC appears and disappears on timescales of less than one month" (Bingham, 1998). As a result, in this region, monthly means may not be adequate for comparisons with synoptic data. In addition, complex small-scale dynamics occur in this region as a result of the rough topography of the Hawaiian ridge that are not resolved by the model's one-degree grid.

2.5 Modes of Variability

It is evident that there is strong variability in the upper-layer circulation in this region. In order to explore the variability and possible covariability of the two gyres, we compare their transports (Figure 2.6). For this comparison, the subtropical gyre is defined as the sum of the transport across PX37 and the transport across the southernmost segment of PX38 (the NHRC). The subpolar gyre consists of the AKC segment of PX38. Since the NPC transport contributes to both gyres, and its bifurcation is undetermined and possibly variable, it is not included in either gyre. In this way, it is possible to distinguish changes in the gyres from changes in the NPC. All estimates in Figure 2.6 show large variability. In the subpolar gyre, data and model estimates are similar, but in the subtropical gyre there are significant differences. Data estimates of the gyres are uncorrelated with each other, but there are weak positive correlations between the gyres in both the model geostrophic estimate (r=0.24) and the full model estimate (r=0.44). This indicates a relationship between the gyres in the model that is fundamentally different than the relationship in the data.

One possible mode of variability, illustrated schematically in Figure 2.2(a), assumes a constant NPC, and attributes the variability of transport in the gyres to changes in the bifurcation of the incoming flow. This would lead to anticorrelation between the two gyres; an increase in southward transport would correspond to

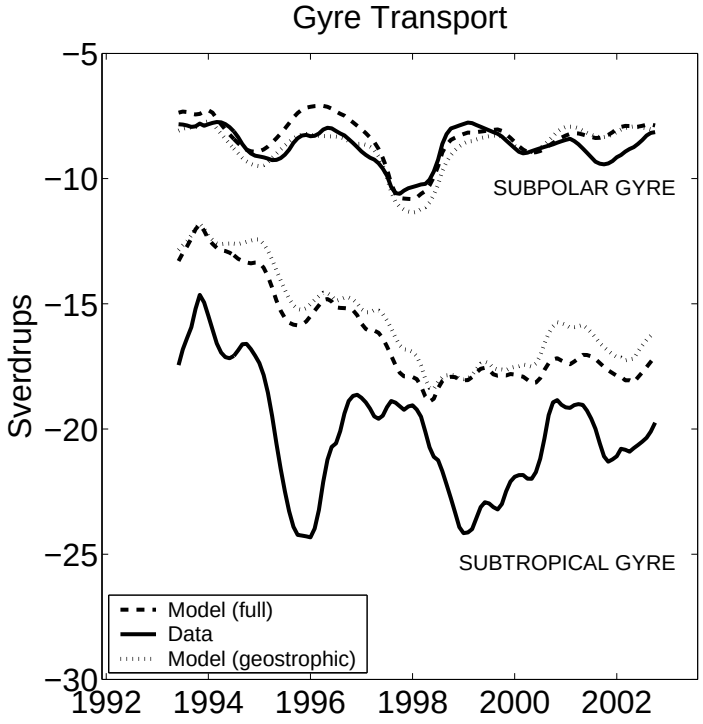

Figure 2.6: Estimates of volume transports in the subpolar gyre (AKC) and the subtropical gyre (PX37+NHRC). The solid lines are the estimates from the data, the dashed lines are the estimates from the model velocity fields, and the dotted lines are the estimates from model geostrophic velocities.

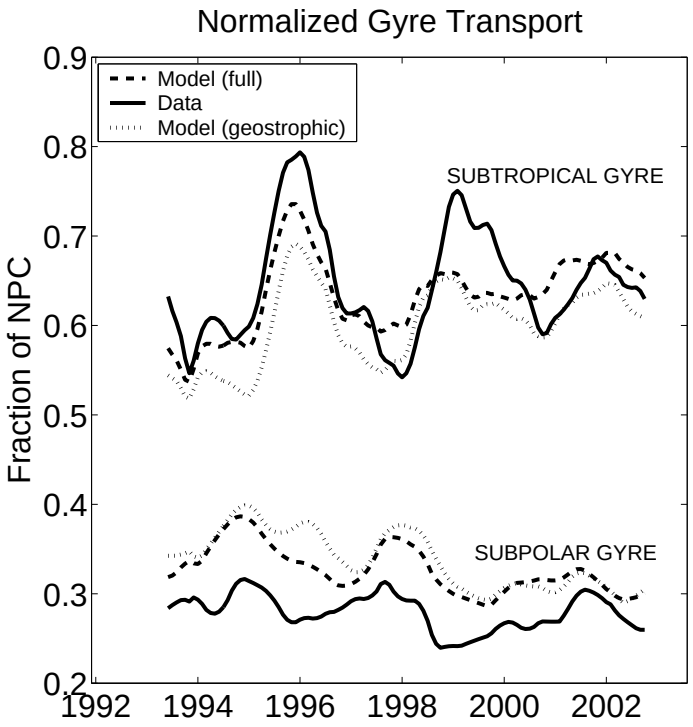

.

Figure 2.7: Similar to Fig. 2.6, but showing the gyre transports which have been normalized by the amount of the instantaneous incoming transport (the NPC). Dashed lines represent model estimates from the full velocity fields, solid lines indicate data estimates, and dotted lines indicate model geostrophic estimates. As before the Ekman transports were added to the geostrophic estimates.

a decrease in northward transport. Although the NPC is not constant, its bifurcation can still modulate the gyre transports. In order to isolate the effect of the bifurcation, the transport in each gyre must be normalized by the magnitude of the NPC at each time step.

Figure 2.7 shows the normalized gyre estimates, or equivalently, the fraction of NPC transport in each gyre. Correlation coefficients of these time series are -0.54 in the data, -0.39 in the full model, and -0.34 in the geostrophic model. This negative correlation in all cases indicates that a change in bifurcation is occurring. The time scale of the variability is approximately 4 years. The anticorrelation is most evident in late 1997, when a significant El Niño event occurred in the tropical Pacific. A minimum in the normalized subtropical gyre transport, shown in

Table 2.1: Correlations between Normalized Gyre transports and the SOI

	Subpolar gyre	Subtropical gyre
Model (full)	0.65	-0.57
Model (geostrophic)	0.51	-0.70
Data	0.76	-0.65

Figure 2.7, is in agreement with previous studies of transport in the California Current that associate El Niño events with decreased horizontal circulation (Chelton et al., 1982). Previous studies of El Niño connections with the subpolar gyre have been inconclusive (McGowan et al., 1998), but Figure 2.7 shows a concurrent peak in normalized subpolar transport. To determine the extent to which the present analysis supports a connection between the bifurcation of NPC transport and El Niño, correlation coefficients were calculated between the Southern Oscillation Index (SOI), a pressure-based index which is related to the El Niño signal (Trenberth and Shea, 1987), and the normalized gyre transports (see Table 2.1). In both gyres, all estimates show significant correlation.

Gyre transports could also covary with the magnitude of the incoming NPC transport (Figure 2.2(b)): the transport in each gyre would increase when the incoming transport increased. Figure 2.8 shows the magnitude of the transports of the NPC (the incoming flow) and of each of the gyres. As in previous plots, the estimates of the subpolar gyre transport agree fairly well. Data estimates for NPC transport and subtropical gyre transport are greater than the model estimates for the same quantities. In the NPC, the difference is a simple bias, but in the subtropical gyre there is substantially more variability in the data estimate than in either model estimate. However, even in the data estimate, a long-term upward trend is evident in both the subtropical gyre and the NPC. Correlation is apparent between the NPC and the subpolar gyre as well: the main signal in the subpolar gyre is a peak in 1998 which also appears in the NPC. The correlations of NPC with gyre transports are shown in Table 2.2.

The most significant signal in this time series is the long-term increase in

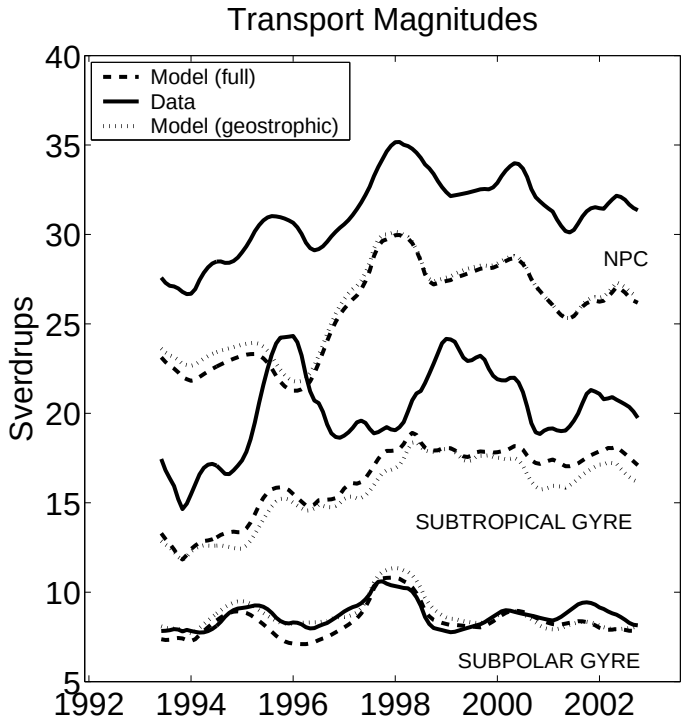

Figure 2.8: Magnitudes of the incoming NPC transport as well as the two gyres (subtropical and subpolar). Dashed lines show results based on the total model velocity field estimates. Solid and dotted lines show data- and model-based geostrophic estimates, respectively. Ekman transport has been added to both geostrophic estimates.

Table 2.2: Correlations between gyre transport magnitudes and the magnitude of the NPC

	Subpolar gyre	Subtropical gyre
Model (full)	0.85	0.71
Model (geostrophic)	0.81	0.54
Data	0.58	0.57

NPC transport. This robust signal is observed in all three estimates of transport (see Figure 2.5(b)), and indicates changes on time-scales longer than the 4-year signal in the bifurcation. Previous research has suggested the possibility of decadal variation in this region (e.g. McGowan et al. (1998) and Chelton et al. (1982)), and the increase in NPC could support these theories. Figure 2.9 shows the transport streamfunction, from the model, averaged over the two time periods 1992-1995 and 1999-2002. The subtropical gyre is significantly stronger in the latter period, but the subpolar gyre remains essentially unchanged. The change in streamfunction is shown in Figure 2.9(c).

For a region in Sverdrup balance, the vertically integrated mass transport can be calculated from the curl of the wind stress as:

$$Hv = \int_{coast}^{x} \frac{1}{\rho\beta}\left(\frac{\partial Y_s}{\partial x} - \frac{\partial X_s}{\partial y}\right) dx \tag{2.10}$$

Here X_s and Y_s are the zonal and meridional components of wind stress, respectively. Using Equation 2.10, the difference in Sverdrup transport between the two time periods was determined. The result is shown in Figure 2.9(d). The similarities between Figures 2.9(c) and 2.9(d) support the hypothesis that the large-scale changes in the model's transport streamfunction are largely due to long-term changes in the local wind forcing of the east North Pacific.

The modes of variability described so far have been based on the premise that mass is constant in the upper layer of the box, so that the transport out of this layer must be the same as the incoming transport. However, if mass were stored in the upper layer, the variability of outgoing transport would be independent of the incoming volume, as in Figure 2.2(c). This possibility can be explored by considering SSH. There are two processes that contribute to SSH variability: changes in steric height, which result from density changes; and changes in mass storage in a region, i.e., uncorrelated to any density change. Steric height changes (Δh) are determined as:

$$\Delta h = \frac{1}{g}\int_{-H}^{0} \delta(T, S, p) dp \tag{2.11}$$

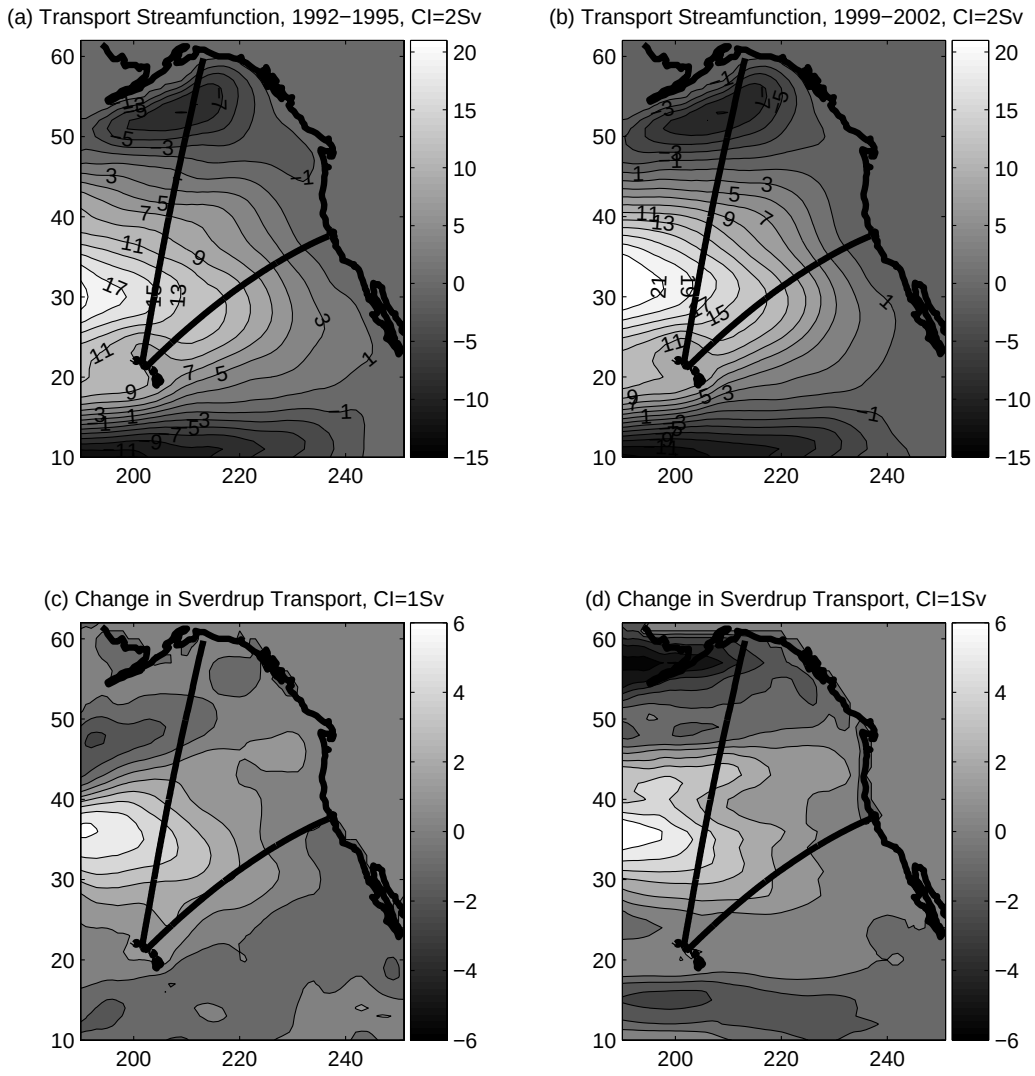

Figure 2.9: Four-year averages of streamfunction representing the period (a) before (1992-1995) and (b) after (1999-2002) the change in NPC. The difference between streamfunction estimates is shown in (c). Panel (d) shows the difference in Sverdrup transport as it results for the same periods, using ECCO wind stress estimates, smoothed over 6 degrees latitude

Here g is gravitational acceleration (9.8 m s^{-2}), δ is specific volume anomaly, and p is pressure. Figure 2.10 shows a time series of steric height anomalies, from the top-to-bottom model field, averaged over the wedge-shaped region shown in Figure 2.1. SSH from the model output and from Aviso data are also plotted. Interannual variability of more than 3 cm is apparent. The high correlation between steric height and SSH shows that changes are mainly due to density variability rather than mass storage. An exception can be found in 1997, when the SSH anomaly as measured by the model and by Aviso is almost a centimeter higher than steric height anomaly would suggest, indicating net mass storage in the box. We note that in this region, the model's density is more strongly dependent on salinity than temperature: the correlation between a time series of halo-steric height and steric height is -0.92 (higher salt leads to higher density which leads to lower steric height), while the correlation between thermo-steric height and steric height is only 0.31. A comparison with *in situ* data from Line P confirms that the salinity signal in the model has skill and suggests the need for more *in situ* salinity measurements to study the North Pacific and to constrain models.

Figure 2.4 shows that the total time-mean horizontal upper-layer transport into the box is not zero. The downwelling transport, calculated from the model fields of vertical velocity, accounts for -1.00±0.88 Sv of transport. When this is added to the horizontal transport, the result is a net inflow of 0.02±0.61 Sv. In the model, then, horizontal transport into the box in the upper layer is balanced by vertical transport into a deeper layer and then horizontal deep transport out of the region. As Figure 2.4 illustrates, the temporal variability of this process is strong. The question of how this variability propagates into the deeper layers of the ocean can be considered using the model's velocity fields. When the transport is calculated for the full depth of the ocean, following the same process of subsampling to XBT months, interpolating, and then using a 12-point filter, the transport into the box is 0.34±2.3 Sv. The large variability of this quantity is surprising. If, instead of subsampling, all months of model output are used, the transport into

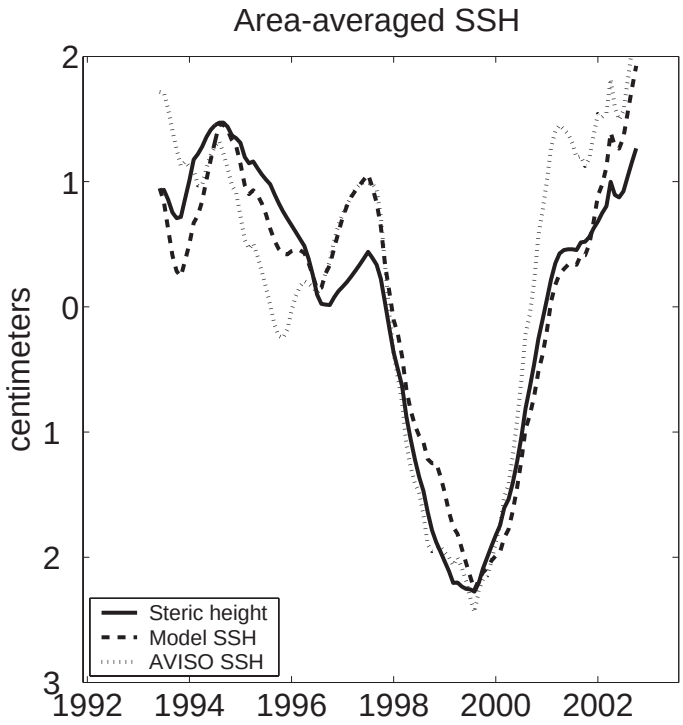

Figure 2.10: Estimated steric height (solid line) calculated from model temperature and salinity fields over the full model depth and averaged over the box. Also shown are spatial averages of the model's SSH (dashed line) and of T/P SSH observations (dotted line). For each estimate, a time-mean was removed.

the box is -0.88±0.77 Sv. The reduced variability, signified by low standard deviation, illustrates that the subsample-and-interpolate method used throughout this analysis has the potential to exaggerate some signals and minimize others. This possibility, an effect of aliasing, cannot be corrected. There is still a slight negative bias in the full time series calculation. If the wedge defined by the XBT lines is replaced by a square box, such as that outlined in dashed lines in Figure 2.1, the need for spatial interpolation of the velocity vectors is eliminated, and the time-mean transport into the box decreases to 0.1±0.02 Sv. These results emphasize that caution must be used when drawing conclusions about the nature of variability from data without including model information, or from model output without validation of data.

2.6 Conclusions

The objective of this work was to analyze high resolution datasets together with a coarser resolution data assimilating model in order to provide an improved description of the mean and time-varying circulation of the Northeast Pacific from 1992-2002. Both the model and the data agree in that, on average, in the upper 800 m, about 25 Sv flow eastward in the North Pacific Current between latitudes 30° N and 52° N. This broad eastward current bifurcates west of the North American coast along 47° N. About 8 Sv turn north and follow the coastline of the Gulf of Alaska into the Alaskan Current, while the remaining 17 Sv turn south and then west in the subtropical gyre. The broad gyre circulation reaches as far south as 15° N, where it joins the North Equatorial Current. The flow that recirculates north of Hawaii is referred to as the North Hawaiian Ridge Current. This current has an average magnitude of about 9 Sv, but its standard deviation is 2.5 Sv, or more than 25% of the magnitude of the flow, indicating very high variability.

The largest interannual signal observed during this period, and also simu-

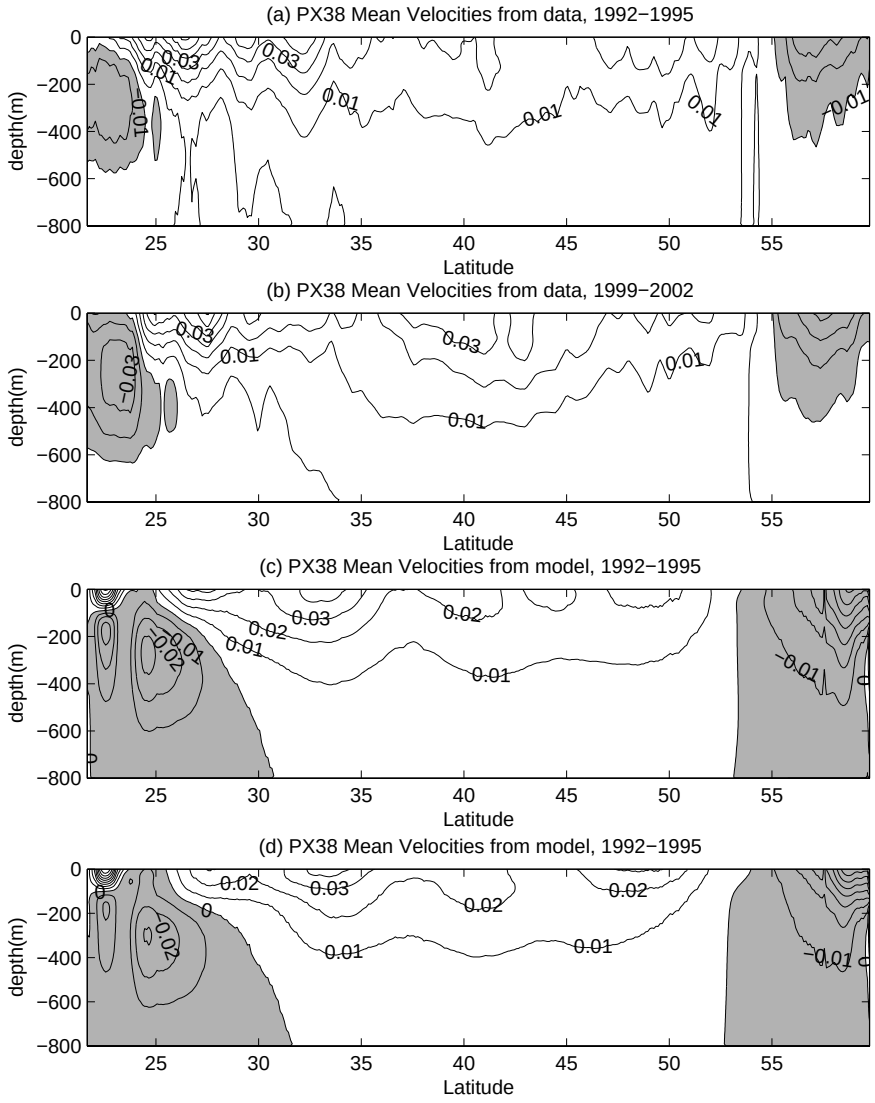

Figure 2.11: Comparison of four-year average velocity structure, before (1992-1995) and after (1999-2002) the change in NPC. (a) and (b) are XBT data velocities, before and after the change, respectively. (c) and (d) are model velocities, before and after the change, respectively. Shaded areas are westward velocities and light areas are eastward velocities. In all panels, the contouring interval is 0.01 m/s.

lated by the data-constrained model, was the increase in the transport of the NPC, and the associated intensification of the subtropical gyre. This signal is observed as a rise in NPC and subtropical gyre transport magnitudes through the first half of the time series, as illustrated in Figure 2.8. Streamfunctions in Figure 2.9 demonstrate the structure of the increase in the strength of the subtropical gyre. This evolution is associated with changes in the curl of the wind stress. The difference in four-year time-mean maps of Sverdrup transport, as calculated from the curl of the wind stress, has the same structure as the difference in the streamfunction for the same time periods (Figures 2.9(c) and 2.9(d)). The vertical structure of this change is illustrated by the sections of mean velocity along PX38 prior to and after the change (Figure 2.11). After smoothing the data over 4 degrees, differences between model and data are still evident. Model output is smoother, and the small-scale structure in the data represents both unresolved structure and noise from temporal aliasing of the *in situ* measurements. However, both data and model still show intensification of the jet structure at the southern end of the line and an increase in the large-scale incoming transport between about 40° N and 50° N. This signal is an example of the "NPC-dependent variability" illustrated in Figure 2.2(b).

On a shorter time scale, covariability between the gyres indicative of changes in the bifurcation of the incoming current is evident. This is the pattern suggested by Chelton and Davis (1982) as depicted in Figure 2.2(a). To observe this, we compare the outflows of the two gyres. Net transport across PX37 is the part of the subtropical gyre water that does not recirculate north of Hawaii, and hence is the part closest to the California coast described by Chelton and Davis (1982). The AKC plays the same role in the subpolar gyre. Model and data estimates of these transports are shown in Figure 2.12. Anticorrelated variability on a 3-4 year time scale is evident. The largest increase in subpolar gyre strength occurs at the peak of the 1997-1998 El Niño event. Similarly, when the fraction of NPC transport in each gyre was considered (another indicator of bifurcation

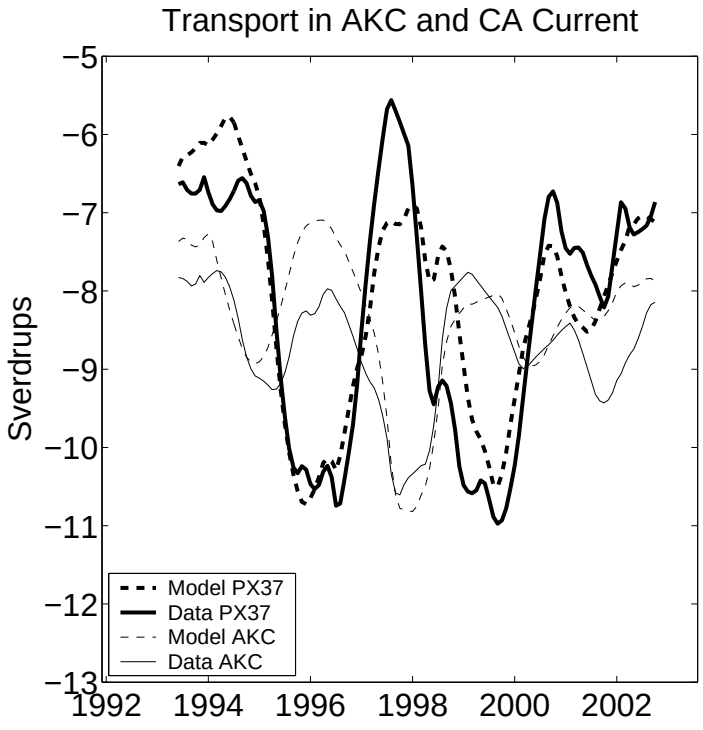

Figure 2.12: Anticorrelated variability of transport in the Alaska Current and the California Current (the net transport across PX37 is considered to be the California Current in this case). Both data and model estimates show clear anticorrelation, with AKC strengthening when the California current is weak, with time-scale of variability of approximately 3 years.

variability), a correlation with the SOI was noted. This is indicative of a possible teleconnection of the subpolar regions with the tropics.

The third mode of variability illustrated in Figure 2.2, the storage of upper layer volume in the box, is not evident in this region of the ocean. Model sea surface height, satellite altimetry, and steric height calculated from the model's temperature and salinity fields are all in good agreement. There is a significant change in steric height, which we find to be mainly a result of changes in salinity rather than temperature. The importance of salinity in the large scale changes in this region underscores the need for more *in situ* measurements to observe change and help constrain models.

Overall, the agreement between the model and the data was good with some notable exceptions. To some extent, this is to be expected, since the assimilation approach did incorporate the same data we compare against. However, as discussed by Köhl et al. (2007), the underlying ECCO solution to first order was not constrained by the XBT profile data set we use here, but by the climatological hydrography, the altimetry and other surface data. Taking this into account, our comparison can be seen as a quasi-independent check of the consistency of the ECCO solution with in situ data.

Along line PX37 and in the Alaska Current region, data and model estimates agreed very well both in their mean and time-varying components. However, problems in determining and resolving the boundary between the NPC and NHRC led to differences in mean and time-varying transports between the data and model. When the estimates are summed, the mean bias essentially disappears. The offsets shown in Figs. 2.5(a) and 2.5(b) therefore have to be considered somewhat artificial.

More problematic is the fact that data and model based transport estimates show different temporal variability, particularly in the NHRC. To first order, this indicates the need for more spatial resolution in the model simulations: the model has only a one-degree resolution and is therefore not able to properly sim-

ulate the currents around Hawaii or any other topographic feature. It is worth recalling, however, that XBT data have fairly high spatial sampling density but are available only once every quarter. This temporal sampling is not adequate and will inevitably lead to aliasing of the energetic eddy field. The respective errors in the *in situ* estimates have to be taken into account during our comparisons between monthly means of model output and quasi-synoptic shipboard measurements. The lack of proper *in situ* salinity observations is yet another source of errors in the data-based estimates.

Given all those uncertainties in the *in situ* and the model estimates, finding essentially the same time-mean and time-varying transport estimates from both sources is very encouraging and confirms that using a high-resolution data assimilation approach as part of an observing and synthesis system is a good strategy to obtain the best possible estimates of observable and unobservable quantities of the ocean circulation.

Chapter 2 appears with minor modifications as Douglass, E., D. Roemmich, and D. Stammer, Interannual variability in northeast Pacific circulation, *Journal of Geophysical Research*, **111**, C04001, doi:10.1029/2005JC003015, 2006. The dissertation author was the primary investigator and author of this paper.

3

Data-sensitivity of the ECCO state estimate in a regional setting

3.1 Introduction/Background

In order to understand the ocean's role in climate and climate variability, its time-varying physical state must be accurately known, including temperature and salinity structure, circulation and property transports, and air-sea exchanges of momentum, heat, and freshwater. Hydrographic measurements of subsurface structure are important, but even with global observational projects such as the World Ocean Circulation Experiment, efforts to determine time-mean transports by combining one-time transects from different seasons and years are complicated by inconsistencies due to the time-variability of the ocean (Ganachaud and Wunsch, 2003; Wunsch, 1978). More recent subsurface datasets such as the Argo array of profiling floats contain spatial and temporal information, but with limited resolution and depth range. Satellite observations, on the other hand, provide measurements with good spatial and temporal coverage of surface parameters such as sea surface height and temperature, but are not adequate to describe the subsur-

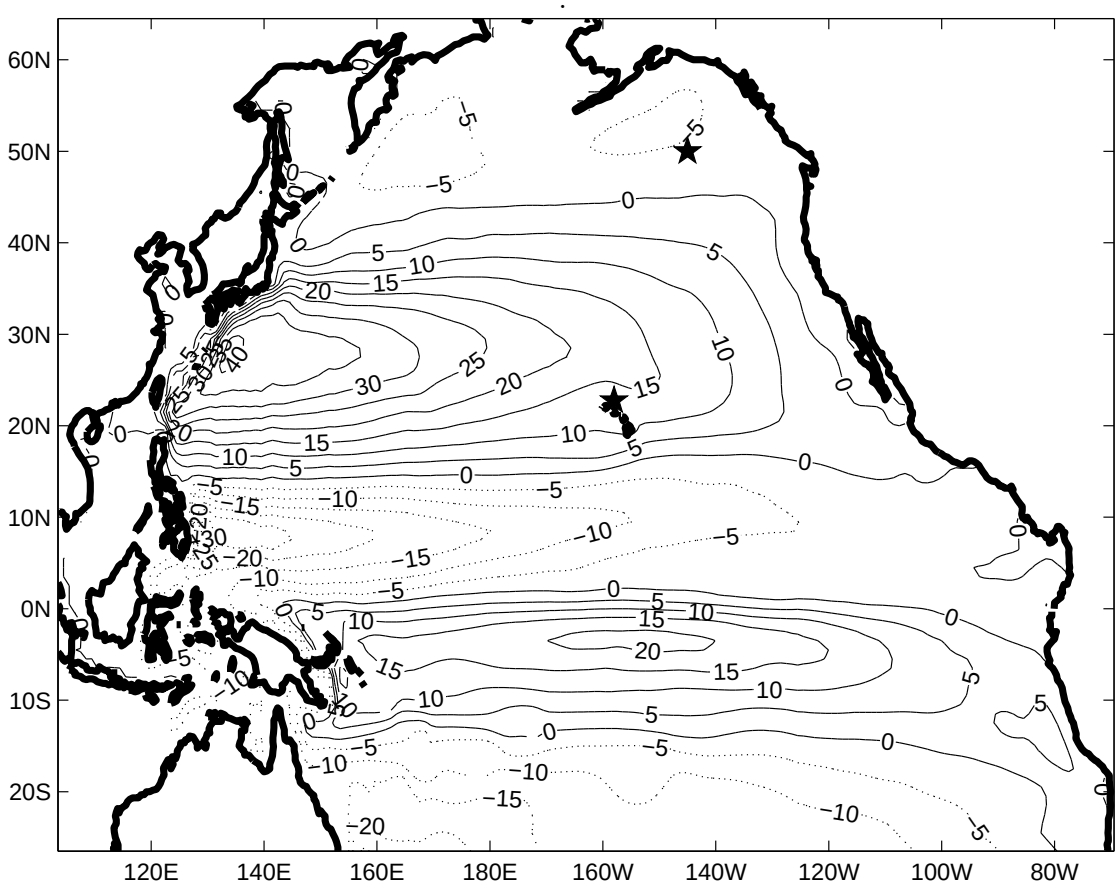

Figure 3.1: The region of study. The mean transport streamfunction in the top 800 m from the STANDARD experiment is shown. Stars indicate the positions of Station Aloha north of Hawaii and Ocean Station Papa in the Northeast Pacific.

face structure and its evolution in time. Existing estimates of air-sea exchanges are subject to substantial systematic errors in addition to their limited resolution. In the short-term, it is not practical to use data alone to fully characterize seasonal-to-decadal variability in the oceans.

Ocean state estimation is an approach to describing the ocean state that synthesizes the existing sparse ocean observations using the dynamics of numerical ocean circulation models. This process provides estimates of time-varying ocean circulation with temporal and spatial coverage unavailable from *in situ* or satellite data. However, ocean processes take place on spatial scales ranging from centimeters to hundreds of kilometers, and temporal scales from seconds to years. Spatial resolution of syntheses is limited at the present time by computing power, with the consequence that small-scale processes must be parameterized. Knowing the uncertainties of the estimates a model provides, and testing their sensitivity with respect to the data used as constraints and the prior errors of those data, are important precursors to using them for analysis.

The Estimation of Climate and Circulation of the Ocean (ECCO) Consortium (see Stammer et al. (2002a)) provides such dynamically consistent estimates of time-varying ocean circulation by constraining the MIT general ocean circulation model with most available ocean data sets. This model, which uses the adjoint approach to ocean state estimation, has been used to provide global syntheses of ocean data on a 1° grid for a period of up to 50 years (Stammer et al., 2002b, 2003, 2004; Wunsch and Heimbach, 2007; Köhl et al., 2007). These results have been used to study various oceanic problems as well as to initialize coupled ocean-atmosphere circulation models (Dommenget and Stammer, 2004; Pierce et al., 2004; Ponte et al., 2007).

In the present work, we analyze the sensitivity of the ECCO data-assimilating system in a regional setting to changes in the type and weighting of assimilated datasets. The adjoint assimilation procedure used by this model attempts to minimize a weighted model-data misfit. In this case, the model has 1° horizontal

resolution, so mesoscale processes are unresolved. The subsurface data, however, are sparse point-wise measurements which subsample these processes, introducing a mismatch between processes observed in the data and those present in the model, called a representation error. Ideally, full error covariances would be used to weight the data appropriately, accounting for both measurement error and representation error. Currently, such covariances are not known. Weights are estimated from available data. If the weights used for assimilation of these data are too high, resolution errors can lead to inaccurate solutions that alias eddy effects into the large-scale synthesis results. However, if the weights are too low, the influence of the subsurface data is marginalized, and the assimilation process will not take full advantage of this extensive data set. An analysis of the weighting scheme is needed to determine if the model is adequately adjusting to the subsurface information available to it. To this end, the model is run with assimilation of only surface data and with assimilation of only subsurface data, to determine the relative influence of each type of data on the model estimate. In addition, the model is run with higher weights on the subsurface data, to demonstrate the model's sensitivity to these weights, and the costs and benefits associated with changing them.

The structure of the paper is as follows. Section 2 describes model and the four experiments used in the analysis. Section 3 compares the results from each experiment with two of the assimilated data sets to demonstrate how accurately they are estimated by the model. Section 4 is a comparison with independent data, providing an assessment of the quality of each estimate. Section 5 compares the present Pacific regional estimates with an existing global ECCO estimate, in terms of both the model-data misfits and the adjustments to control parameters. Finally, section 6 has discussions and conclusions.

3.2 Model Description

The present analysis employs the ECCO model in a regional setting in the Pacific Ocean north of 26°S. The model and adjoint assimilation approach is explained in detail in Stammer et al. (2002b) and Köhl et al. (2007); in this work we present only a conceptual description. In this method, the model runs forward to simulate the time-varying ocean state. From this state, a cost function is calculated from a weighted model-data misfit. The adjoint model is subsequently used to provide the gradient of the cost function with respect to the model variables. A standard descent algorithm then uses these gradients to provide adjustments to the surface forcing and initial conditions to reduce the misfit while maintaining dynamical consistency. A new forward run is then performed using the adjusted forcing, and a new cost function is calculated. The process is repeated iteratively to minimize the cost function.

The model cost function provides a quantitative measure of the overall misfit of the model relative to observations. In addition, it is a useful tool in analyzing the model results. It is calculated as follows:

$$J = \sum (model - data)^2 * W_{data} + \sum (control\ adjustments)^2 * W_{control} \qquad (3.1)$$

The first term is composed of the misfit between the simulated ocean state and data used as constraints, while the second term quantifies the changes to the control variables, which in this case consist of the model's initial conditions and the surface forcing of heat flux, freshwater flux and wind stress. Each type of data and each control variables have a corresponding weight matrix determined from the inverse of the prior error. Minimizing the cost function is equivalent to finding the best dynamically consistent fit between the model and the data.

For the present work, the region of study is the Pacific Ocean north of 26°S, as shown in Figure 3.1. The model has horizontal resolution of 1° in latitude and longitude, and 50 vertical levels. The level thicknesses increase from 5 m at the surface to 500 m at depth. All the model runs span the time period

1992-2004, and the output consists of daily SSH fields and monthly means of temperature, salinity, and zonal, meridional, and vertical velocity. The output also includes an adjustment to the initial conditions and adjustment fields every two days for the surface forcing. Initial temperature and salinity are from the Levitus 1994 climatology (Levitus and Boyer, 1994; Levitus et al., 1994), and the NCEP reanalyses of heat flux, freshwater flux, and zonal and meridional wind stress are used for initial surface forcing (Kalnay et al., 1996).

The model domain is bounded by land to the north and to the east, but the southern boundary is open to the South Pacific, and the western boundary is open to the Indonesian Throughflow. Temperature, salinity, and zonal and meridional velocity are prescribed on the boundaries. These values were obtained from a global product produced by the ECCO Consortium spanning the time period 1992-2004 (hereafter ECCO-GODAE; see Wunsch and Heimbach (2007)). While the horizontal resolution of the ECCO-GODAE model is the same as in our experiment, a significant difference is the increase in vertical resolution from 23 levels to 50. Linear interpolation was used to obtain 50-level boundary conditions from the global 23-level solution. Another difference is that the weights used by the ECCO-GODAE model differ from the weights used in any of the experiments described below. We chose the ECCO-GODAE model for boundary conditions because it spanned the full time period from 1992-2004, and no model synthesis for the full time period using any of the weighting schemes described below was available.

Four experiments, described below, were performed with the model. The physics of the model do not change between the experiments; all differences are a result of the datasets used as constraints and the error information associated with those data.

The first model experiment consists of a standard run (referred to hereafter as STANDARD). The estimate in this case is constrained by all available data, including satellite measurements such as sea surface height (SSH) from al-

timetry and surface winds from scatterometry, other surface measurements such as Reynolds sea surface temperature (SST) and sea surface salinity (SSS), and *in situ* measurements from expendable bathythermographs (XBTs), conductivity-temperature-depth sensors (CTDs), drifters, and Argo profiling floats. Observational data are bin-averaged onto the model grid, a process which removes some of the eddy noise from the data. Additionally, the model climatology is constrained to Levitus climatology. Finally, the drift of temperature, salinity, and vertical velocity between the first and final years of the state estimate is constrained. The STANDARD model uses the same weights as a global run previously performed at Scripps Institution of Oceanography (Köhl et al., 2007). Since the implementation of full error covariances is not computationally feasible at this time, the weighting matrices are diagonal, with the inverse of the prior variances on the diagonal. See Köhl et al. (2007) for further details on the choice of data and prior diagonal error fields.

The second experiment (called NOINSITU) does not assimilate any subsurface data. All measurements from XBTs, CTDs and Argo profiling floats are excluded from the computation of the control adjustment fields. The satellite measurements of SSH and winds are still assimilated, as are SST and SSS. The misfit between the subsurface measurements and the model output fields is still calculated as a diagnostic to aid in comparison between the different model experiments, but this misfit is not considered when the adjustments to forcing fields are determined, and therefore these data have no influence on the resulting state estimate.

The third experiment (called NOSAT) assimilates the subsurface data, but excludes surface data. This category includes satellite altimetry, wind scatterometry, and SST and SSS fields. As in the NOINSITU run, misfits are still calculated, but now the adjustments to the forcing are solely determined by the subsurface data. The resulting state estimate provides perspective on the importance of subsurface data in determining the adjustments the model makes.

The first three experiments use the same weighting matrices, and vary by the inclusion or exclusion of particular types of data constraints. The fourth experiment (WEIGHTED), is constrained by all available data, but changes the weights relative to the STANDARD case. In our assimilation, the number of subsurface observations is low, relative to the number of surface observations. Additionally, the error bars prescribed to the subsurface data, in order to account for both measurement error and mesoscale representation error, are relatively large, with standard deviations ranging from more than 0.5°C and 0.14 psu at the surface to 0.05°C and 0.01 psu at depth. As a result, the relative weights on the subsurface data are small, and their effect on the resulting state estimate is minor. Larger weights on the subsurface data will increase their relative influence on the solution. To achieve this increased influence, in the WEIGHTED run, the weights on the subsurface data are increased by a factor of 16 relative to the standard case, which is equivalent to decreasing the prior error by a factor of four (see Equation 3.2-3.4). The surface data are assimilated with the same weights used in the other experiments. This increases the relative impact of the subsurface data on the solution.

$$\sigma_{weighted} = \frac{\sigma_{standard}}{4} \tag{3.2}$$

$$W = \frac{1}{\sigma^2} \tag{3.3}$$

$$W_{weighted} = 16 * W_{standard} \tag{3.4}$$

As an initial demonstration of the trade-off in cost between decreasing model-data misfit and increasing adjustments to the forcing, as well as an indicator of some of the differences between the model results, the evolution of several components of the cost function is shown in Figure 3.2. Panel (a) shows the percentage cost decrease, or the total cost normalized by the initial cost, for the first 30 iterations of each experiment. The WEIGHTED estimate (triangles) has the greatest percentage decrease in total cost. Panels (b), (c), and (d) show the cost contributions of XBT misfits, SSH misfits, and heat flux adjustments respectively,

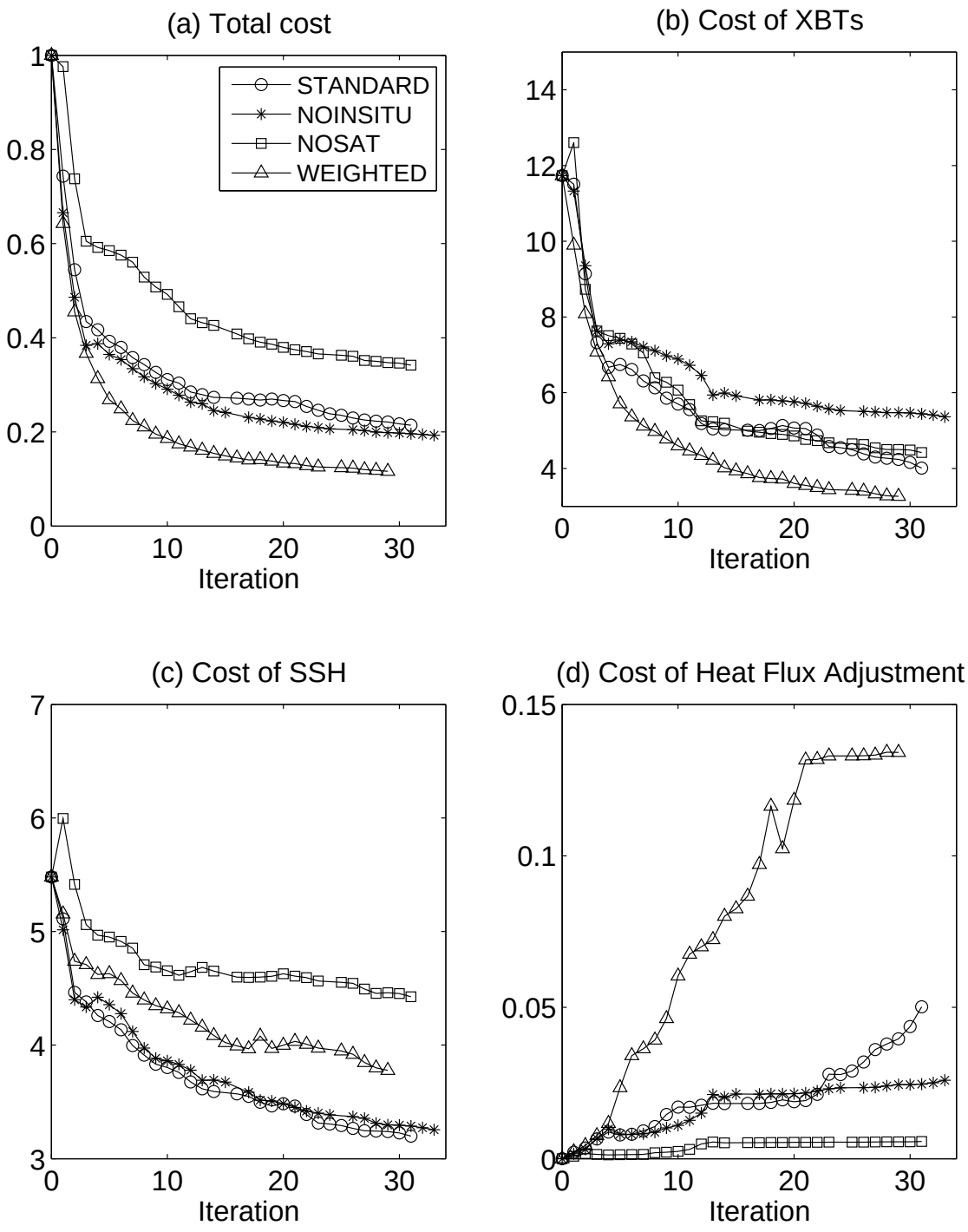

Figure 3.2: (a) Total cost of each of the four experiments as a function of iteration, normalized by initial value. (b) Normalized cost of the model-XBT misfit for each experiment. (c) Same as (b), for sea surface height anomaly misfit. (d) Normalized cost of adjustments to the heat flux. See text for details.

normalized by their prior variances. Since cost is proportionate to the square of the misfit, as the model converges to a solution, the misfits approach the data variance, and the normalized cost converges to unity. In order to compare the four experiments directly, the misfits from all experiments are normalized by the prior variances from the STANDARD experiment. Thus, the differences in Figure 3.2 are due only to model-data misfit. Cost contributions from XBTs and SSH decrease with each iteration in all experiments. The XBT cost has decreased the most in the WEIGHTED experiment, which has the highest penalty associated with this misfit, and the least in the NOINSITU experiment, which does not assimilate these data. The NOSAT and STANDARD costs are nearly identical, indicating that the assimilation of surface data has little effect on the estimation of subsurface data. One might expect the NOSAT experiment to match the XBT data more closely than it does, since there are no competing costs from surface data to constrain it. However, relative to the XBT cost component, the cost of the adjustments to the forcing is too high to justify the changes necessary for a reduced misfit. In the WEIGHTED experiment, weights on the XBTs are so high that the relative cost of adjusting the forcing is small, so large adjustments are made and a smaller model-data misfit is attained. In the NOSAT experiment, similar changes would increase the cost of the forcing more than they would reduce the cost of the model-data misfit; thus, the estimate does not make those adjustments, and the misfit between XBTs and the model is comparatively higher.

A similar effect is noted in the SSH cost component (Figure 3.2(c)). The largest model-data misfit in SSH, not unexpectedly, occurs in the NOSAT estimate, which does not assimilate those data. The cost of SSH misfit in the NOINSITU experiment is almost identical to the STANDARD cost, indicating that the estimation of surface data is not affected by the additional assimilation of subsurface data in the STANDARD experiment. This also suggests that even in the NOINSITU experiment, which is not restricted by the constraints of the subsurface data, the cost of adjusting the forcing to match the SSH data more accurately is higher

than the reduction in cost that would result from such changes. Since there is no experiment with higher weights on the SSH data, it is harder to be sure in this case than it was in the case of the XBTs. In this component, the misfit between the WEIGHTED model estimate and the measured SSH is slightly larger than that in the STANDARD run, indicating that the improved match to the XBT data comes at the expense of the a reduced match to the SSH data. This may be due in part to a warm bias in the XBT data (Gouretski and Koltermann, 2007), introducing a level of inconsistency between the XBT and SSH data. This is considered further in the discussion section.

The costs of the adjustments made to the heat flux are shown in Figure 3.2(d). These are largest in the WEIGHTED experiment, indicating that larger adjustments are necessary for increased accuracy in the fit to the data. While these adjustments are significant relative to the adjustments of the other three model estimates, the normalized costs are still below 0.2, indicating that the magnitude of the changes is, on average, less than 20% of the prior variance. Therefore, on average, these adjustments are well within the expected limits. It is important to note that the total cost and the model-data misfits are still decreasing, indicating that the solutions have not fully converged. However, enough iterations are complete to demonstrate robust differences resulting from the various weighting and assimilation schemes.

3.3 Comparison with Assimilated Data

Comparisons between the model output and the data to which it is constrained are informative in several ways. First of all, differences between the data sets and the model results indicate the extent to which the model is accurately representing the data. Second, because the experiments assimilate different subsets of the data, the differences between the versions demonstrate the extent to which each type of data affects the model output. Therefore we compare the model estimates

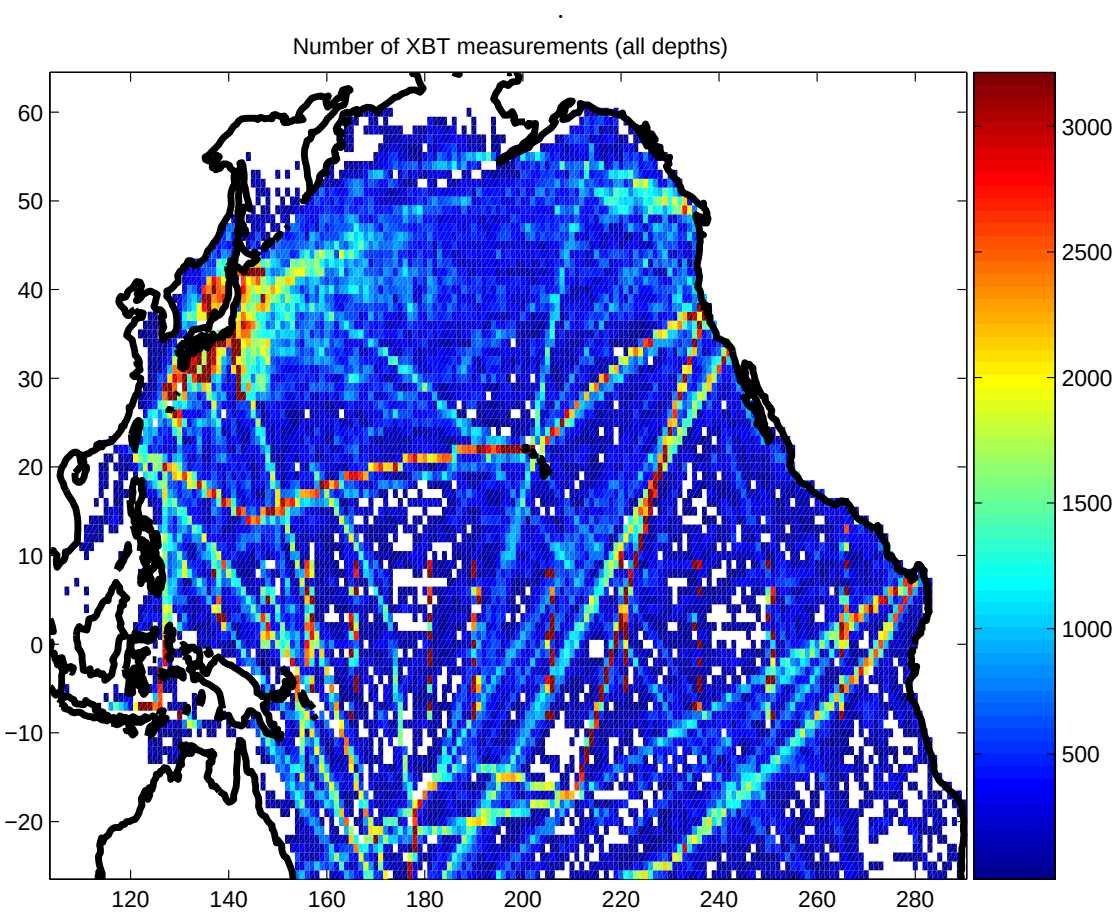

Figure 3.3: Coverage of XBT data displayed as the depth-integrated number of measurements available at each location from 1992-2004.

to the XBT temperature profiles, which comprise the largest subsurface dataset, and to the satellite altimetric height dataset, the most complete surface dataset, to determine the realism of our various simulations and the relative importance of surface and subsurface data.

3.3.1 Heat Content/SST

The XBT temperature data is the subsurface dataset with the best coverage both temporally and spatially. Even so, its coverage is inhomogeneous, as seen in Figure 3.3, which shows the depth- and time- integrated number of measurements for each location. When comparing model and data estimates, the sparse nature of this data must be accounted for. At each time step, the heat con-

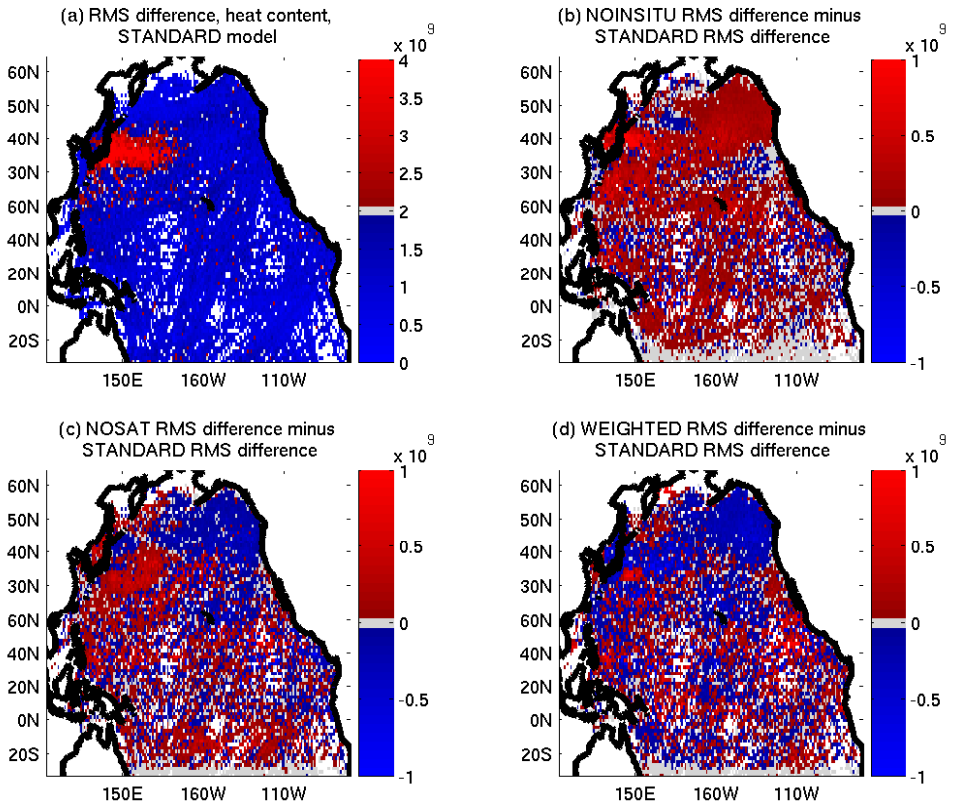

Figure 3.4: (a) RMSD between heat content estimated by the STANDARD experiment and heat content estimated from XBT data. (b) Difference between RMSD between NOINSITU estimated heat content and XBT-derived heat content, and STANDARD RMSD as shown in panel (a). (c) Same as (b), for NOSAT estimate. (d) Same as (b), for WEIGHTED estimate. In difference maps, red indicates positive differences (higher RMSD than STANDARD) and blue indicates negative differences (lower RMSD than standard). Units are Joules.

tent was computed from the model output at the positions where XBT data are available, and maps of estimated heat content were constructed. The root-mean-square difference (RMSD) between data- and model-estimated heat content (mean removed) are mapped in Figure 3.4. Figure 3.4(a) shows the mapped RMSD between the STANDARD model estimate and the data, and panels (b), (c), and (d) are differences between the STANDARD RMSD and the RMSDs from other model estimates. Positive numbers (red) indicate higher RMSD than STANDARD, while negative (blue) areas indicate a lower RMSD than STANDARD and thus a more accurate estimate. Several features are immediately evident. In panel (a), we see a region of high RMSD in the region off the coast of Japan, where the Kuroshio separates from the coast and meanders east to the Kuroshio extension region. This is a highly variable region with intense mesoscale activity, which is not present in the model but which aliases XBT measurements. Panels (b) and (c) indicate that both NOINSITU and NOSAT have higher RMSDs (less accurate estimates) than the STANDARD experiment in this region. In panel (d), the WEIGHTED estimate has negative values in this region, indicating that it simulates the data-based heat content more accurately than the STANDARD experiment. Overall, the NOINSITU RMSDs are slightly worse than any of the other model estimates. This is expected, since NOINSITU is not constrained by these data. The NOSAT estimate matches the XBT estimate more closely than the STANDARD estimate does in some areas such as the Gulf of Alaska, but has higher RMSDs in the Kuroshio region and south of the equator. The WEIGHTED estimate is the most accurate, indicating that the change in weights is making a significant difference in the assimilated product.

A time series of heat content anomaly in the upper 750 m of the ocean, calculated from optimally interpolated XBT data (Willis et al., 2004, hereafter WRC), is also available for comparison with the model estimate. There are several issues to be considered with this comparison. First, as mentioned previously, Gouretski and Koltermann (2007) have found a time-varying but systematically

warm bias in XBT measurements, which introduces a highly correlated error into both the WRC product, and into the data being assimilated by the model. This kind of error is not accounted for in the covariances used to assimilate these data, and could have serious impacts on model estimates of temperature, especially since it is inconsistent with other data being assimilated. In addition, or possibly as a result, a large secular increase in heat content is found in the ECCO estimates. While heat content is thought to increase over this time period (Levitus et al., 2005), the temperature drift in the model estimates implies a heat uptake that is larger than expected. In their estimate, Köhl et al. (2007) found an increase in heat content corresponding to a global net ocean heat uptake in their model estimate of 1.1 W/m^2. When the domain is restricted to the Pacific Ocean north of 26°S, as in our setting, the average heat uptake is 1.5 W/m^2. The average heat uptake for each of the four estimates and for the data are found in Table 3.1. Of the four model experiments, the smallest uptake, of only 0.78 W/m^2, is found in the NOSAT estimate. The largest uptake is found in the NOINSITU estimate, which averages 3.30 W/m^2. The STANDARD estimate shows an average heat uptake of 2.83 W/m^2, while the WEIGHTED estimate averages 2.62 W/m^2 over the time period. The data from WRC indicate an average heat uptake of only 0.41±0.12 W/m^2.

The secular heat increase in the model estimates makes direct comparisons with heat content estimated from XBT data more difficult. To determine if variability in the model is correlated with that in the data, the trend is removed from the model- and data-derived heat content estimates. Figure 3.5 shows detrended heat content from the data and from the four experiments. The monthly model estimates and quarterly WRC estimates are smoothed over one year to remove higher frequency variability. Correlation coefficients for these detrended and smoothed time series are listed in Table 3.1. The WEIGHTED experiment estimates heat content variability most accurately, with a correlation coefficient of 0.54. Figure 3.5 shows that the STANDARD estimate is nearly identical to the

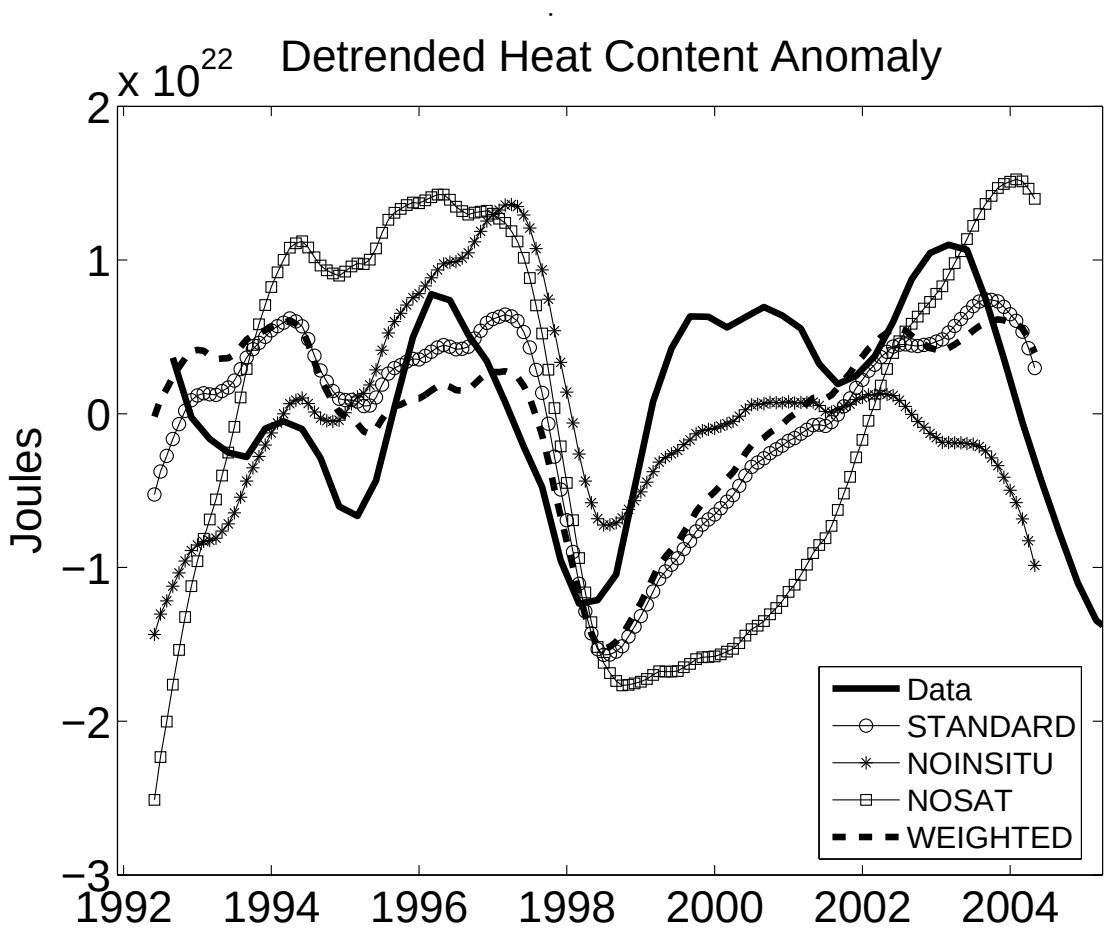

Figure 3.5: Time series of heat content anomaly as a function of time, from an optimally interpolated XBT dataset, and from each of the four estimates. All timeseries were detrended to remove a secular heat content trend from the model output.

Table 3.1: Basin-averaged heat uptake and correlation coefficients for comparison between model- and XBT-estimated heat content.

	Net Heat Uptake	Correlation Coefficient
Data (WRC)	0.41	N/A
STANDARD	2.84	0.49
NOSAT	0.78	0.19
NOINSITU	3.30	0.26
WEIGHTED	2.62	0.54

WEIGHTED estimate, and its correlation coefficient it only slightly lower at 0.49. The NOINSITU and NOSAT estimates have significantly lower correlations, at 0.29 and 0.19 respectively, indicating the importance of both surface and subsurface information when estimating an integrated quantity such as heat content.

Another test of realism of the temperature estimate comes from empirical orthogonal functions, or EOFs, of SST. EOFs represent the decomposition of a time series into orthogonal modes representing the most energetic patterns of variability (Lorenz, 1956). Each EOF has two parts: the spatial pattern of variability, and the associated amplitude time series. Prior to the decomposition, the mean was removed and a 12-month smoothing was applied to remove the seasonal cycle and other high-frequency variability. Mantua et al. (1997) defined the Pacific Decadal Oscillation (PDO) index as the time-series associated with the first EOF of SST in the North Pacific. The spatial pattern of variability associated with this index is seen in Figure 3.6(e), the EOF for the Reynolds SST data: a horseshoe shape centered in the North Pacific, with high values in the center and to the west and lower values in the coastal areas to the north and east as well as at the equator. This mode represents 37% of the variance of the SST data. The other panels of FIgure 3.6 show differences between the first EOFs of the model estimates and that of the data. The WEIGHTED result has lower values than the data in the northern half of the Pacific, and higher values in the south, but the differences are generally small in amplitude. The first EOF represents 36% of the variance of the WEIGHTED estimate. The NOINSITU result has deeper

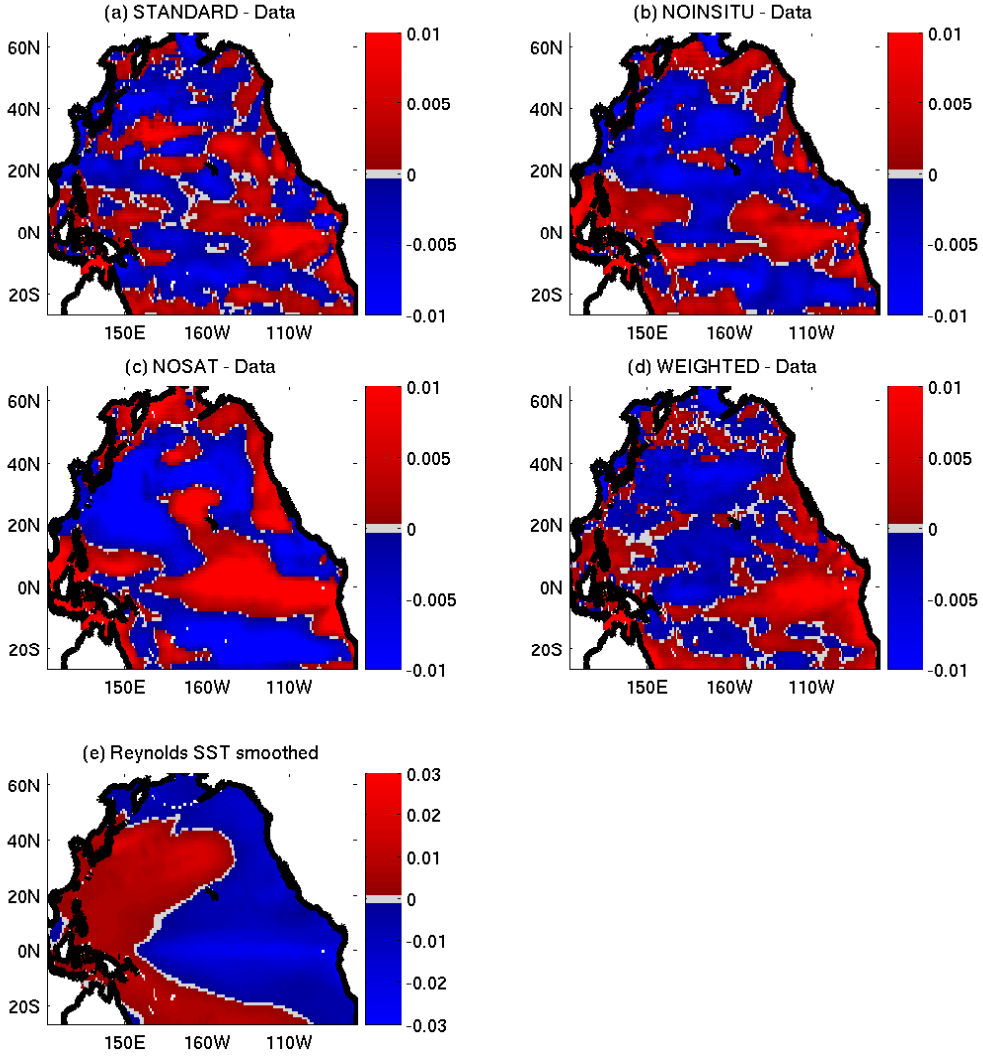

Figure 3.6: (a)-(d) Maps of the differences between the first EOF of SST from the four experiments and the first EOF of SST from Reynolds SST data (e) Map of the first EOF of the Reynolds SST data.

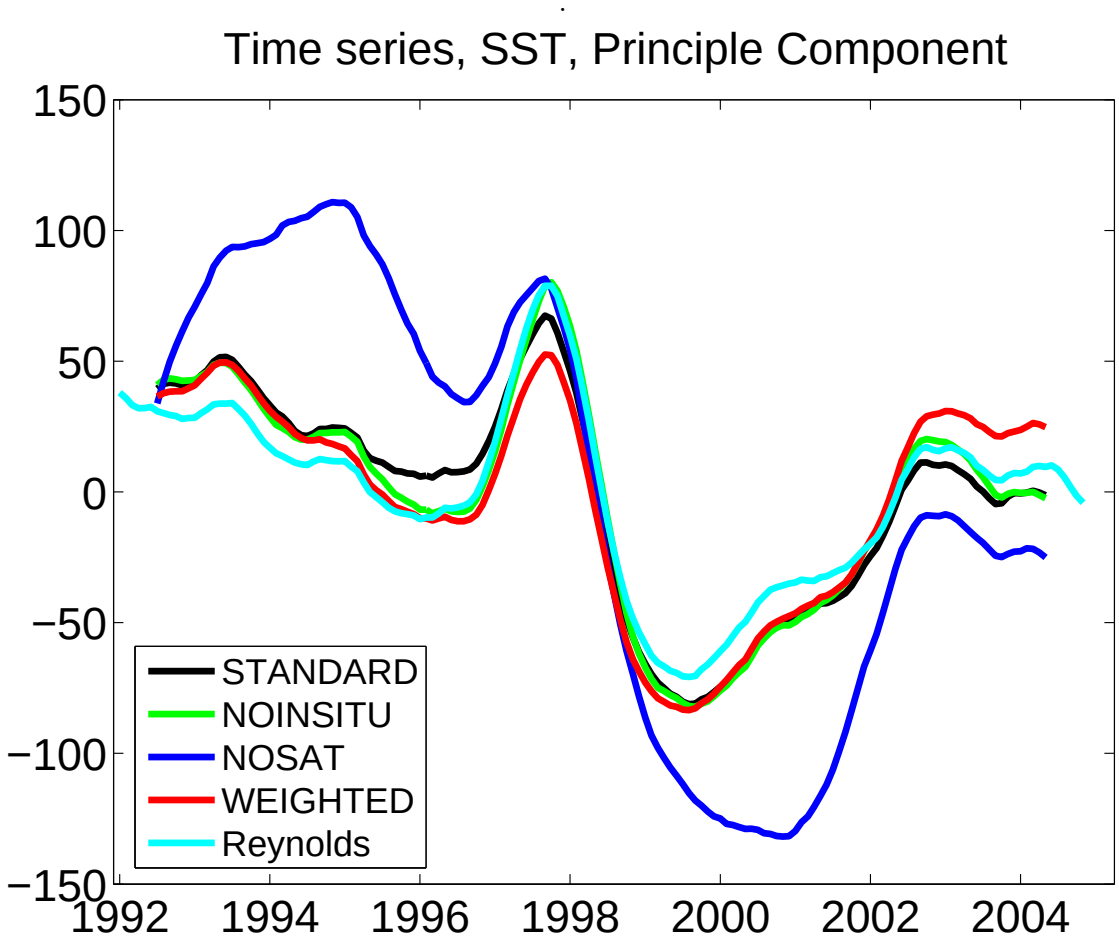

Figure 3.7: Amplitude time-series associated with the first EOF of SST for each of the four experiments and also for the Reynolds SST data.

lows at the equator and in the northern and eastern coastal regions, in a pattern similar to the PDO, indicating that the physical processes associated with this variability are stronger in the NOINSITU estimate. This mode represents 32% of the variance of NOINSITU. The STANDARD EOF indicates a deeper low at the equator but a lower peak in the central North Pacific, with differences of larger amplitude than either WEIGHTED or NOINSITU. The first EOF of STANDARD represents only 31% of the variance. The first EOF of the NOSAT estimate has differences of the largest amplitude, which could indicate that in this experiment, the most energetic mode, representing 39% of the variance, is associated with different physical processes than in the other experiments. The amplitude time-series associated with the first EOFs, shown in Figure 3.7 for the data and for each model experiment, reinforce the conclusion that the NOSAT estimate is distinct from the others. All model time-series have a correlation with the data of greater than 0.9 except NOSAT, which has a correlation below 0.75.

3.3.2 Sea Surface Height

SSH has been measured continuously by satellites since 1992. The model assimilates daily fields of along-track SSH anomaly from the TOPEX/Poseidon and Jason satellites. Using a method similar to that used for heat content to account for inhomogeneously distributed data, maps of the RMSD between measured and modeled SSH anomalies are created (Figure 3.8). Panel (a) shows the RMSD between STANDARD SSH anomaly and altimetric height data, and panels (b), (c), and (d) show the difference between the NOINSITU, NOSAT, and WEIGHTED RMSD and the STANDARD RMSD, respectively. As with heat content, the main signal is evident in the Kuroshio Extension region, an area with intense mesoscale activity. The differences between NOINSITU and STANDARD (Figure 3.8(b)) are approximately evenly split between positive and negative, and all differences are small in magnitude. This indicates that the skill of the two experiments in estimating SSH is about equal, implying that the effect of assimilation of subsurface

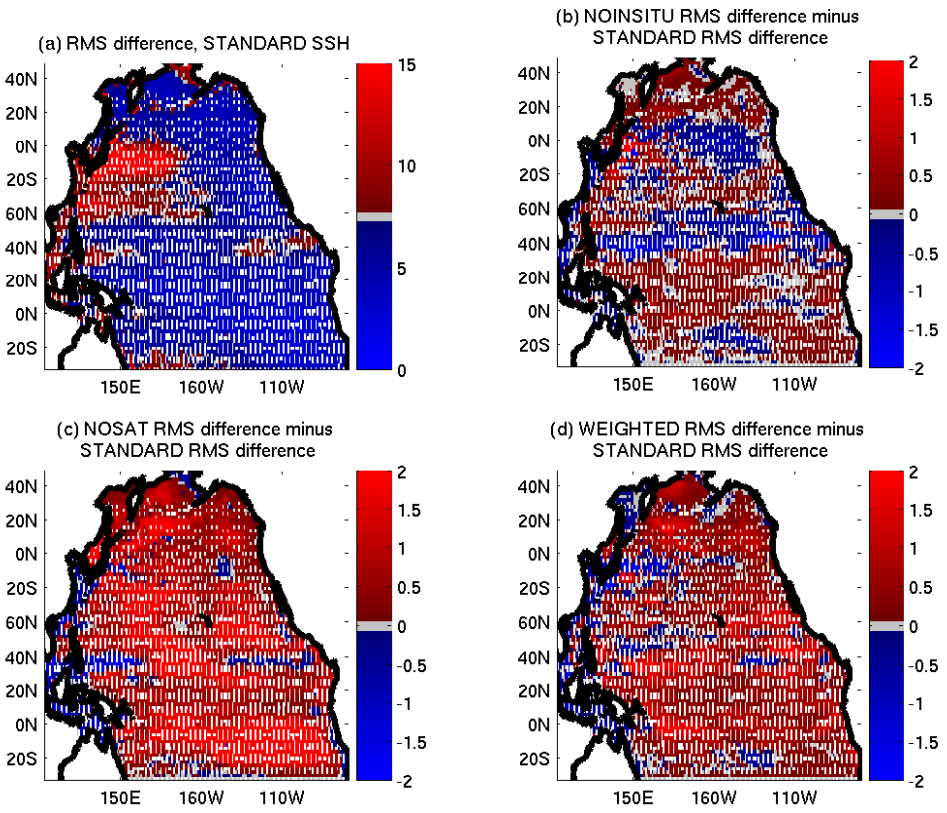

Figure 3.8: As Figure 3.4, but for SSH instead of heat content. Units are cm.

data on estimation of SSH with the weights used in the STANDARD model is minimal. The WEIGHTED RMSD is higher than the STANDARD RMSD in most regions, as indicated by Figure 3.8(d). This implies that adhering more closely to subsurface data in these areas is detrimental to the objective of minimizing SSH misfit. However, these differences are still smaller than those indicated on the map of differences between NOSAT and STANDARD RMSD (Figure 3.8(c)). It is clear that the NOSAT experiment, which does not assimilate any surface data, is the least accurate estimate of SSH anomaly.

As with SST, EOF analysis is used to compare observed SSH signals to their representation in the experiments. Monthly estimates of sea surface height anomaly were smoothed over 12 months to remove the annual cycle as well as other high frequency variability. The first EOFs for the data and each model estimate are shown in Figure 3.9. The EOF of the data shows a large feature in the tropics, with a high region at the equator east of about 160°W, extending about 5 degrees north and south of the equator, and a low area to the west, with less zonal extent but greater meridional extent. There is also a signal in the North Pacific similar to the PDO pattern seen in the SST EOF, with low values in the central North Pacific extending to the western edge, and high values in the northern and eastern coastal regions. The signal in the North Pacific has smaller magnitudes than that in the tropics, indicating that the tropical signal is dominant in amplitude. The STANDARD and NOINSITU estimates (panels (a) and (b) respectively) show both the tropical and subtropical signals with approximately the right magnitudes. The STANDARD has a high region north of the equator that does not appear in the data. The NOSAT estimate (panel (c)) is the least similar to the data. The equatorial peak is much lower, and values throughout the North Pacific are considerably higher. The WEIGHTED estimate (panel (d)) replicates the main features of the data, but with slight differences such as a weaker high at the equator in the east, a weaker low in the central North Pacific, and higher values in the northern and eastern coastal regions than in the data. In this

estimate, the tropical signal and North Pacific signal seem to have approximately equal amplitude. In general, the NOINSITU model, for which altimetric height data comprises the majority of the assimilated data, replicates the dominant mode of variability of these data more accurately than any of the other experiments.

In the amplitude time-series associated with these EOFs (Figure 3.10), the most significant feature, replicated in all estimates, is a peak just before the end of 1997, associated with a strong El Niño event that occurred in 1997-98. This, together with the spatial pattern indicating the high level of energy in the tropics, confirms that the most energetic mode of interannual variability in SSH is associated with the El Niño oscillation. All time series in Figure 3.10 are highly correlated, with correlation coefficients greater than 0.9. These time series are also well correlated with the amplitude time-series of the first EOF of SST (Figure 3.7), indicating that the most energetic modes of SST and SSH are controlled by the same dynamics.

3.4 Comparison with Independent Data

So far, we have investigated the skill of the individual experiments in simulating the data to which they were constrained. In the following, independent data from two time series not used as constraints are used to assess the skill of the estimates.

3.4.1 Station Aloha

The Hawaii Ocean Time-series (HOT) is a time series of hydrographic measurements at Ocean Station Aloha, which is just north of Oahu, Hawaii at 22°45' N, 158°00" W (Karl and Lukas, 1996). Temperature and salinity have been measured at this location approximately once per month since October of 1988. This dataset was not assimilated in any of the four experiments. As a result, it is independent and can be used as a test of the model's realism.

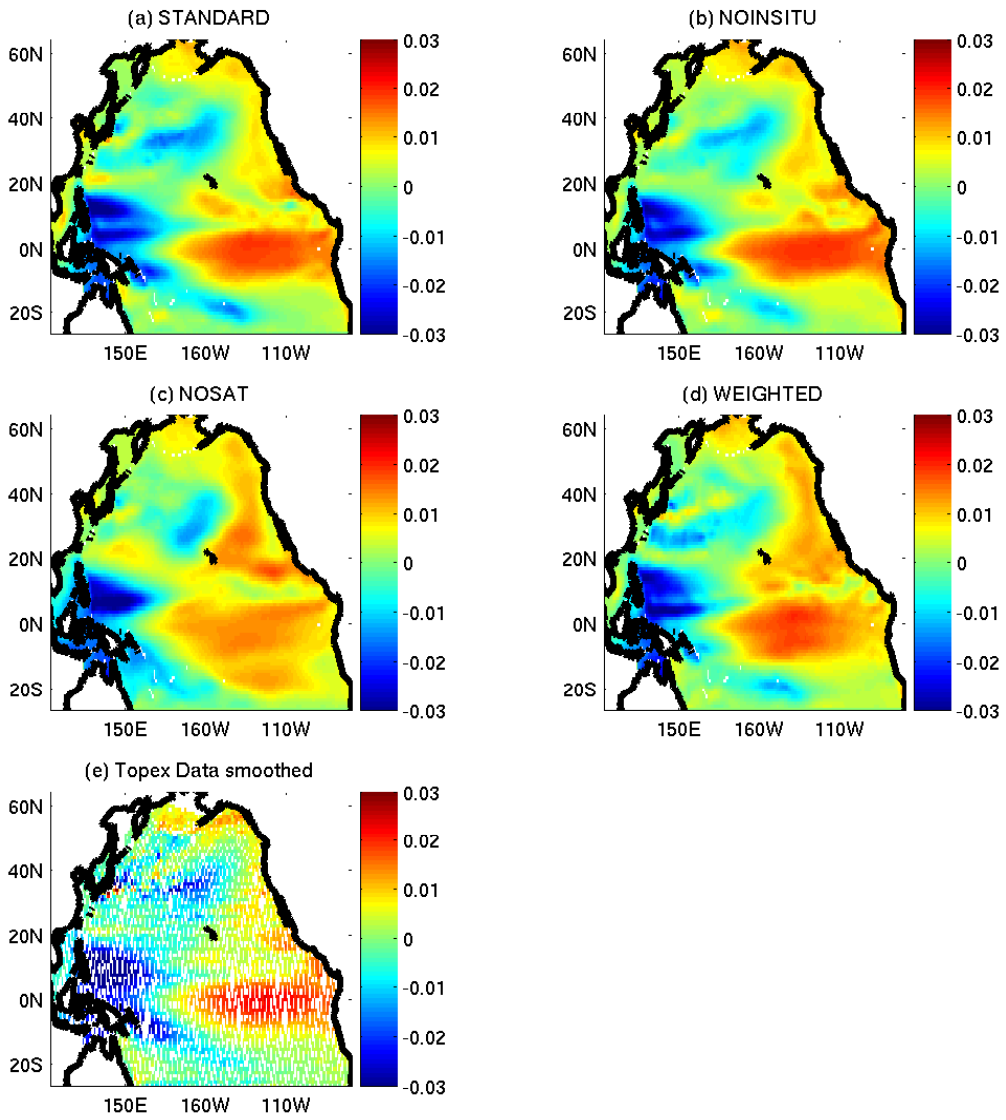

Figure 3.9: (a)-(e) Spatial maps of the first EOF of SSH, for the four experiments and for the altimetric height data.

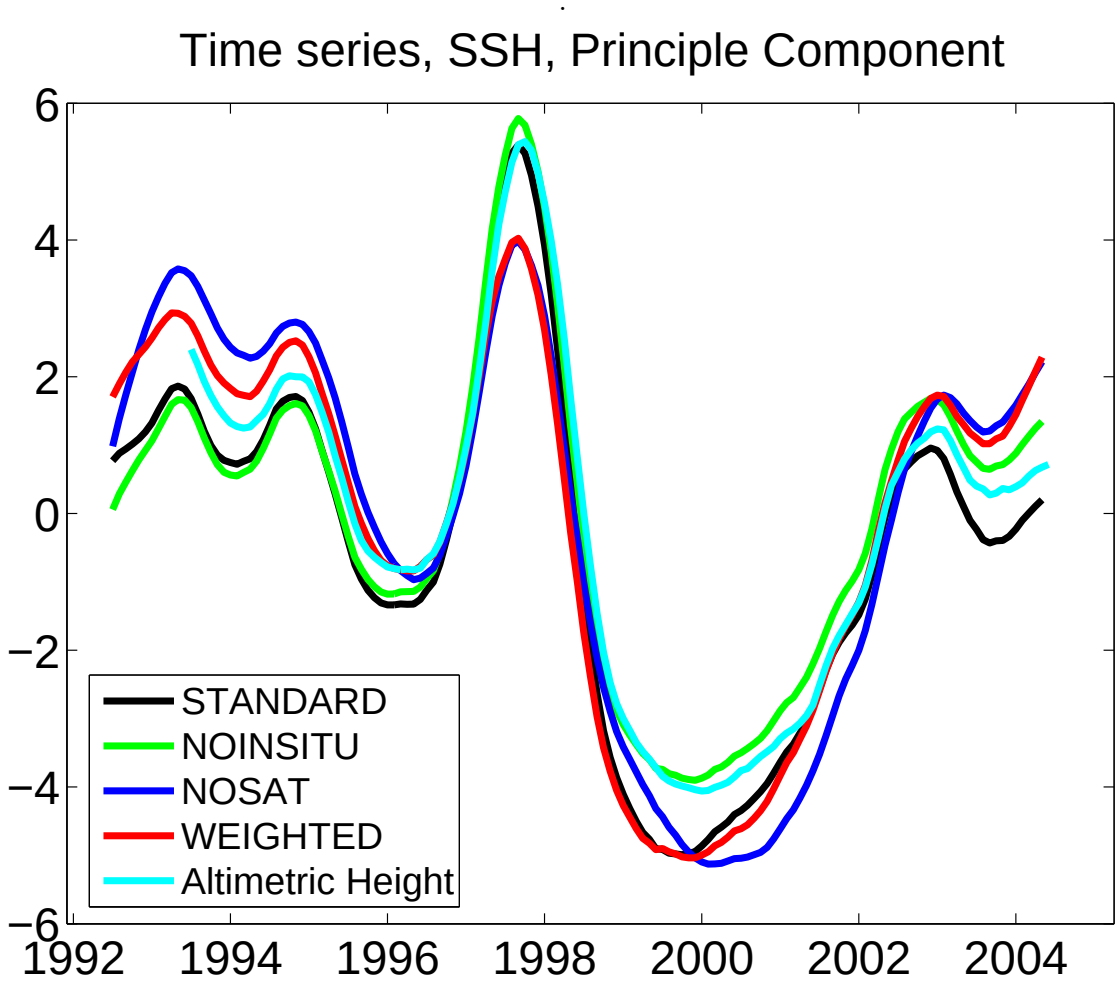

Figure 3.10: Amplitude time-series associated with the first EOF of SSH for each of the four experiments and also for the Topex SSH data.

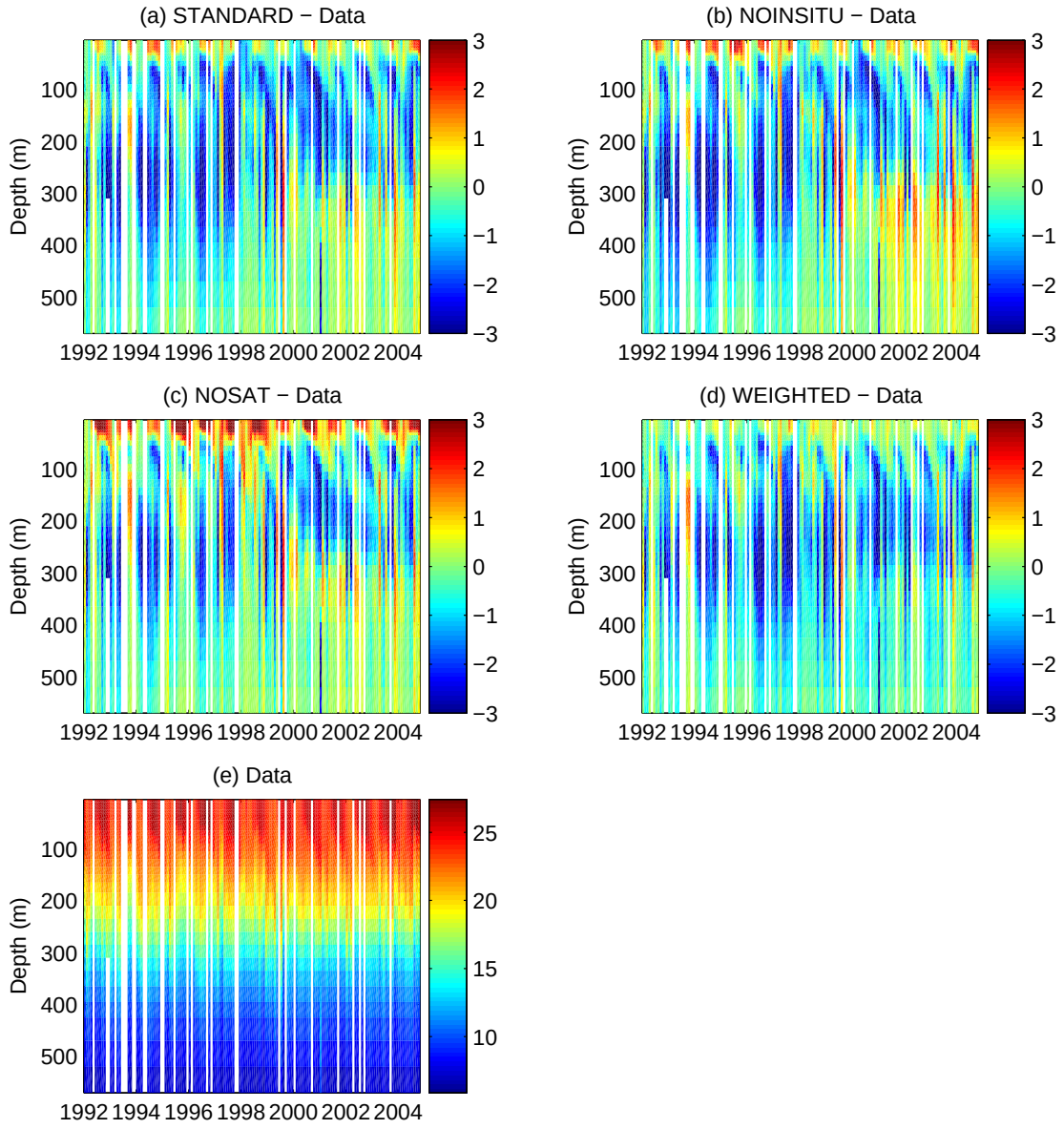

Figure 3.11: (a)-(d) Temperature difference in the top 500 m between model estimate and data at Station Aloha, for each of the four estimates. (e) The temperature time series at Station Aloha. All units are °C.

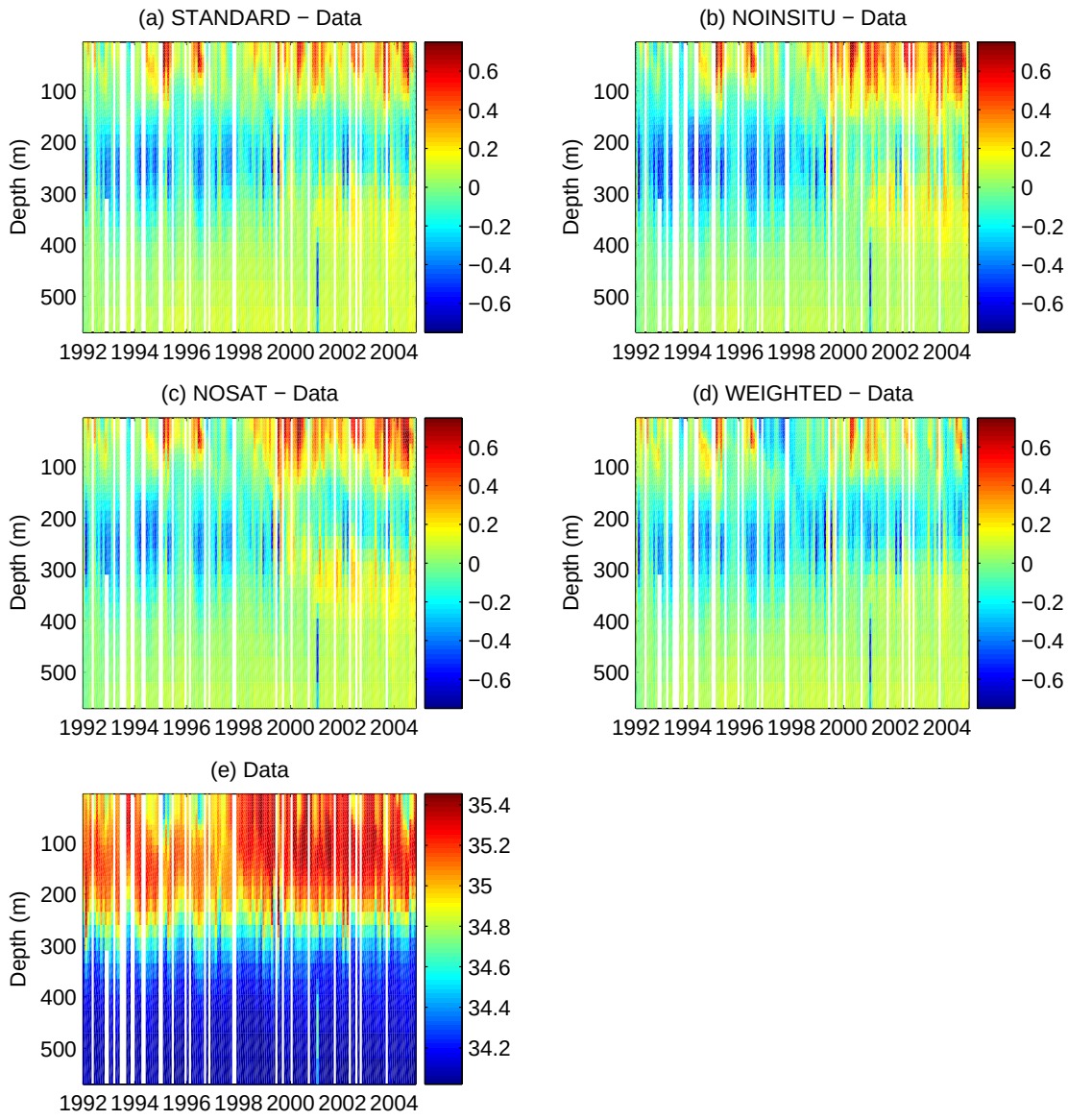

Figure 3.12: (a)-(d) Salinity difference in the top 500 m between model estimate and data at Station Aloha, for each of the four estimates. (e) The salinity time series at Station Aloha. All units are psu.

The time evolution of the difference between measured and modeled temperature at Station Aloha is shown in Figure 3.11, for each of the four model estimates. The quantity shown in the panels (a) through (d) is model minus data, so that positive values indicate higher temperatures in the model, and negative values indicate higher temperatures in the data. The temperature measurements at Station Aloha are shown in panel (e) for reference. Surface temperature is higher in all four model estimates than in the data. This is caused by problems with the KPP mixed layer model in simulating the wind-induced mixed layer deepening in late summer and the associated cooling of SST (Köhl et al., 2007). The overestimation is weakest in the WEIGHTED time series (panel (d)), while the NOSAT model (panel (c)) has the highest surface temperatures. This disparity in surface temperatures is the strongest in the summer, when stratification in the model is stronger than that in the data. The strong summer stratification is also confined to a shallower depth in the model estimates than in the data, such that in all estimates, the model temperatures at levels below about 100 m are too low. This difference is magnified during the fall of each year, when summer stratification breaks down earlier in the model than in the data, with the result in all estimates, the modeled subsurface temperatures are as much as three degrees cooler than the data. The difference in thermocline structure results in cooler temperatures in the model estimates to a depth of almost 500 m. From about 1992-1997, the largest differences are centered at 200-250 m, while from 1998-2004 they are at a shallower depth of about 150 m. Unlike surface temperature, which was measured more accurately by the WEIGHTED experiment, the subsurface bias has similar magnitude in all experiments. The basic structure of overestimated surface temperatures, a too-shallow thermocline, and underestimated subsurface temperatures persist throughout the time series, and are consistent in all model estimates.

The time evolution of differences in salinity between the four model estimates and the observations are shown in Figure 3.12. As with temperature, the quantity shown is model minus data, so that positive values indicate higher salinity

in the model and negative values indicate higher salinity in the data. The structure of the differences is similar to temperature, although the subsurface structure of salinity is more complicated. At the surface, the modeled salinity is higher than the data. This overestimation persists to a depth of more than 100 m in salinity, as opposed to only 50 m in temperature. As we see in Figure 3.12(e), which shows the salinity measurements at Station Aloha, salinity has a subsurface maximum, and then decreases with depth. This subsurface maximum is shallower in the model than in the data. Below the subsurface maximum, modeled salinity is consistently lower than measured salinity, particularly from about 200 to 300 m depth. Although this basic structure persists in all estimates throughout the time series, its magnitude changes. During 1998, the difference between modeled and measured salinity in the top 100 m increases markedly. We can see from the raw data in Figure 3.12(e) that measured salinity increased at this time, and the difference plots indicate that in all four model estimates, the model salinity increased by more. After this shift, the negative surface bias dominates the difference figures, and the bias in the thermocline weakens. The structure of the differences is the same in all four estimates, but the magnitudes are smallest in the WEIGHTED estimate.

The differences between estimated and measured temperature as a function of depth are shown in Figures 3.13(a) and 3.13(c). In Figure 3.13(a), which shows the mean difference of modeled minus observed temperature, we see that while all solutions overestimated surface temperature, the WEIGHTED model is, on average, the closest. However, within 50 m of the surface, all four solutions become cooler than the data. Below the surface, the NOSAT estimate has the lowest bias throughout the depth range. Below about 200 m, the WEIGHTED estimate is biased lower than any of the other estimates. WEIGHTED underestimates temperature by as much as 1.5° at 250 m depth. The NOINSITU and STANDARD model estimates are similar at all depths, with NOINSITU slightly better than STANDARD. However, with the mean removed, the RMS differences between the data and the WEIGHTED model estimate are smaller than those of

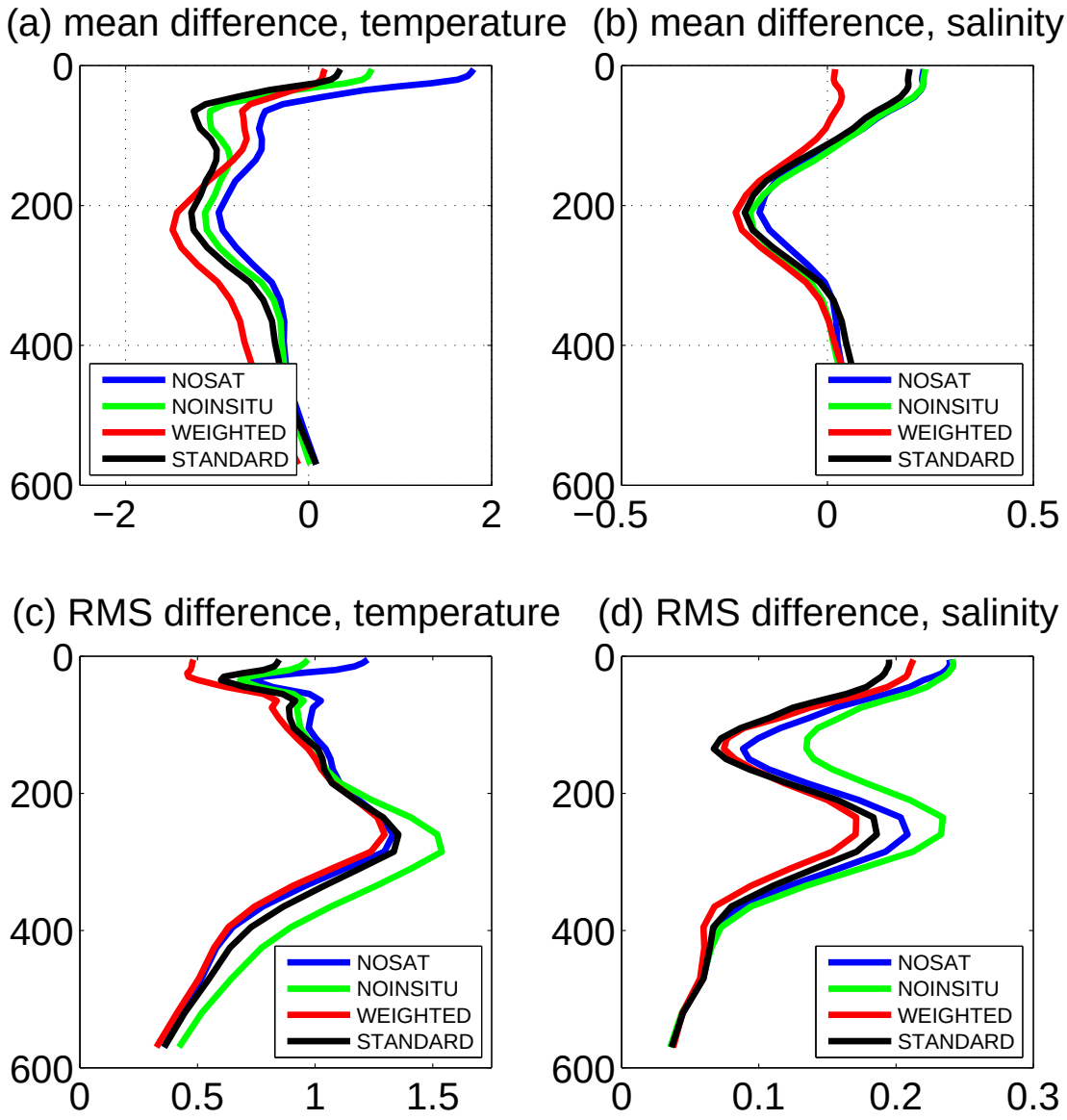

Figure 3.13: (a) Mean difference between model estimated temperature and measured temperature at Station Aloha as a function of depth, for each of the four experiments. (b) Same as (a), for salinity. (c) RMS difference between model-estimated temperature anomaly and measured temperature anomaly at Station Aloha as a function of depth. (d) Same as (c), for salinity.

any of the other estimates, for the full depth range shown (Figure 3.13(c)). At the surface, the NOSAT estimate has the highest RMS difference, but below 200 m, the NOINSITU estimate is the least accurate. This indicates that when the bias is removed, the WEIGHTED experiment provides the model temperature estimate with the time evolution most similar to the measured profile.

Mean and RMS differences between modeled and observed salinity as a function of depth are shown in Figures 3.13(b) and 3.13(d). In Figure 3.13(b), the mean difference is clearly the smallest in the WEIGHTED model estimate at the surface, where the other three solutions overestimate by more than 0.2 psu. Below 100 m, though, all four model estimates behave similarly, underestimating the salinity at around 200 m depth by about 0.2 psu and then estimating salinity correctly below about 400 m. The only significant difference in the mean estimates is the accuracy of the WEIGHTED estimate at the surface. Figure 3.13(d) shows that the STANDARD model estimate has the smallest RMS difference from the data at the surface, and that the STANDARD and WEIGHTED estimates are nearly identical for the top 200 m. The WEIGHTED estimate has a slightly smaller RMS than the STANDARD estimate from 200 m to 400 m. The NOINSITU and NOSAT estimates have higher RMS differences than either of the other two through the top 400 m. Below 400 m all four model estimates become nearly indistinguishable. This confirms that while there is some bias in the WEIGHTED estimate, its simulation of the time evolution of salinity is at least as accurate and often more accurate than any of the other estimates.

3.4.2 Ocean Station Papa

Another independent time series has been recorded in the northeastern Pacific Ocean at 50°N, 145°W (Whitney and Freeland, 1999). This station, known as Ocean Station Papa (OSP), was originally established in 1949. During the time period spanned by the model estimates, measurements were taken approximately 3-6 times per year. While this is slightly less frequent than Station Aloha, there

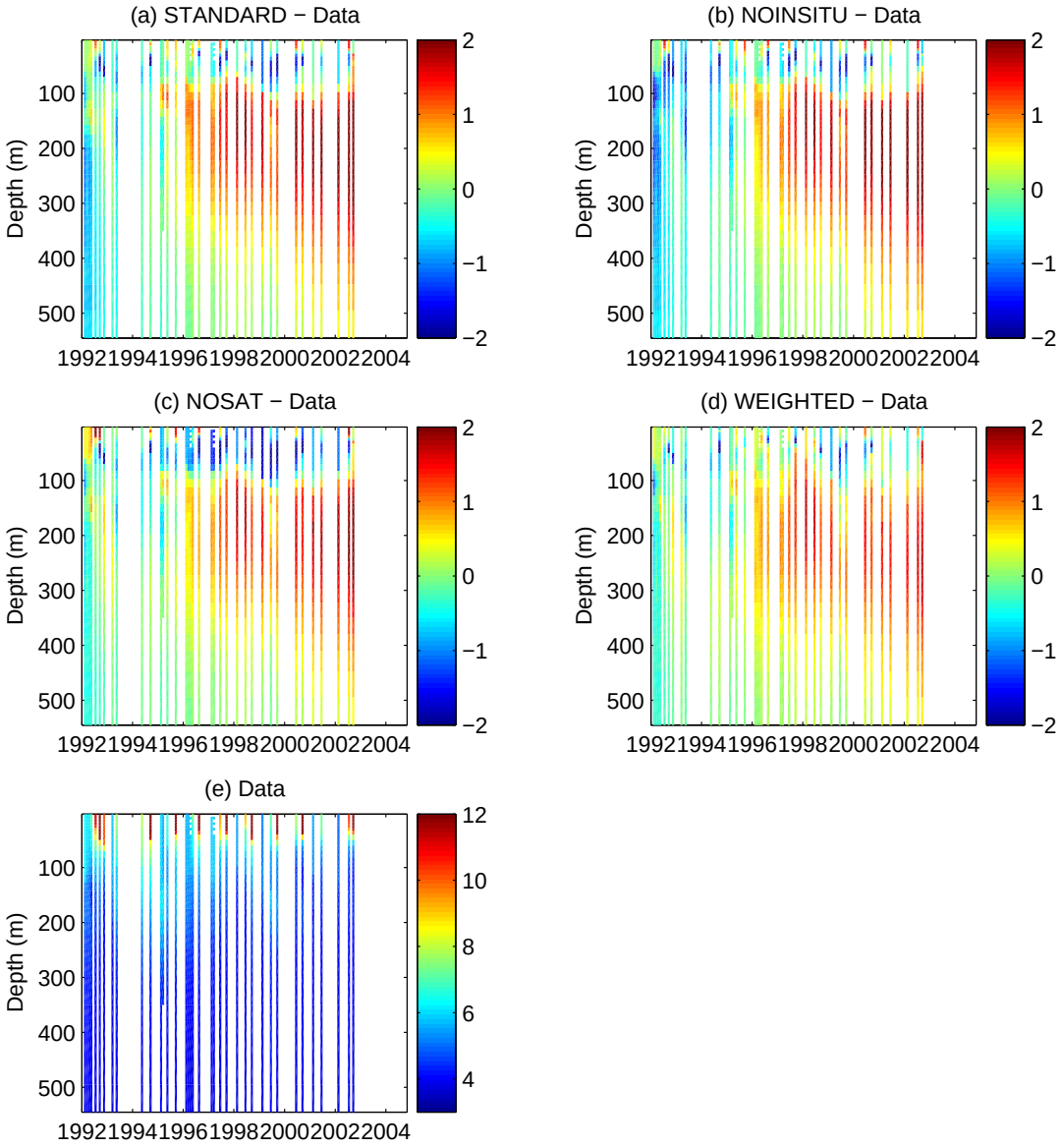

Figure 3.14: (a)-(d) Temperature difference in the top 500 m between model estimate and data (model minus data) at OSP, for each of the four estimates. (e) The temperature time series at OSP. All units are °C.

.

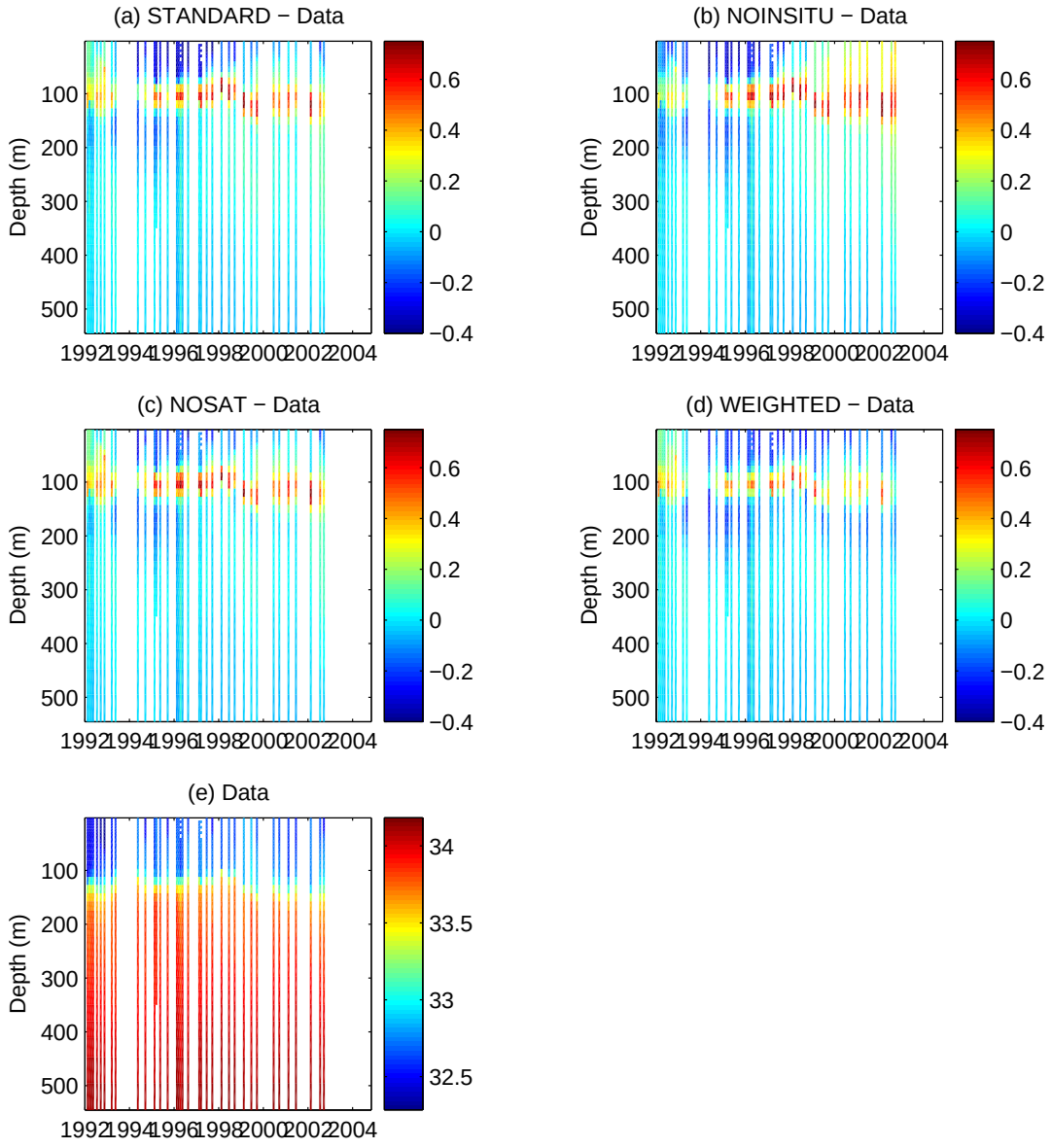

Figure 3.15: (a)-(d) Salinity difference in the top 500 m between model estimate and data (model minus data) at OSP, for each of the four estimates. (e) The salinity time series at OSP. All units are psu.

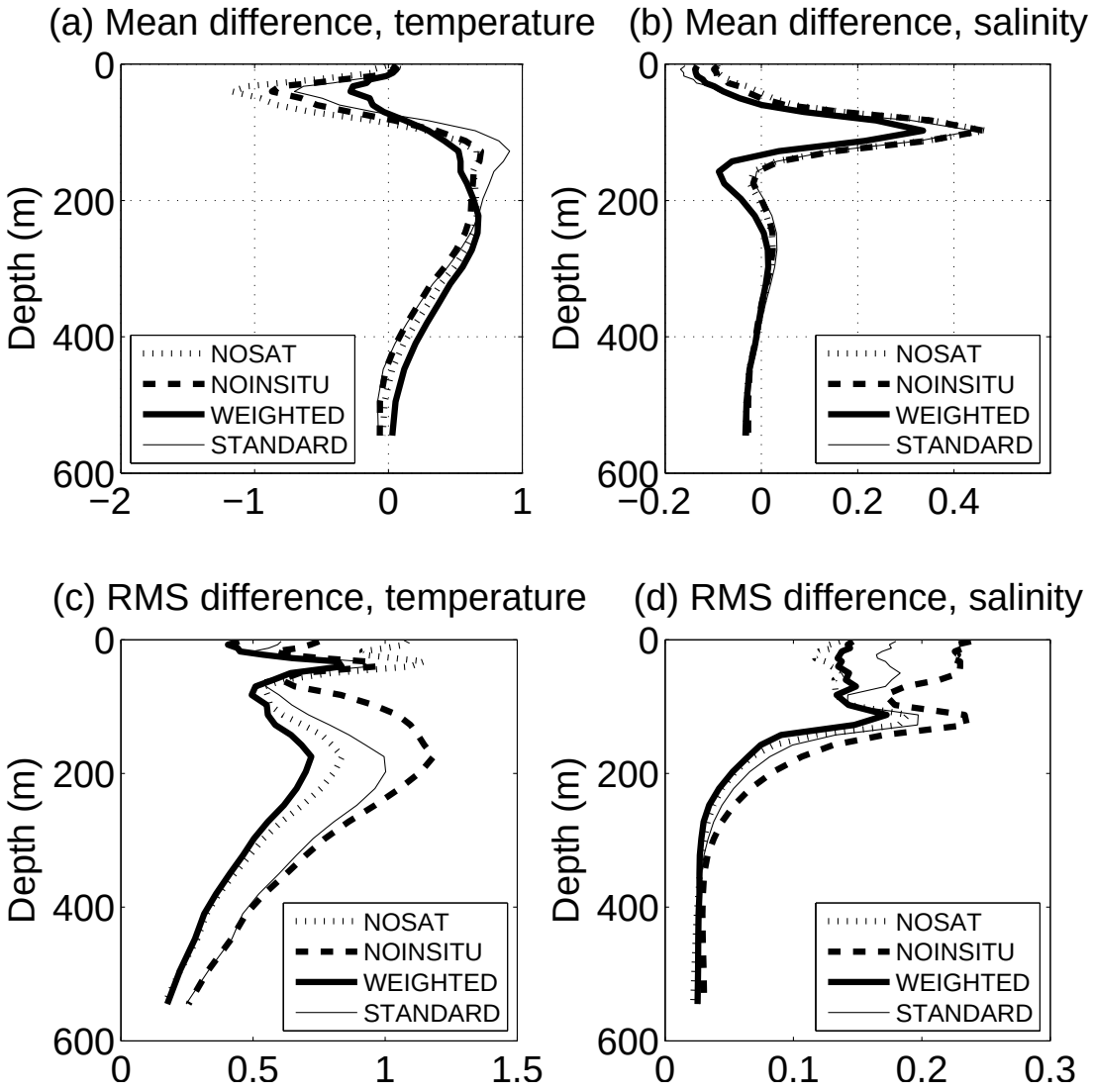

Figure 3.16: (a) Mean difference between model estimated temperature and measured temperature at OSP as a function of depth, for each of the four experiments. (b) Same as (a), for salinity. (c) RMS difference between model-estimated temperature anomaly and measured temperature anomaly at OSP as a function of depth. (d) Same as (c), for salinity.

are still a significant number of profiles for comparison with the model output.

The time evolution of the difference between data and model temperatures at OSP is shown in Figure 3.14 for each of the model estimates. As for Station Aloha, the quantity shown is model minus data, so positive values indicate higher temperatures in the model and negative values indicate higher temperatures in the data. All four solutions underestimate the surface temperature throughout the time series, by as much as three degrees at certain points. Starting in about 1996, observed temperatures between 100 and 300 m depth are significantly cooler than the model estimates. Panel (e) shows that observed temperatures are not changing significantly, so these changes must come from a continual warming in the model estimates. The warming deepens to almost 500 m by the end of the time series, reaching magnitudes of up to two degrees in all four model estimates. The structure of the differences is the same in all four estimates, with the main difference being that both the underestimation at the surface and the subsurface warming have smaller magnitude in the WEIGHTED estimate.

The time evolution of modeled minus observed salinity at OSP is shown in panels (a)-(d) of Figure 3.15. The quantity shown is model minus data, so positive values indicate higher salinity in the model and negative values indicate higher salinity in the data. Figure 3.14(e) shows that salinity structure is simpler here than at Station Aloha, with minimum values at the surface, a sharp halocline just below 100 m, and increasing salinity below that point. The main feature of the difference plots is a band of much higher modeled than measured salinity at about 100 m depth. This indicates that the halocline is deeper in the model estimates than in the data. The bias introduced by this difference in halocline structure can reach more than 0.6 psu. This systematic bias in all four estimates indicates that a problem with the mixing is leading to too smooth a halocline. Differences at both shallower and deeper levels than this feature are generally of much smaller magnitude, although the magnitude of the overestimation by the NOINSITU estimate of surface salinity after 2000 is close. In general, the structure

of differences is the same in magnitude and sign in all four model estimates.

Comparisons between modeled and measured temperature and salinity as a function of depth at OSP are shown in Figure 3.16. Figure 3.16(a) shows the mean difference between modeled and observed temperature. The WEIGHTED model only overestimates the mean by a maximum of 0.25 degrees in the top 100 m, which is significantly less than the other three estimates. Below 100 m, the four model estimates have similar structure. Figure 3.16(c) shows that the RMS difference between model and data is smallest for the WEIGHTED estimate everywhere below 100 m. In the top 100 m, the NOSAT estimate is the worst, while below that the NOINSITU estimate is the farthest from the measurements. In salinity, Figure 3.16(b) demonstrates again that the only significant difference is the incorrect halocline structure. The effect is slightly smaller in the WEIGHTED estimate, a result balanced by a slight overestimation of salinity just below the halocline, when all three of the other estimates match the mean salinity closely. Figure 3.16(d) shows that the RMS differences from the data are nearly identical, except that the NOINSITU estimate is somewhat less accurate in the top 150 m.

An important aspect of this comparison is the contrast with the comparison with the Station Aloha profiles. The surface temperature biases are of the opposite sign in the two locations. This indicates that rather than a large-scale consistent bias, the differences between model estimates and measurements are location-specific. However, at both stations, the WEIGHTED model provided the most accurate overall estimate of temperature and salinity.

3.5 Comparison with Global Estimate

Of the four experiments described in this work, the WEIGHTED estimate produces the best results when compared with assimilated data as well as independent data. However, similar methods of data assimilation have produced global, converged solutions, such as the ECCO-GODAE solution used for bound-

Table 3.2: Normalized costs of the assimilated datasets, for the WEIGHTED regional model and ECCO-GODAE model.

	WEIGHTED (iteration 30)	ECCO-GODAE (iteration 177)
CTD T	2.29	3.05
CTD S	1.27	1.63
Argo T	2.99	4.26
Argo S	1.78	1.99
XBT	3.25	4.26
SSH (altimetric height)	2.52	1.32
SST (Reynolds)	1.60	2.01
SSS	1.83	2.40
SST (TMI)	1.58	1.89

ary conditions. It is important to determine how our estimate compares with these other solutions.

3.5.1 Model-Data Misfits

One metric for comparison between the ECCO-GODAE solution to the estimate from the WEIGHTED regional model is the normalized cost. In order for these changes to be directly comparable, the normalization uses prior variances from the STANDARD experiment. Costs for the ECCO-GODAE model are limited to the North Pacific region. Thus differences in normalized costs are only due to differences in the model-data misfit. These costs are listed in Table3.2.

For almost all data, the WEIGHTED estimate has lower costs than the ECCO-GODAE estimate. There are various reasons for the differences. First, the WEIGHTED estimate benefits from increased vertical resolution. Additionally, a regional model has an advantage in that the assimilation will focus on features specific to the region of interest. That is, in a global model, errors or misfits in the Antarctic Circumpolar Current might dominate the assimilation simply as a result of the magnitude of the signals in that region, with misfits in the Kuroshio having less impact on the final estimate. In the North Pacific regional model,

the Kuroshio itself is the largest feature, and therefore misfits and changes in that region have a significant impact on the final estimate. However, the most significant difference between the two estimates is the increased weight on the subsurface data in the WEIGHTED experiment. It is clear that this change has improved the model's estimation of subsurface data, as well as most components of surface data. From the difference in SSH cost between the two estimates, it is evident that the improvement in the match to the subsurface structure is not without cost to the surface data. While it is higher than the corresponding value for the ECCO-GODAE estimate, the cost of SSH is not unreasonably high. The other surface fields of SST and SSS have lower normalized costs in the WEIGHTED estimate than in the ECCO-GODAE estimate. It is also important to note that as was previously mentioned, the WEIGHTED model is not fully converged. Further iterations are expected to reduce costs of all model-data misfits and provide a more accurate final solution. The preliminary results presented here are only intended to emphasize the importance of using the available subsurface data to their full potential, rather than using such large error bars that they have only minimal effects on the final state estimate produced by the model.

Maps of RMSD of heat content anomaly and SSH anomaly provide another comparison between the WEIGHTED and ECCO-GODAE estimates (Figure 3.17). The first column displays RMSD between XBT-derived heat content anomaly and model-estimated heat content anomaly. Panel (a) shows the result from the WEIGHTED estimate and panel (c) the ECCO-GODAE estimate. Panel (e) shows the difference, ECCO-GODAE minus WEIGHTED. Positive (red) values indicate that ECCO-GODAE has a higher RMS difference, and thus that the WEIGHTED estimate is more accurate. In much of the region, and particularly in the Kuroshio region, the WEIGHTED RMSD is lower than that of the ECCO-GODAE estimate. This implies that the WEIGHTED experiment provides a more accurate estimate of heat content anomaly as measured by XBTs. The second column of Figure 3.17 shows RMSD between measured and modeled

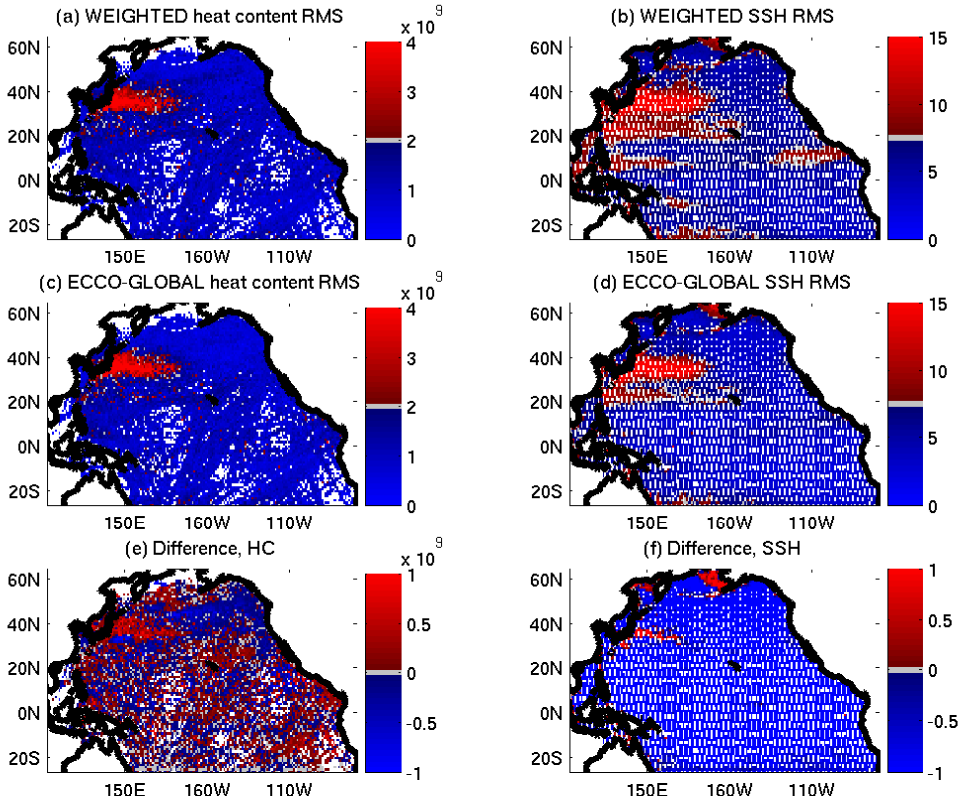

Figure 3.17: (a) RMS differences between WEIGHTED estimate of heat content and XBT-derived heat content; (b) Same as (a), for SSH instead of heat content; (c) Same as (a), for ECCO-GODAE instead of WEIGHTED; (d) Same as (a), for ECCO-GODAE SSH instead of WEIGHTED heat content; (e) (c) minus (a); (f) (d) minus (b). Heat content units are joules, SSH units are cm.

SSH anomaly. Panel (b) shows the WEIGHTED RMSD, panel (d) shows the ECCO-GODAE RMSD, and panel (f) shows the difference, ECCO-GODAE minus WEIGHTED. In this case the map is dominated by negative (blue) values, indicating that WEIGHTED estimates of SSH anomaly are less accurate than ECCO-GODAE estimates almost everywhere. This confirms what was suggested in Table 3.2 by the higher normalized cost of SSH. However, the RMS differences between the WEIGHTED estimate and the data are still not unreasonable, and with more iterations and better convergence, the accuracy of this estimate will continue to improve.

3.5.2 Surface Forcing Adjustments

Through the adjoint method, the WEIGHTED state estimate has reduced its model-data misfits such that it now matches much of the data more accurately than the ECCO-GODAE state estimate. These improvements have been achieved in a dynamically consistent way by adjusting the fluxes of heat, freshwater, and momentum imparted by the surface forcing. Since both the WEIGHTED and the ECCO-GODAE estimates were initially forced by NCEP reanalysis fields, their adjustments can be compared easily. Although the adjustments are made at two-day intervals, only monthly means of forcing are available for the ECCO-GODAE solution, so the comparisons are made between monthly adjustments.

The normalized costs for each of the four forcing terms are listed in Table 3.3 for both of the estimates. As before, prior variances from the STANDARD model are used for the normalization, and the calculation for the ECCO-GODAE estimate is restricted to the North Pacific region. In this case, all results are significantly less than one, indicating that the adjustments made to the forcing terms are, on average, much smaller than the assumed prior errors.

The first two terms in Table 3.3 are for zonal and meridional wind stress adjustments. For these parameters, normalized costs of the adjustments made by the WEIGHTED and ECCO-GODAE estimates are similar, indicating that the

Table 3.3: Normalized costs of the adjustments to the surface forcing, for the WEIGHTED regional estimate and ECCO-GODAE estimate.

	WEIGHTED	ECCO-GODAE
Zonal Wind Stress	0.0924	0.0606
Meridional Wind Stress	0.0395	0.0278
Heat Flux	0.127	0.211
Freshwater Flux	0.0102	0.107

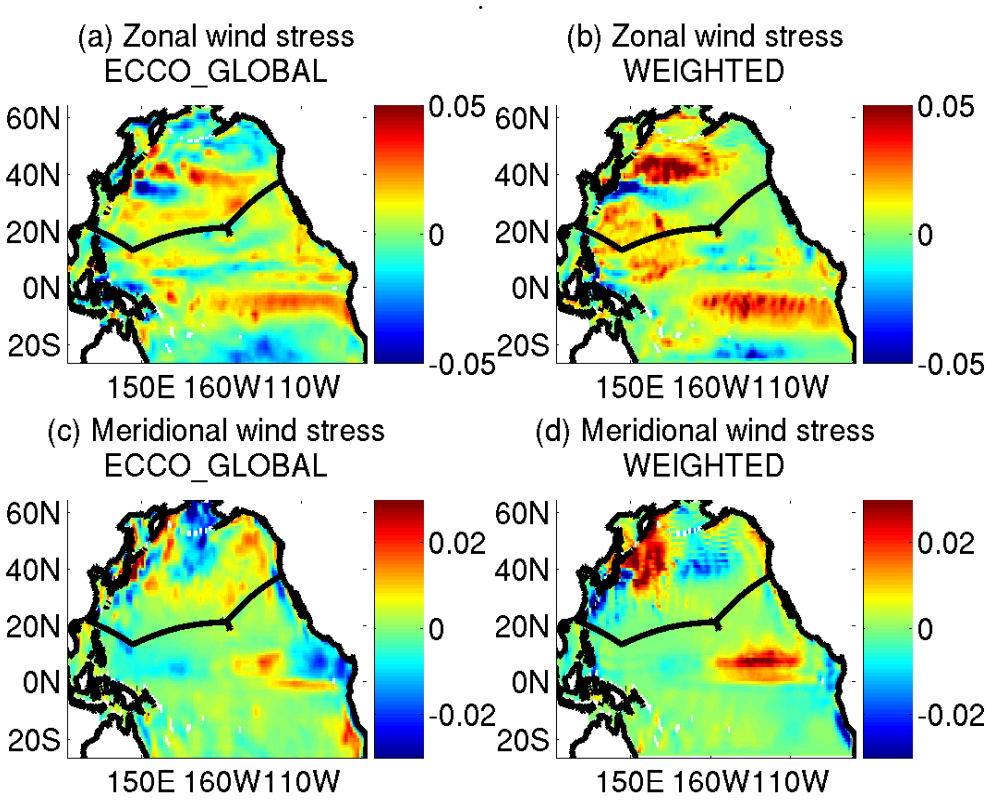

Figure 3.18: The mean adjustments to the zonal and meridional wind stress for the ECCO-GODAE and WEIGHTED model solutions. Units are N/m^2.

changes made to these parameters are of the same order of magnitude. It is important to ensure that changes made to these parameters are reasonable in spatial structure as well. The mean adjustments to the zonal and meridional wind stress from the WEIGHTED and ECCO-GODAE estimates are shown in Figure 3.18. The main signal in zonal wind stress forcing is a strengthening of the major wind systems: the trades, near the equator, and the westerlies in the northern Pacific. Prior research indicates that the wind fields of the NCEP reanalysis are biased low relative to shipboard wind measurements (Smith et al., 2001). This supports the adjustments evident in both model solutions. In meridional wind stress, there are more differences between the two solutions. In both maps, adjustments are concentrated north of 45°N, except for a feature at the equator on the east side of the basin. The WEIGHTED estimate has an increase in northward wind stress near the equator on the east side of the basin, while the ECCO-GODAE estimate has a much weaker increase at that location, countered by a negative signal farther east. Both solutions have their strongest adjustments in the north part of the basin, but in the ECCO-GODAE estimate the dominant feature is a decrease in meridional wind stress in the Bering Sea, while in the WEIGHTED estimate there is a strong positive adjustment just east of the Okhotsk Sea. Despite these differences in magnitude, the pattern of strong adjustments in the northwest region of the basin is the same in both estimates. As noted, general patterns of zonal wind stress adjustments are also the same in both estimates. This supports the hypothesis that although the WEIGHTED estimate is not fully converged, the adjustments made to the surface forcing by the assimilation thus far are reasonable.

The third and fourth terms in Table 3.3 are the normalized costs of heat and freshwater fluxes. In both cases, the ECCO-GODAE estimate has made much stronger adjustments than the WEIGHTED estimates. In the heat flux, the ECCO-GODAE normalized cost is twice the WEIGHTED normalized cost. In freshwater flux the difference is close to an order of magnitude. Maps of the mean adjustments, seen in Figure 3.19, confirm this conclusion.

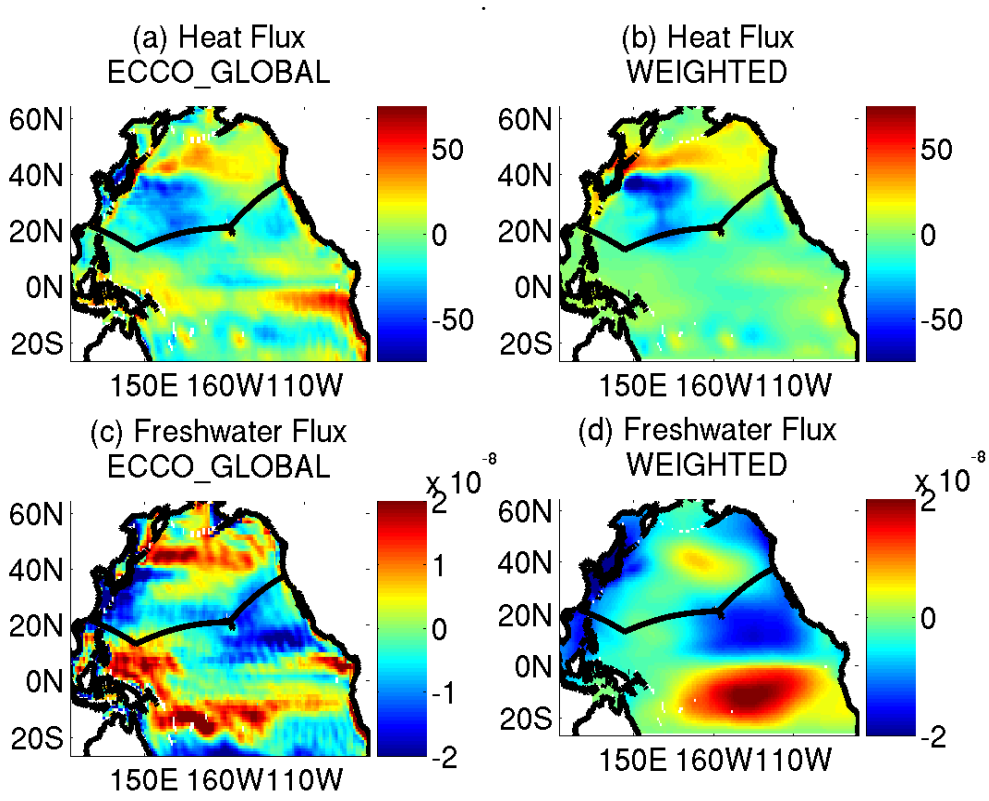

Figure 3.19: The mean adjustments to the heat and freshwater fluxes, for the ECCO-GODAE and WEIGHTED model solutions. Heat flux units are W/m^2, freshwater flux is m/s.

First we consider the heat flux adjustments. Overall, both estimates indicate that a net decrease in heat flux, equivalent to an increase in heat absorption and storage by the ocean, is a necessary adjustment to the forcing field. In Figure 3.19(b), the WEIGHTED estimate has some of the same features seen in the ECCO-GODAE estimate (Figure 3.19(a)), particularly a decrease in surface flux (more heat into the ocean) in the western North Pacific just south of the Kuroshio and an increase in surface flux (more heat into the atmosphere) north of this region. The strongest feature in the ECCO-GODAE mean heat flux adjustment is the region of strong increased heat flux (less heat into the ocean) over the Pacific cold tongue region. This feature is completely absent from the WEIGHTED estimate. This could be a result of a less-converged result, or a fundamental difference in the solutions. More iterations are necessary to be certain. Overall, the comparison indicates that thus far, the heat flux results are reasonable.

Freshwater flux adjustments are also shown in Figure 3.19. In total, both WEIGHTED and ECCO-GODAE indicate that a net flux of freshwater into the ocean (precipitation and/or runoff) is necessary. Spatially, some basic features are similar, such as an increase in evaporation (negative) south of the equator and an increase in precipitation (positive) north of the equator. There are also distinct differences between the estimates. The ECCO-GODAE estimate has a strong feature in the North Pacific near 45°N indicating decreased precipitation. A similar feature is present in the WEIGHTED estimate, but is much weaker. The ECCO-GODAE adjustments also indicate increased precipitation in the tropics in the west, but this feature is entirely missing in the WEIGHTED result. In general, the ECCO-GODAE solution has much more structure on small spatial scales than the WEIGHTED estimate. As with heat flux, this could indicate fundamentally different results, or it could be a sign that the solution is not yet fully converged. More iterations are necessary, but the similarities between the two results are encouraging.

3.6 Discussion and Conclusions

The results of state estimation are dependent on many factors, including the model resolution, the data being assimilated, and the error bars assigned to both the data used as constraints and the control variables being adjusted to improve the model's skill in simulating the observations. The purpose of this study was to compare the influence of surface observations as constraints on ocean state estimates to that of subsurface observations. To that end, three model experiments were constrained by subsets of the available data to analyze the relative importance of those data to the solution. The control experiment (STANDARD) assimilated all available data, a second experiment assimilated only subsurface data (NOSAT), and a third assimilated only surface data (NOINSITU).

Comparisons between the resulting state estimates demonstrate the importance of using both surface and subsurface data to obtain the best possible estimate of the time-varying state. The NOINSITU experiment matches SSH more accurately than the STANDARD estimate, but is deficient in estimating heat content. The NOSAT experiment, conversely, is accurate in its heat content estimate but highly inaccurate in estimation of SSH. In comparisons with independent data at Station Aloha, the NOSAT estimate had a significant negative temperature bias relative to the data, and the NOINSITU estimate had high RMS differences indicating inaccurate representation of subsurface variability in both temperature and salinity. At OSP, the NOINSITU estimate again did poorly at representing subsurface variability. In general, the STANDARD experiment provided a state estimate that was consistently more accurate than both NOSAT and NOINSITU, demonstrating the importance of using all available data.

To determine the model's sensitivity to the weights used on the constraining data, a fourth experiment (WEIGHTED) was performed. Both the STANDARD and WEIGHTED experiments were constrained by all available data, but with different weighting on the subsurface observations. Overall, the WEIGHTED

estimate provides a more accurate solution. In total cost, the simplest measure of overall accuracy, the percentage decrease was greatest for the WEIGHTED estimate. In estimated heat content, the WEIGHTED solution had the lowest RMSD and the highest correlation with the heat content calculated from optimally interpolated XBT data. In comparisons with independent data at Station Aloha and OSP, WEIGHTED temperature and salinity estimates were generally less biased, particularly in the top 100 m, and had lower RMS differences at depth. The EOFs of SST and SSH from the WEIGHTED estimate captured the main signals seen in the data. It is important to note that the WEIGHTED solution is less accurate than the STANDARD solution when comparing estimates of SSH anomaly, but overall, the increased weights on the subsurface data in the WEIGHTED experiment have led to a more accurate model solution.

A comparison of the WEIGHTED estimate with a global, data-assimilating model solution (ECCO-GODAE) reinforced the conclusion that the increased weights on the subsurface data have improved the results. Again, the only shortcoming of the WEIGHTED solution is in the estimation of SSH, which is expected to improve with further iterations. The comparison with the global estimate also demonstrated that adjustments to control parameters from the WEIGHTED experiment have similar patterns to those from the ECCO-GODAE estimate. Whether differences are true results of the model or are indicators of a lack of convergence remains to be seen, but initial results are encouraging.

An important point to remember, which was mentioned briefly earlier, is possible biases within the datasets themselves. Recent research has indicated that there may be systematic, time-varying biases in XBT measurements as a result of changes in instrumentation (Gouretski and Koltermann, 2007). The error estimates used to determine weights include an assumption that error is uncorrelated, but systematic bias is highly correlated and cannot be accounted for in this way. Additionally, such errors result in inconsistencies between the various datasets. A time-varying change in XBT bias, for example, would indicate variability in dy-

namic height that would not be reflected in altimetric height variability, not to mention disagreement with unbiased CTD or Argo temperature measurements. Currently, there is ongoing research in determining a correction for the possible systematic errors in the XBT dataset (Wijffels et al.). Such a correction will provide a more accurate dataset and will in turn lead to an improved ocean state estimate.

This analysis was not intended to determine the optimal weights for assimilation of subsurface data. The goal was to determine if the subsurface observations could be matched more accurately without a loss of realism in the overall solution, which might be expected if the aliasing of mesoscale noise into the estimate were too significant. The results of the WEIGHTED experiment indicate that some increase in the weights when assimilating these data provides an improved final product, with increased accuracy in the estimation of subsurface structure, as well as appropriate evolution of forcing adjustments. The weights used in the WEIGHTED experiment, when applied to a corrected XBT dataset and with further iterations for convergence, could provide an improved ocean state estimate for analysis of the dynamics of the North Pacific between 1992 and 2004.

Chapter 3 will be submitted for publication with minor modifications as Douglass, E., D. Roemmich, and D. Stammer, Data-sensitivity of the ECCO state estimate in a regional setting. The dissertation author was the primary investigator and author of this paper.

4

Interannual Variability in North Pacific Heat and Freshwater Budgets

4.1 Introduction

The transport of heat and freshwater by the large-scale ocean circulation is a critical component in the global climate system. A better understanding of the magnitude and frequency of variability in the ocean is essential to determining its role in the climate and ecosystems we live in. Even synoptic estimates of heat and freshwater transport are difficult to obtain, and the details of variability on longer time scales remain to be explored. However, as data accumulate and global and regional-scale models are developed and refined, estimates of mean transports are improving and variability on a range of temporal and spatial scales is being quantified.

The heat transport in the Pacific Ocean has been the subject of much research. The magnitude of this component of the global heat budget has been estimated both directly from hydrographic transects and indirectly from basin integrals of surface fluxes. Early hydrographic estimates left even the sign of this

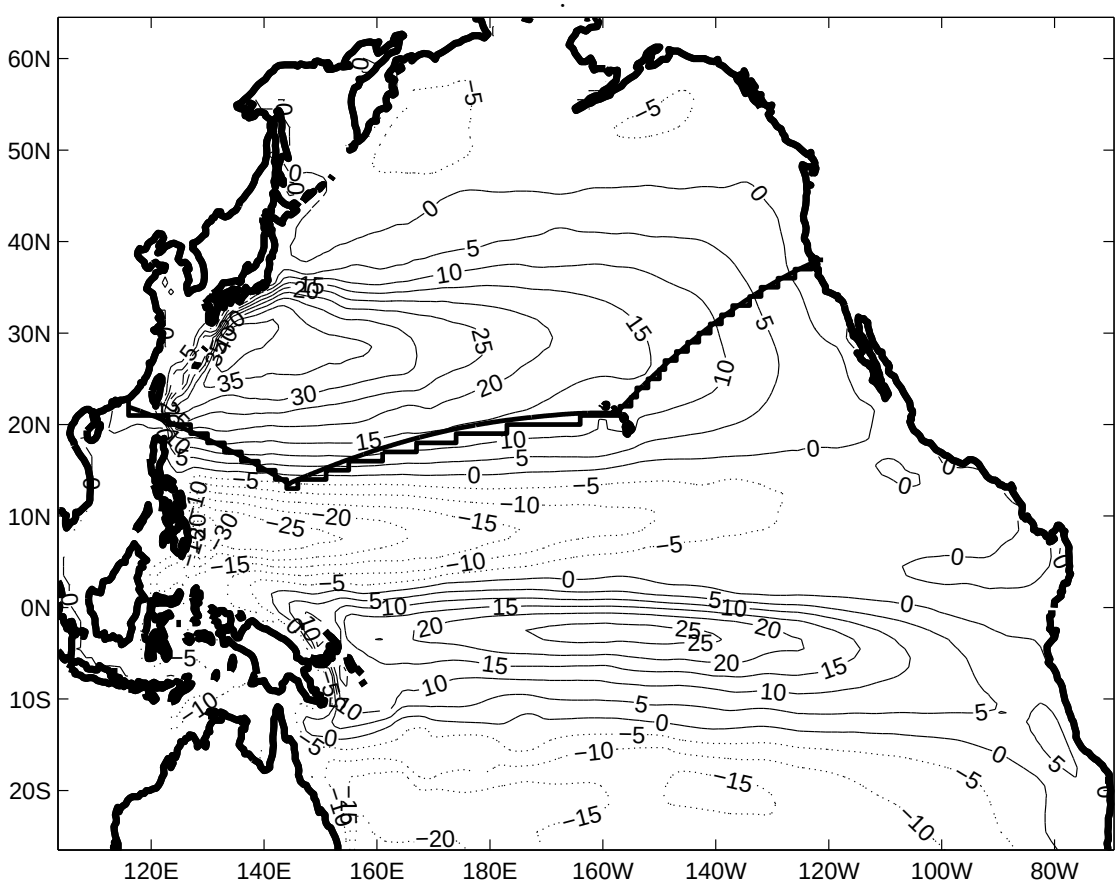

Figure 4.1: Area of study. Contours indicate the mean transport streamfunction in the top 800 m as it results from the ECCO state estimate. The mean track of line PX37 is shown, as is the grid-box following approximate track used to eliminate interpolation issues in the model.

transport in dispute, but more recent work has determined that heat is transported poleward, from the equator where heating takes place to regions where heat is radiated to space. Recent direct estimates of heat transport into the North Pacific from hydrography, including those from Bryden et al. (1991), Roemmich et al. (2001), and Ganachaud and Wunsch (2003) have converged between 0.5 and 1.0 pW. Air-sea estimates, based on the concept that heat transported poleward must be radiated to space, range from 0.8 to 1.03 PW depending on the surface flux product used (from Roemmich et al. (2001)).

Freshwater transport is also important, but salinity has been measured less often and with less coverage than temperature. As a result, large-scale estimates of freshwater transport are scarce. Ganachaud and Wunsch (2003) use hydrographic sections from the World Ocean Circulation Experiment (WOCE) and various surface climatologies to calculate positive freshwater flux into the North Pacific, but caution that uncertainty is very large. Precipitation in the subpolar regions and evaporation in the subtropical regions combine in such a way that even the sign of freshwater flux into the North Pacific is not well known.

In this work, a long time series of high-resolution expendable bathythermograph (XBT) transects and a regional ocean state estimate from a data-assimilating numerical model are used to estimate the time-mean and variability of heat and freshwater transport in the North Pacific between 1992 and 2004. The XBT transect, at approximately 24°N, provides a southern boundary to a closed region for which budgets can be calculated. The advective component of transport can be estimated from the geostrophic velocity, temperature, and salinity available from hydrographic transects, as well as from the output of the model. The model also provides heat and freshwater flux fields which comprise the surface component of the budget. For both heat and freshwater, the sum of the advective and surface components provides an estimate of the time-varying storage in the region north of the XBT transect. Broadscale XBT estimates of heat content provide an independent check for the heat storage component.

The structure of the paper is as follows. Section 2 provides a brief description of the model and the data used in this analysis. Section 3 analyzes the volume transport in the closed region of the North Pacific. Section 4 provides a complete heat budget for that region, and section 5 provides the freshwater budget. Section 6 analyzes some aspects of forcing of the variability, and section 7 has discussions and conclusions.

4.2 Model and Data

4.2.1 Model

This analysis uses output from a data-assimilating model developed by the Estimating the Climate and Circulating of the Ocean (ECCO) Consortium (see Stammer 2002a). This model has been developed to provide dynamically consistent estimates of time-varying ocean circulation by using the adjoint method to constrain the MIT general circulation model with ocean data. The model runs forward to estimate the time-varying ocean state, and then calculates a cost function from the misfit between the resulting state estimate and the constraining data. The adjoint of the model is then used to obtain the gradient of this cost function with respect to the model variables. A standard descent algorithm uses these gradients to produce adjustments to the surface fluxes of heat, freshwater, and momentum to bring the model into closer agreement with the data while maintaining dynamical consistency. The process is repeated iteratively to minimize the costfunction. This approach to data assimilation is explained in further detail in Stammer (2002b).

To obtain the state estimate used in this analysis, the ECCO model was used in a regional setting in the Pacific Ocean north of 26°S. The estimate was performed for the time period from 1992-2004. Constraining data include hydrography, satellite altimetry, sea surface temperature and salinity, profile data from floats, drifter-derived velocities, and winds from scatterometry. The state estimate used in this analysis results from assimilating all subsurface data with increased

weights relative to the surface data, to increase their relative influence on the solution. A detailed analysis of the weighting scheme used here and comparison with other state estimates is presented in Chapter 3 of this dissertation. The model has horizontal resolution of 1° in latitude and longitude and 50 vertical levels. The initial surface forcing used was provided by the National Center for Environmental Prediction (NCEP). Output includes monthly estimates of temperature, salinity, and the three components of velocity (zonal, meridional, vertical) and daily estimates of sea surface height, as well as the adjustments to the surface forcing necessary for a dynamically consistent product.

As noted in Chapter 3, there are some inconsistencies between the data sets in the state estimate as performed thus far. Specifically, a time-varying bias due to changes in XBT instrumentation has yet to be removed. When such corrections become available, this analysis will be refined.

4.2.2 XBT Data

The data used in the present work consist mainly of temperature profiles from XBT measurements along ship track PX37 (Figure 4.1). Collection of temperature profiles from a cargo ship along this track from San Francisco, CA, to Honolulu, HI, to Guam, to Hong Kong began in 1991 and continues to the present. Cruises take place approximately every three months; between 1992 and 2004, the time period of interest, there were 49 cruises. These measurements have high along-track spatial resolution, ranging from 50 km in the open ocean to 10 km near shallow topography or interesting features. The probes measure temperature to a nominal depth of 800 m. In addition, occasional expendable conductivity-temperature-depth (XCTD) probes and, in recent years, profiles from Argo floats provide supplemental salinity data. From temperature and salinity, density and thus relative geostrophic velocity can be calculated. The process used to estimate density profiles and determine geostrophic velocities is described in Gilson et al. (1998).

4.3 Volume Transport

From the XBT dataset, the geostrophic transport relative to 800 m can be determined. For comparison with the data, geostrophic transport is calculated from the model output as well. Model temperature and salinity are interpolated spatially to the locations of XBT casts. From these estimates of temperature and salinity, density is determined. Along-track density gradients are used to calculate cross-track geostrophic velocities, and thus, geostrophic transports. Estimates of geostrophic transport across PX37 from the model and from XBT data are shown in Figure 4.2(a). For further clarification of the horizontal structure of these transports, the transect is divided into three segments, using the ports of call as natural break points. The western segment spans the distance from Guam and Hong Kong, and includes the Kuroshio. The middle segment is between Guam and Honolulu, and most transport across this segment is zonal flow in the subtropical gyre. Transport across the eastern segment, between Honolulu and San Francisco, includes large-scale gyre circulation and the California Current along the eastern boundary. All of these features are evident in the mean streamfunction contours on Figure 4.1. Transports across each section are shown in Figure 4.2(b)-(d). It is clear that while there are discrepancies between the total geostrophic transport estimated by the model and that estimated by XBTs, the main features of variability in each section are replicated well. This is confirmed quantitatively by the correlation coefficients between the time series. The correlation between the geostrophic estimates of transport across the full track is only 0.21. However, a close look at the time series indicates that many of the main features are replicated by both model and data estimates. Both time series show a peak in 1995, a subsequent peak in 1998, and lower variability from 2001 to the end of the time series. However, the XBT estimate is biased high by approximately 5 Sv from 1993-1997 and from 1998 to the end of the time series. This time-varying bias is the reason for the low correlation coefficient. When only the section from Hong Kong to Guam

is considered, the correlation increases to 0.76. It is also evident that part of the bias seen in the full section is a result of a high bias in XBT transport in this section, especially in the first few years. The section between Guam and Honolulu is the most highly correlated at 0.86. This section also has the highest variability, with transport as high as 10 Sv northward in the data, but dropping to net southward transport from 1999-2002. This is another section in which the data is biased high relative to the model, almost throughout the time series. In the final section, between Honolulu and San Francisco, the data and model estimates have a correlation of 0.51. This section shows the least bias. Both at the beginning and end of the time series, there is a signal in which the southward transport estimated by the data increases sharply in the data, but not in the model. However, both of these signals are paralleled by an increase in northward transport between Guam and Honolulu, indicating that this could be gyre transport that flowed south east of Hawaii and then turned west (thus crossing both transects) in the data. This could have occurred on a spatial or temporal scale unresolvable in the 1°, monthly model output, such that there was no significant change in the structure of model transport. This is another indication of the differences between high-resolution data and a 1° model. Also shown in Figure 4.2 for comparison with geostrophic estimates is the transport as calculated from the model velocity fields, relative to no motion at 800 m and with Ekman transport removed. In each case, the model geostrophic transport is nearly identical to the model transport from the velocity fields.

Geostrophic velocities are calculated relative to a reference velocity at a level of known motion. In this analysis, the reference level is chosen to be 800 m, the nominal depth of the XBT casts, and reference velocity is zero. The model can be used to assist in analysis of this choice. The volume of transport in the top 800 m that would result from the model's velocity at 800 m is shown in Figure 4.3. The mean transport is 0.70±1.31 Sv. Average transport is northward, but the variability is so large that the mean transport is statistically equivalent to

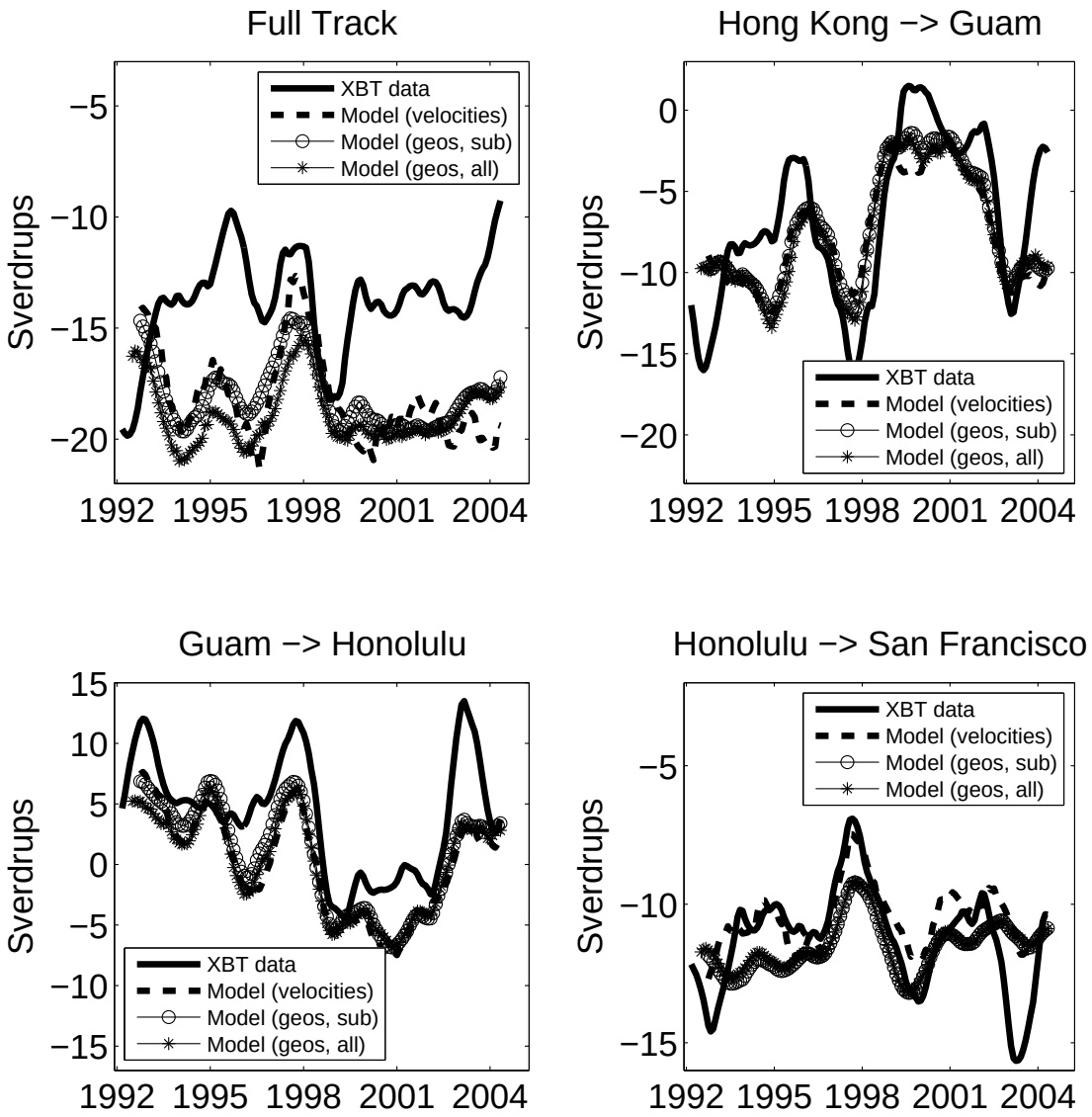

Figure 4.2: Transport across the full track and across each of the geographical sections. Four estimates of transport are shown: geostrophic transport from the XBT data, the full time series of geostrophic transport from the model, geostrophic transport from the model subsampled to XBT cruise times, and transport from the model velocity fields referenced to zero at 800 m and with Ekman transport subtracted.

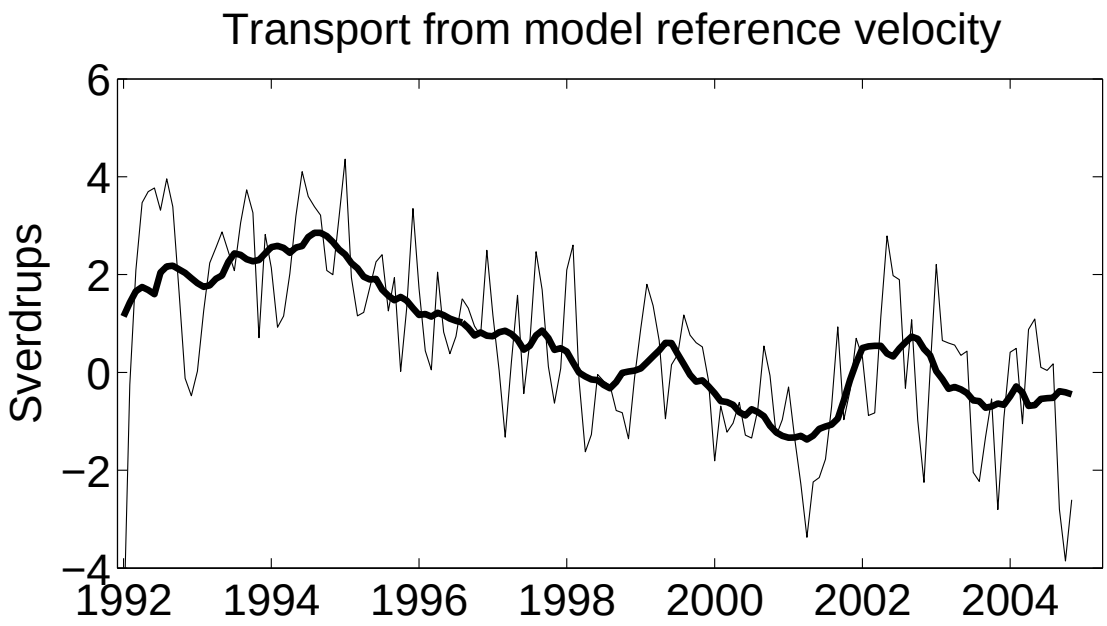

Figure 4.3: Total transport in the top 800 m when the model's velocity at 800 m is used as a reference velocity.

zero. With this in mind, the reference velocity of zero is retained for estimates of geostrophic velocity from the XBT data.

Geostrophic transport is only one part of the full volume budget. Ekman transport is also a significant component of meridional transport in the subtropical North Pacific. This component is determined from the curl of the wind stress. Ekman transports calculated using wind stress estimates from NCEP and from ECCO are shown in figure 4.4. This demonstrates both the magnitude of the adjustments made by the model to the wind stress, and the magnitude and variability of Ekman transport in this region during the time period of interest. It is important to note that although the interannual variability in Ekman transport is small compared to the higher frequency variability, it still has a range of almost 10 Sverdrups, comparable to interannual variability in geostrophic transport.

To examine the full depth volume budget from the model for the region north of PX37, model velocities were interpolated to the exact locations of XBT casts. However, because of the way deep topography is handled in the model, this

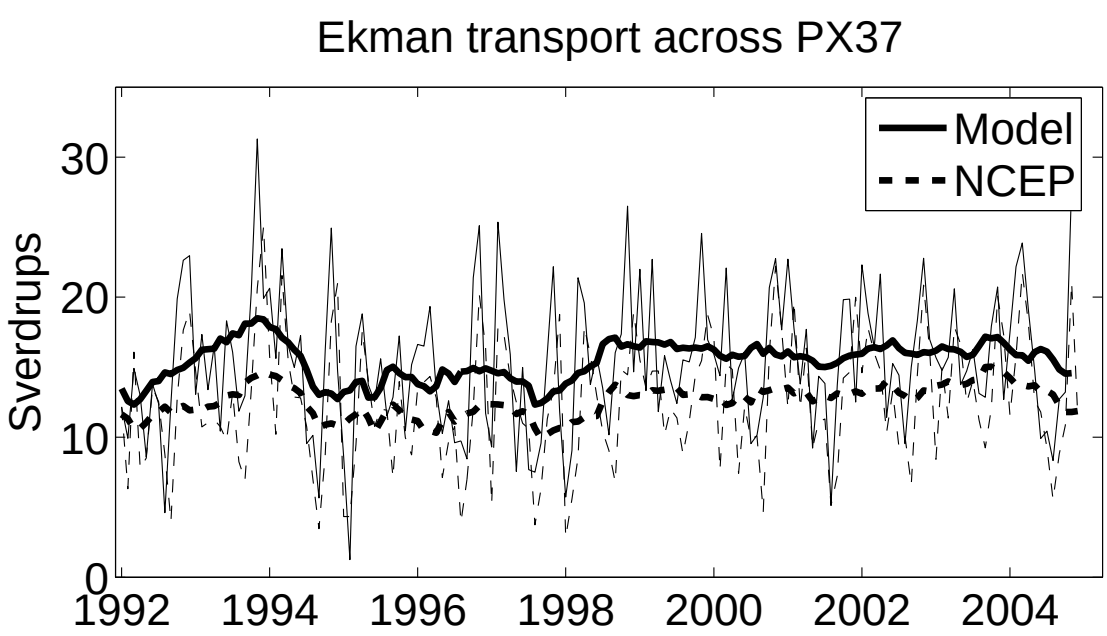

Figure 4.4: Total Ekman transport into the North Pacific across PX37, estimated from NCEP wind stress and model wind stress. Thin solid line is the unsmoothed model transport, thin dashed line is unsmoothed NCEP transport, and the thick lines are smoothed over 12 months.

interpolation created large, time-varying imbalances in the volume budget (Figure 4.5). This is an artifact of the construction of the model rather than a real feature of the circulation. To eliminate interpolation, a track approximating the mean ship track but following the edge of model grid boxes was used for estimates of volume transports. This track is shown in Figure 4.1, and the full depth volume transport across this approximate track is shown in Figure 4.5. It is clear that the full-depth volume budget is adequately balanced for calculation of heat and freshwater transport. This track is used for all calculations involving the model.

Changes in the cruise track cause further inconsistencies in the volume balance. In 1999, the endpoint of the cruise track changed from Taiwan to Hong Kong. The cruises after this change thus include transport west of Taiwan, in the Taiwan Strait. To calculate a full budget, all transport into the North Pacific must be included. In order to achieve this balance and alleviate inconsistencies between the cruises, the model was used to calculate volume, temperature, and

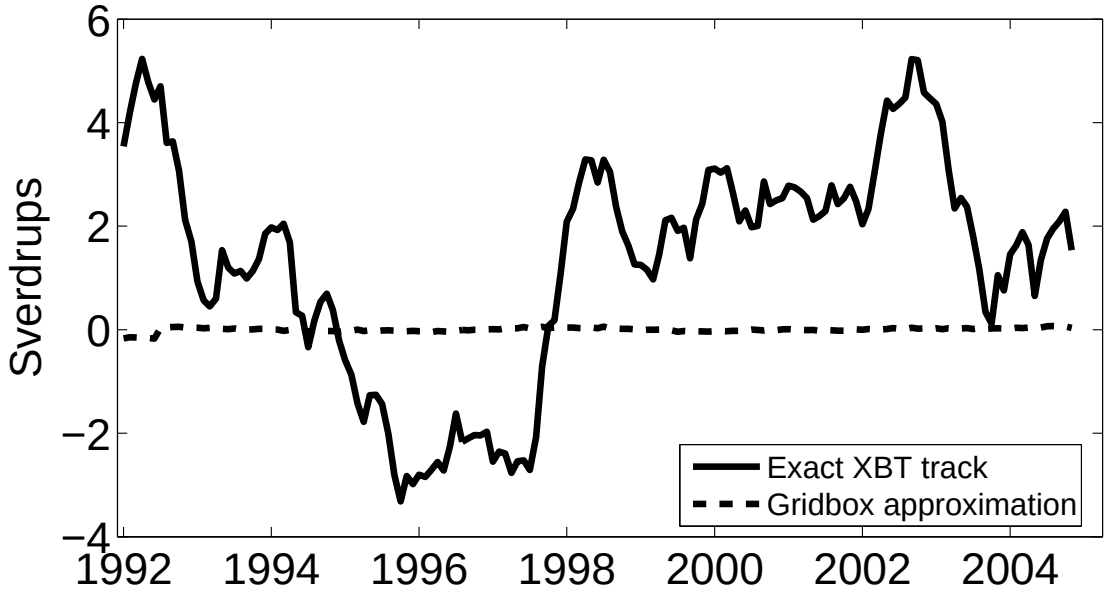

Figure 4.5: Difference between volume transport across exact XBT track from model, and volume transport across approximate track following gridbox edges to eliminate interpolation.

salt transport west of Taiwan. These results were then added to the data for cruises ending in Taiwan. The model's mean volume transport through the strait was 2.4±1.1 Sv, comparable to results from studies such as Wang et al. (2003). The variability is mainly due to a strong seasonal cycle with a maximum in the summer and a minimum in the winter. Due to the high temperatures in this region, temperature transport through the strait is significant but strongly variable, at 0.15±0.17 pW. Salt transport through the strait is an insignificant component of the freshwater budget.

A final issue that must be taken into account when comparing model and data estimates is temporal aliasing. The model produces monthly output, but cruises only occur approximately every three months. In order to estimate the effects of aliasing, when comparing a model time series with the data, the model estimate was subsampled at the times when cruises occurred. Both the subsampled model output and the data were interpolated to obtain monthly estimates, and then smoothed over 12 months to remove annual and higher frequency variability.

In most cases, this processing had only minor effects on the shape of the time series. As an example, both the subsampled and interpolated and the full time series of geostrophic transport are shown in Figure 2.4. It is evident that while both estimates preserve the main character and variability of the transport, the differences in transport can reach a Sverdrup or more. To ensure that the results are directly comparable, subsampled and interpolated time series of model estimates are used in all comparisons with XBT data.

4.4 Heat Budget

A heat budget can be calculated for the Pacific Ocean north of PX37. Figure 4.6 shows estimates from the data and the model of advective heat transport, surface heat flux, and heat storage in the region. Each component is discussed below.

4.4.1 Advective Component

Advective heat transport is the product of volume of transport and the temperature of that volume. Integrated across the full section, there is no net volume transport, but if warm water transported northward is compensated with cooler southward flow, net northward heat transport has occurred. For the model, this calculation is straightforward, using the full depth temperature and velocity fields. As shown in Figure 4.5, volume is balanced when the approximate track is used. The model advective heat transport shown in the heat budget in Figure 4.6 is the full depth heat transport from the velocity fields.

Estimating advective heat transport from the data is slightly more complicated. For this calculation, we distinguish between temperature transport, which is the product of temperature times transport but which does not require a closed region with no net volume transport, and heat transport. The heat transport across the section can be calculated as the sum of geostrophic temperature trans-

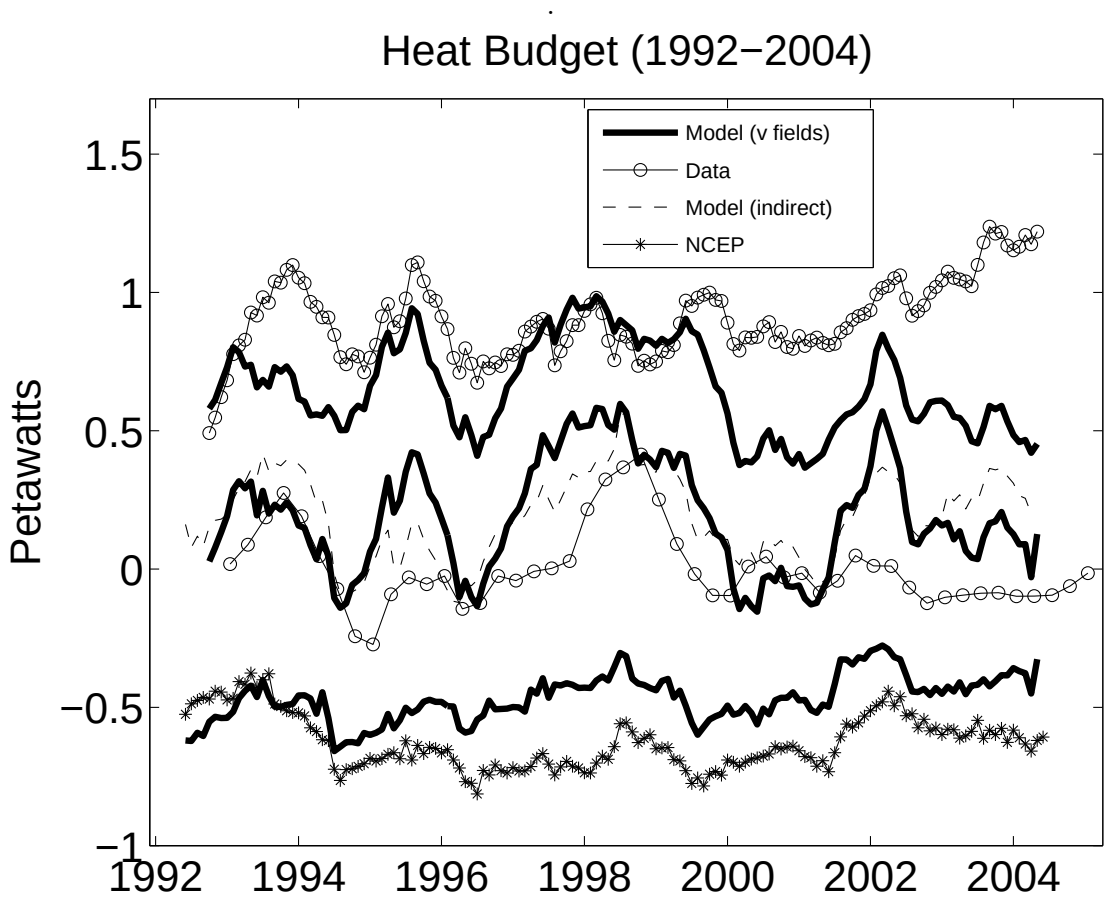

Figure 4.6: Full heat budget for the region north of PX37. Model estimates of advective heat transport (positive), surface heat flux (negative), and their sum are shown in thick black lines. Data-based estimates of advective heat transport and implied heat storage are shown as lines with circles. NCEP estimate of surface heat flux is the with stars. The implied heat storage from the change in model heat content is the thin dashed line.

port, Ekman temperature transport, and a temperature transport whose volume transport compensates for the other two components. Geostrophic temperature transport in the top 800 m is calculated from the XBT information, using the volume transport described previously. This transport, as shown in Figure 4.2, is southward. Ekman transport, as shown in Figure 4.4, is northward across the transect. For this analysis, we assume that Ekman transport occurs at the surface temperature, an assumption that has been shown to introduce negligible error into the calculation (Wijffels et al., 1994). When determining the sum of Ekman and geostrophic components of temperature transport, difficulties arise as a result of aliasing effects. If Ekman temperature transport is subsampled to the months when XBT cruises occur, and then interpolated to obtain new monthly estimates and smoothed to remove higher frequencies, discrepancies between the original and subsampled time series are significant, as demonstrated in Figure 4.7. Ekman temperature transport occur at the warmest temperatures, so small discrepancies in volume are magnified by high temperature. In this case, the differences reach magnitudes of up to 0.4 pW. This is due to aliasing of the high-frequency variability evident in Figure 4.4. To avoid this issue, the XBT estimates of temperature transports are interpolated to monthly values before the Ekman component, which is a model product and therefore available in all months, is added. This aspect of processing must also be replicated with the model estimates. Since Ekman velocity is incorporated as part of the model velocity fields, Ekman transport must be calculated and removed prior to subsampling the estimate at XBT months, and then added after interpolation. This ensures that the data and the model are being processed in the same way, which is necessary for making comparisons.

To complete the estimate of advective heat transport from the data, the volume must be balanced. The sum of Ekman transport and geostrophic transport leaves a mean imbalance of 1.42 ± 2.62 Sv. The model can be used to help determine the best method to balance the volume. In terms of temperature transport, there are two extremes for how the volume imbalance is compensated. On

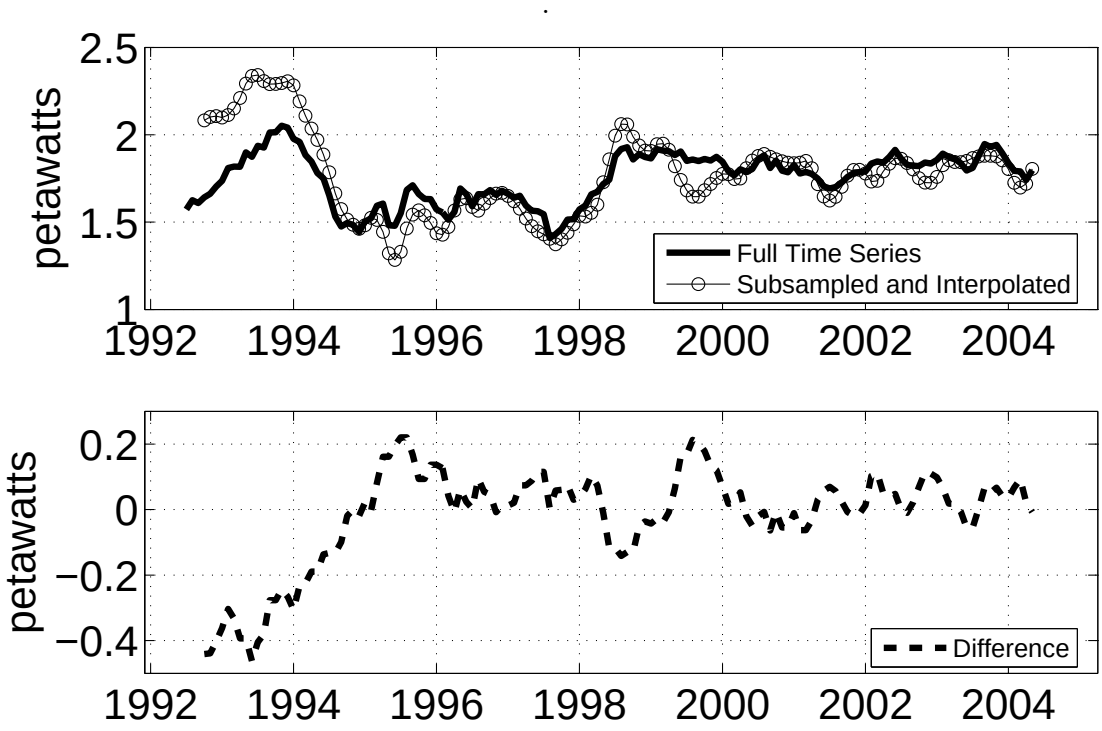

Figure 4.7: (a) Ekman temperature transport. Solid line is the full time series smoothed over 12 months, and line with circles is the time series when subsampled to dates of XBT cruises and interpolated before smoothing. (b) The difference between the two time series in panel (a).

one hand, there could be a barotropic component of transport. If this were the case, the compensating transport would occur throughout the water column, and the net temperature transport would occur at the depth-averaged temperature. The model estimate of depth-averaged temperature along PX37 is 2.9°C. Alternatively, the compensating transport could be baroclinic, resulting from shear below 800 m. In the extreme, if there were enough shear just below 800 m in the warm western boundary current, the compensating transport would be at the mean temperature of the Kuroshio. In the model, the mean temperature of the Kuroshio transport is 12.8°C; in the data, it is 13.8°C. Although these two options offer a simplistic view of the velocity structure, applying them to the model can provide some guidance as to how to balance volume in the data. To do this, we calculate the model geostrophic transport relative to zero, as in Figure 4.2. Adding Ekman transport gives us the residual volume to be balanced, and the total heat transport is determined from the model by summing the geostrophic temperature transport, the Ekman temperature transport, and the baroclinic or barotropic volume-compensating temperature transport. The difference between each of these estimates and the model's full depth heat transport is shown in Figure 4.8. It is evident that neither estimate is perfect. However, on average, the amount of temperature transport result from each is small, at -0.057±0.14 pW from the baroclinic balance and 0.055±0.16 pW from the barotropic balance. The difference is slight, but the barotropic version has a smaller average, and we therefore choose that method of balancing the volume. Thus, the data-estimated advective heat transport shown in Figure 4.6 is the sum of the geostrophic temperature transport, the Ekman transport as estimated by the ECCO model, and a barotropic volume-balancing component at the depth-integrated temperature of 2.9°C at each time step.

Heat is transported northward across PX37 into the North Pacific, as demonstrated by positive estimates of advective heat transport from both the model and the data in Figure 4.6. As with geostrophic transport, there are simi-

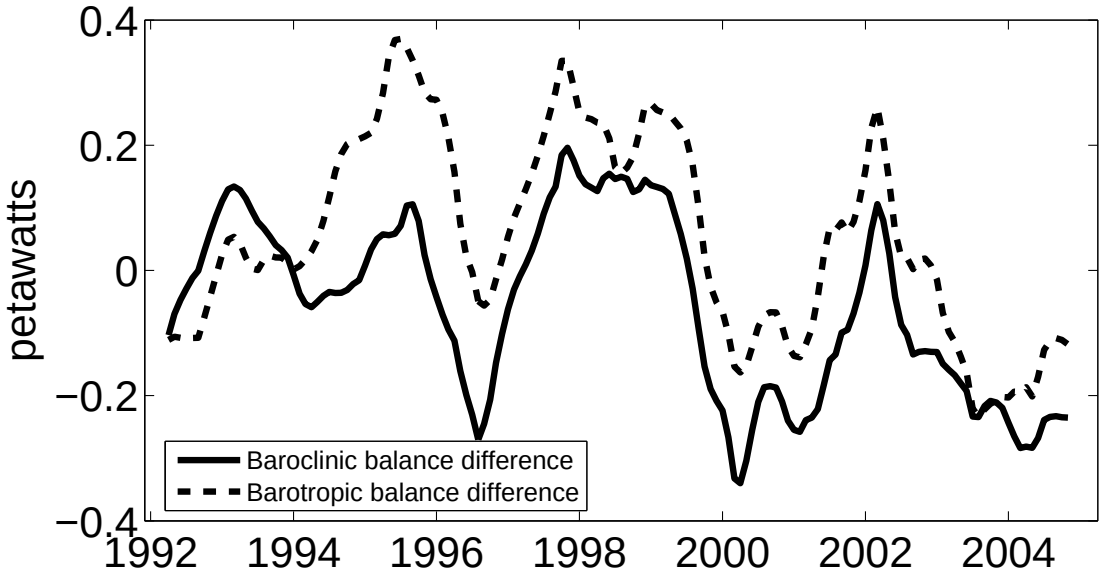

Figure 4.8: The thick solid line shows the difference between the model estimate of full depth heat transport, and the model estimate using geostrophic transport relative to zero with a baroclinic assumption for volume balance. The dashed line uses the barotropic assumption to balance the budget

larities between the model and data estimates of heat transport but they are statistically uncorrelated. Many of the discrepancies in heat transport coincide with discrepancies in geostrophic transport, such as the high bias in the from 1993-1997 and again from late 1999 to the end of the time series. As with volume transport, it is instructive to compare geographical subsections to determine the location of the discrepancies. The temperature transport, including both geostrophic and Ekman components, across each of the three sections is shown in Figure 4.9. Model and data estimates of temperature transport are highly correlated for each of the three geographical sections. Correlation coefficients are 0.72, 0.88, and 0.79 for the western, central, and eastern sections respectively. However, it is clear that northward temperature transport in the data is much higher than that in the model between Hong Kong and Guam, and that the southward temperature transport estimated from the data between Honolulu and San Francisco is larger than the model estimate as well. Noting the different scales of variability in the sections, it is clear that the high bias between Hong Kong and Guam will dominate. This

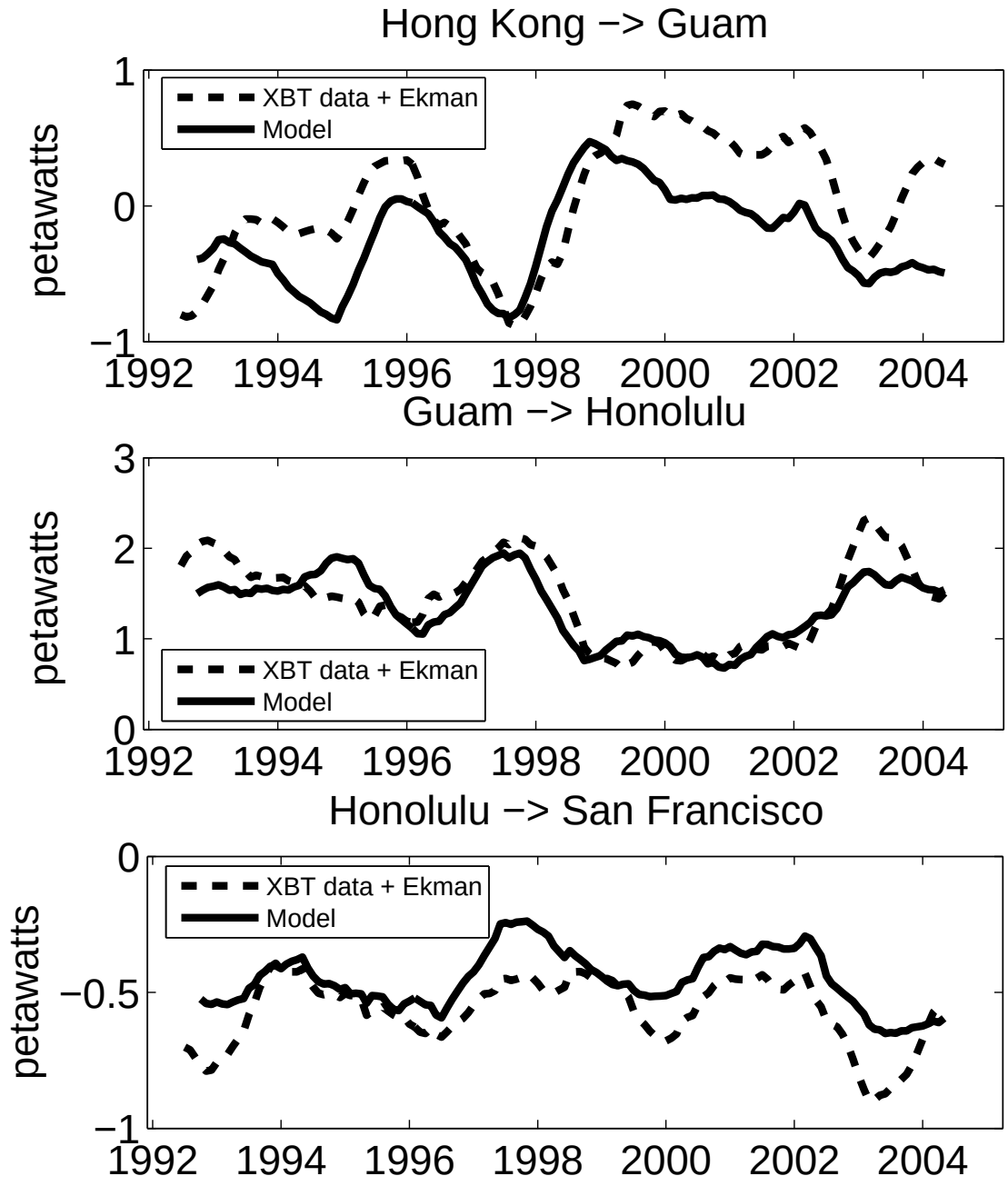

Figure 4.9: Advective temperature transport for each of the geographical sections, estimated from model velocity fields and from XBT data with model Ekman added.

bias has the same structure as the volume differences between Guam and Hong Kong. Additionally, it was noted in the previous sections that the data estimate of mean temperature in the Kuroshio is higher than the model estimate, which would contribute more to the high bias in the data. Although the temperature transport between Guam and Honolulu has the largest magnitude, it does not seem to have a particular bias, and probably does not contribute as much to the systematic differences between the data and model estimates of advective heat transport.

The differences between model and data estimates of heat transport still warrant further investigation. In particular, the data estimate of heat transport increases throughout the time series, while the model estimate decreases. There are several possible causes for this difference. One possibility is a change in the warm northward Ekman transport compensated by cooler water in the subsurface layers, which would lead to net heat transport northward. Because the same volume of Ekman transport is used for both estimates, this would be visible as an increase in observed surface temperature relative to model surface temperature. Another possibility is that differences already noted in the magnitude of geostrophic transport are magnified by differences in the temperature of the transport as well. The evolution of the temperature anomaly along the transect, shown in Figure 4.10, clarifies some of the issues at hand. For the full track and in each geographical section, temperature was averaged both spatially and temporally to determine a mean profile. At each time step, this mean profile was subtracted from a spatially averaged profile, to determine the evolution of temperature anomaly as a function of time and depth. The anomaly time series was smoothed over one year to remove the annual cycle and higher frequency variability. The most significant signals are not at the surface, implying that changes in Ekman temperature transport are not to blame for the previously noted discrepancies in heat transport. A much more significant and persistent signal is the warming in the thermocline throughout the time series. This signal is present in the model but is much stronger in the data. Around 1999, when the data estimate of advective heat transport deviates signif-

.

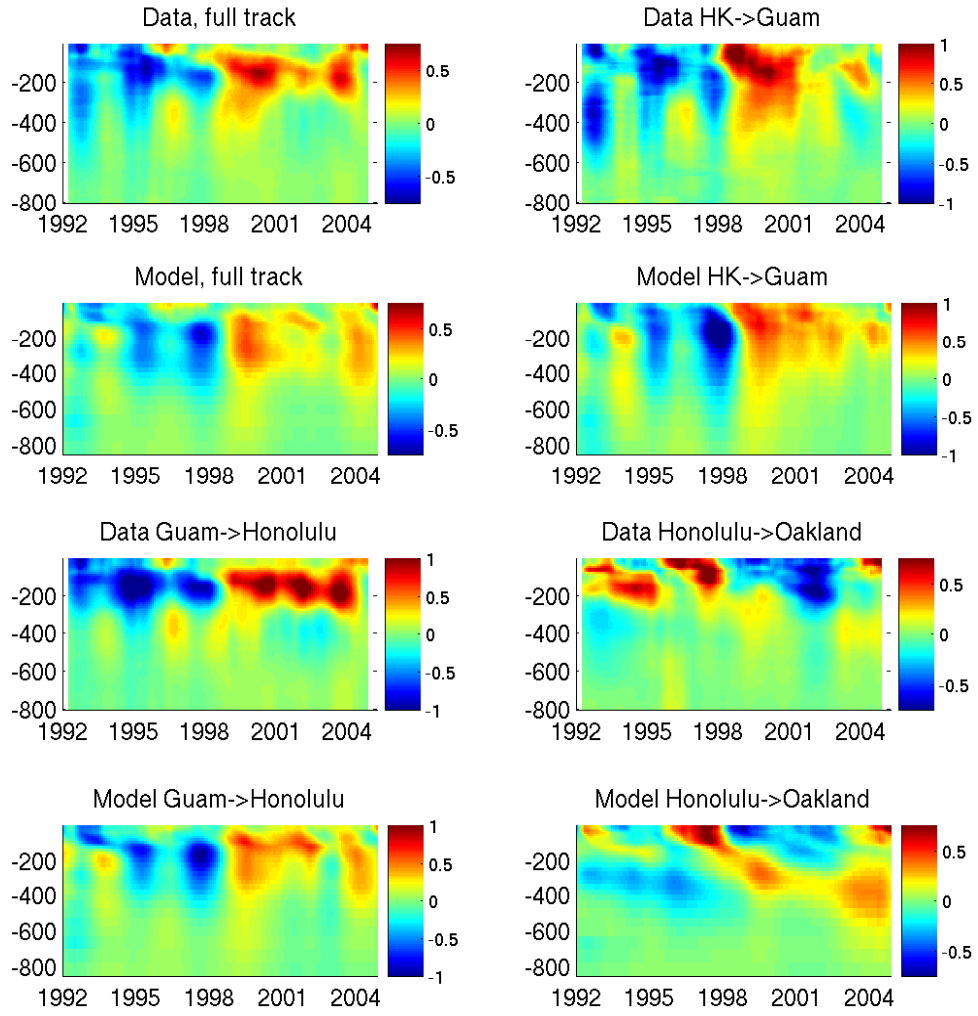

Figure 4.10: Model and data-based estimates of the time evolution of temperature anomaly as a function of depth, for the full track and for each of the geographical sections.

icantly from the model estimate, a strong warming signal is evident in the top 300 m between Hong Kong and Guam. Figure 4.9 confirms that at this time, the temperature transport between Hong Kong and Guam is significantly higher than the model estimate. Shortly after that signal, in around 2001, there is significant warming of the thermocline between about 100 m and 300 m depth in the region between Guam and Honolulu. This signal is significantly weaker in the model estimate. Figure 4.9 indicates that this discrepancy is not significant relative to the size of the temperature transport until 2003, when the model seems to cool slightly and the observed increase in thermocline temperature reaches its peak. There is also an increase in data-estimated geostrophic transport at this point (Figure 4.2), magnifying the excess of temperature transport in the data over the model. Between Honolulu and San Francisco, on the other hand, temperature transport is southward, and is stronger in the data than the model (Figure 4.9), because mean observed temperatures are warmer than those in the model. However, the magnitude of the variability in both the temperature anomaly and the volume transport is much smaller in the east than that the rest of the transect, so the effect on the total heat transport is minimal.

Another perspective on advective heat transport can be obtained by examining the temperature structure of the mean volume transport. Figure 4.11 shows the temperature classes in which transport occurs, for the model and the data. The model transports are calculated from the model velocity fields, while the transports for the data are calculated from geostrophy. Ekman transports calculated from the wind field from the model are added to geostrophic estimates. The figure also shows standard deviations. The structure of total heat transport is simple. Large volumes of the warmest water are transported north. This warm flow is compensated with a deep return flow, at a broad range of cooler temperatures. Most of the warm northward transport occurs between Guam and Honolulu, and can be attributed to northward Ekman transport. Transport throughout the water column between Guam and Honolulu is northward, which is not true of either of

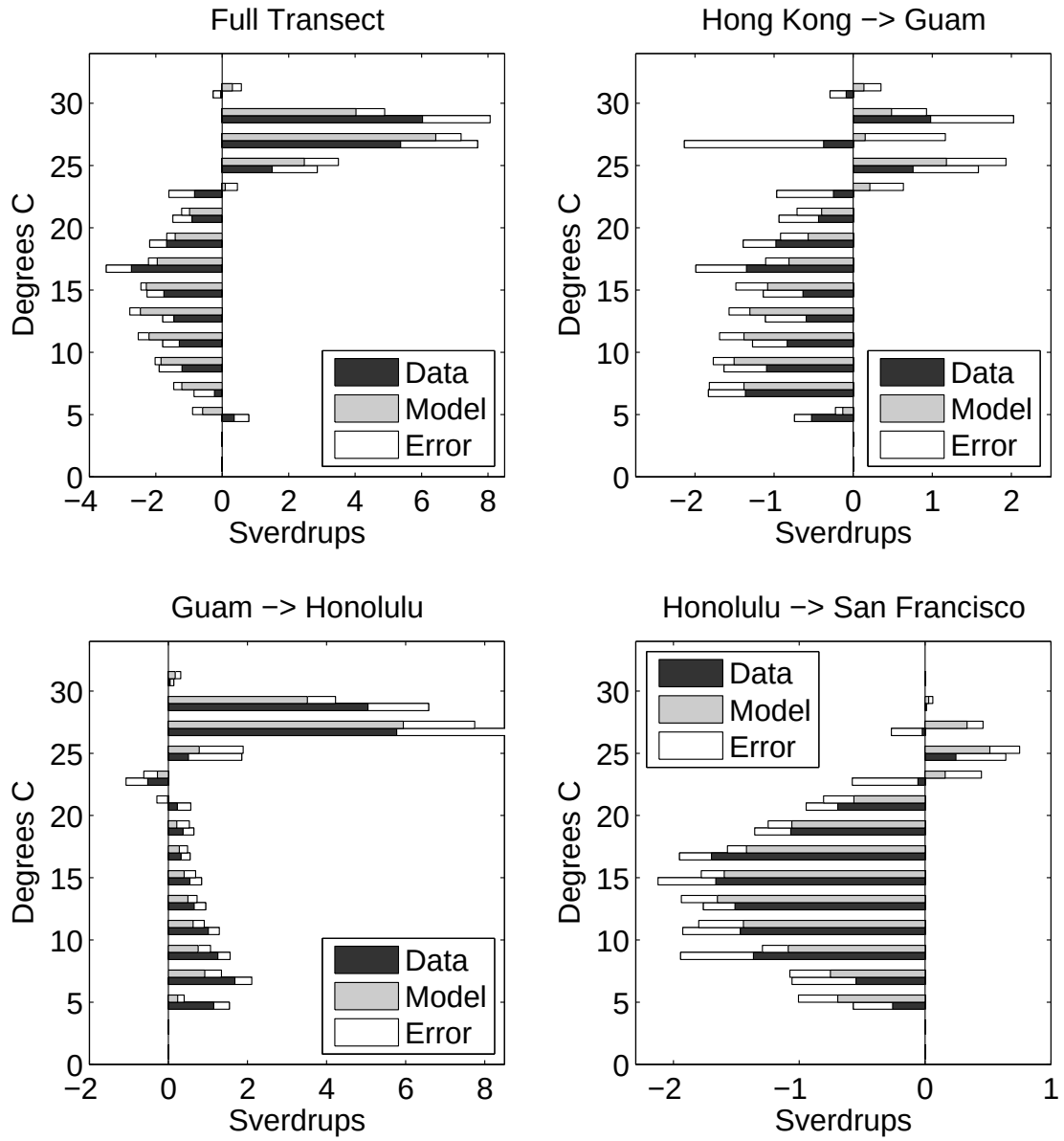

Figure 4.11: Temperature classes of volume transport, for the model and for data (geostrophic plus ekman). Shown for the full transect and for each of the geographical sections.

the other two regions. Transport in the warmest classes between Hong Kong and Guam is generally northward but highly variable. Transport in cooler temperature classes in this region is southward and somewhat more stable, but error bars are still significant relative to the magnitude of the signal. Most transport between Honolulu and San Francisco is consistently southward and cool, with error bars that are small relative to the size of the signal, indicating relative stability in this region.

4.4.2 Surface Flux

Surface heat flux is another component of the heat budget shown in Figure 4.6. Two estimates of surface flux are shown, one from NCEP and the other from the model. In both estimates surface flux is negative, indicating that net heat is radiated to the atmosphere from the ocean. The two estimates are similar, with a correlation coefficient of 0.36. In the assimilation process used by the ECCO model, surface heat flux is one of the "control variables" which is adjusted to reduce the model-data misfit. NCEP fields provide the starting point for the model, so the difference between the model and NCEP estimates of heat flux are indicative of the magnitude of the changes made by the model. In this case, the model adjustments have had only small effects on the variability of the surface flux. The mean has changed significantly: the magnitude of heat radiated from the region has decreased by 0.16 pW. Additionally, there is a trend of decreasing magnitude in the model surface heat flux during the time series that is not seen in the NCEP estimate. Spatially, the difference between the two heat fluxes is shown in Figure 4.12. Figure 4.12(a) shows the time mean NCEP heat flux. The sign convention in this figure is consistent with the rest of this work, with positive numbers indicating heat absorption by the ocean from the atmosphere. The main feature of heat flux north of PX37 is the distinct radiation of heat from the Kuroshio region. In the northeast Pacific, heat flux is weakly absorbed by the ocean. Figure 4.12(b) shows the mean adjustments made by the model to the heat flux. These include a

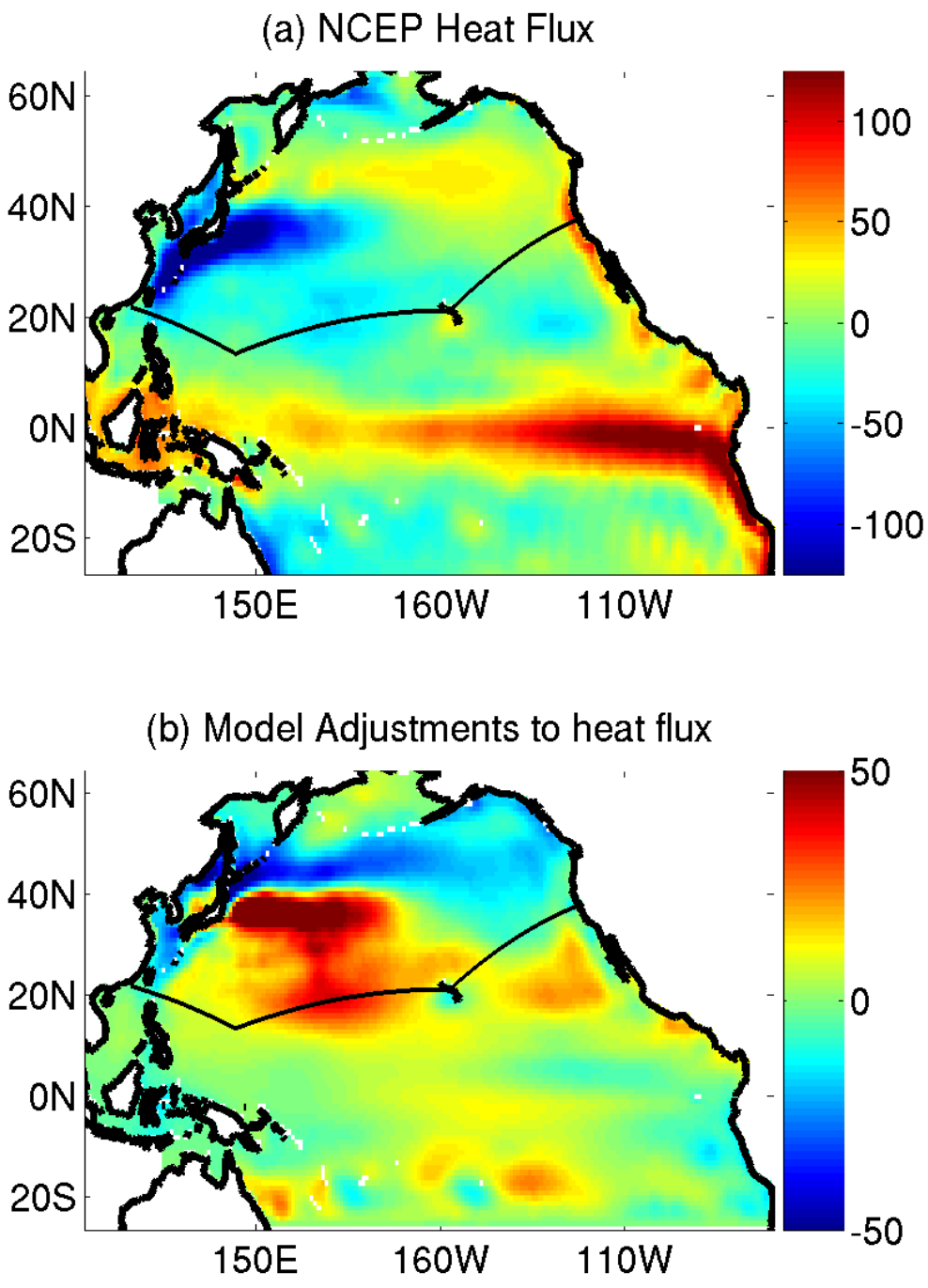

Figure 4.12: (a) Map of mean NCEP heat flux (b) Map of mean difference between model heat flux and NCEP heat flux. Units are W/m^2

significant weakening of the radiation over the Kuroshio, countered by an increase in radiation (decrease in absorption) farther north. From the heat budget, it is clear that the decrease in radiation over the Kuroshio dominates the changes.

4.4.3 Storage

The final term of the heat budget is the heat storage. There are two methods of estimating heat storage. First, as this is a budget for a closed region, the storage must be equal to the sum of the advective and surface terms in the model (method one). Second, storage can also be calculated as the time derivative of heat content (method two). Both of these methods are applied to the model and shown in Figure 4.6. That these two estimates of heat storage are well correlated (correlation coefficient of 0.81) only implies that the model is self-consistent. The differences between them arise because the storage implied from heat content is derived using the full model time series, while the advective part of the other estimate is subsampled and interpolated to match the XBT estimate. A more instructive comparison is with the third estimate of heat storage. This estimate is calculated from the time derivative of heat content anomaly estimated from a combination of broadscale XBT data and satellite altimetric height (Willis et al., 2004, hereafter WRC). There are notable differences between this estimate and the estimates from the model. In particular, the model estimates are biased high. The mean of the model estimate from method one is 0.21 ± 0.24 pW, while that of the model estimate from method two is 0.19 ± 0.15 pW. Both of these indicate a time mean increase in heat content. The WRC estimate, on the other hand, has a time mean of 0.0035 ± 0.14 pW. All three estimates have variability of the same order of magnitude. Despite the bias, the correlation between the WRC estimate and the model estimate from method one is 0.77, and that between the WRC and the model estimate from method two is 0.72. These high correlations confirm that the model's estimate of the variability of the heat storage is accurate.

Taken as a whole, the heat budget analysis demonstrates the large in-

terannual variability in heat transport in the North Pacific. Variability of surface heat flux is secondary to advective heat transport, which can vary by as much as 0.5 pW. These changes in advective heat transport result from changes in both geostrophic volume transport and thermocline temperature structure. As the sum of two variable components, heat storage is itself highly variable, with a range of almost 0.7 pW. In general, changes seem to occur on a time scale of 2-4 years.

4.5 Freshwater Budget

Calculation of a budget for freshwater is less straightforward. Because changes in salinity are small relative to changes in transport velocity, salt transport is very highly correlated with volume transport. In order to separate the salinity variability from the interannual changes in volume transport, an equivalent freshwater flux was calculated. The concept is relatively simple. Volume is being transported into and out of the region at all times. If the incoming transport has a higher salinity than the outgoing transport, the net effect is an increase in salt content in the region. If the outgoing transport contained the same amount of salt as incoming transport, but with more freshwater added, resulting in lower outgoing salinity, the effect on the salt content of the region would be the same: increased salinity, due to exported freshwater. In essence, we assume that the same amount of salt is entering and leaving the region, and import and export of freshwater is responsible for the variation of salinity.

The equivalent freshwater transport can be calculated as follows. Volume must be conserved, so incoming volume transport is equal in magnitude to outgoing volume transport, including freshwater. Incoming salt is also equal to outgoing salt . Therefore we have:

$$V_{in} = V_{out} + FW \tag{4.1}$$

$$\rho * V_{in} * S_{in} = \rho * V_{out} * S_{out} \tag{4.2}$$

In this equation, V_{in} and V_{out} are incoming and outgoing volume transport respectively, S_{in} and S_{out} are incoming and outgoing salinity respectively, and ρ is the density of seawater. We can solve for FW in terms of incoming or outgoing velocity.

$$FW = V_{in} * \frac{S_{out} - S_{in}}{S_{out}} \tag{4.3}$$

$$FW = V_{out} * \frac{S_{out} - S_{in}}{S_{in}} \tag{4.4}$$

In this way we calculate a transport that accounts for the changes in salinity, but in a way that is independent of the varying volume transport signal, because of the requirement of balanced volume transport at every time step.

As was the case with temperature, the XBT dataset only provides information in the top 800 m. Salinity is determined from a combination of historical data, XCTD casts, and profiles from Argo floats where available. As with temperature, most variability occurs in the top 800 m. A comparison between the model estimates of full depth equivalent freshwater transport and the equivalent freshwater transport in the top 800 meters is shown in Figure 4.13. Differences are much smaller than the magnitude of the signal. Because the calculation of equivalent freshwater transport requires balanced volume transport, and we have demonstrated that using the top 800 m give the same magnitude of variability that using full depth does, the calculation for the data estimate of equivalent freshwater transport will be performed using only the top 800 m, instead of estimating baroclinic and barotropic closure schemes as was necessary for an accurate measurement of heat transport and its variability.

The components of the freshwater budget are shown in figure 4.14. Panel (a) shows the total freshwater storage in the North Pacific. This is calculated in three ways: from XBT advective freshwater transport plus NCEP surface flux, from the model advective freshwater transport plus model surface flux, and from the time derivative of model salt content. There is not enough salinity data to

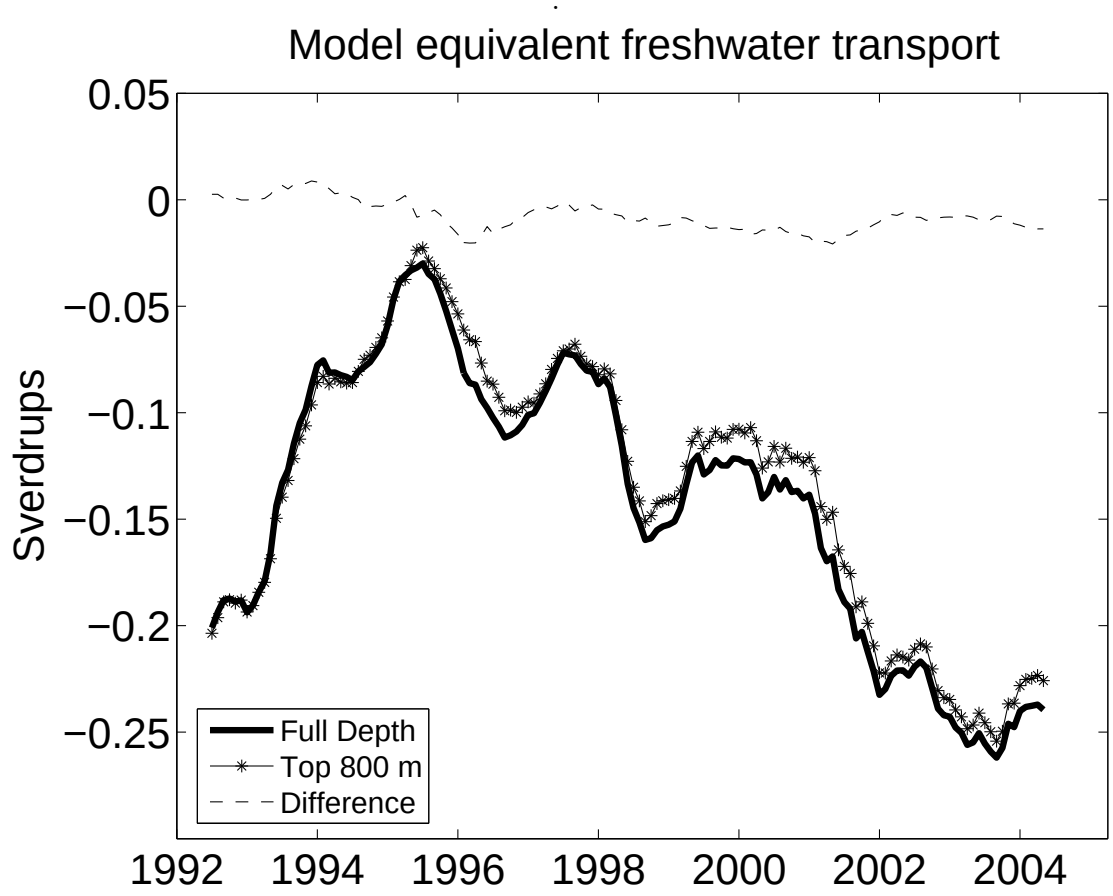

Figure 4.13: The thick solid line shows the full depth equivalent freshwater transport, while the thin solid line shows the top 800 m equivalent freshwater transport. The dashed line shows the difference.

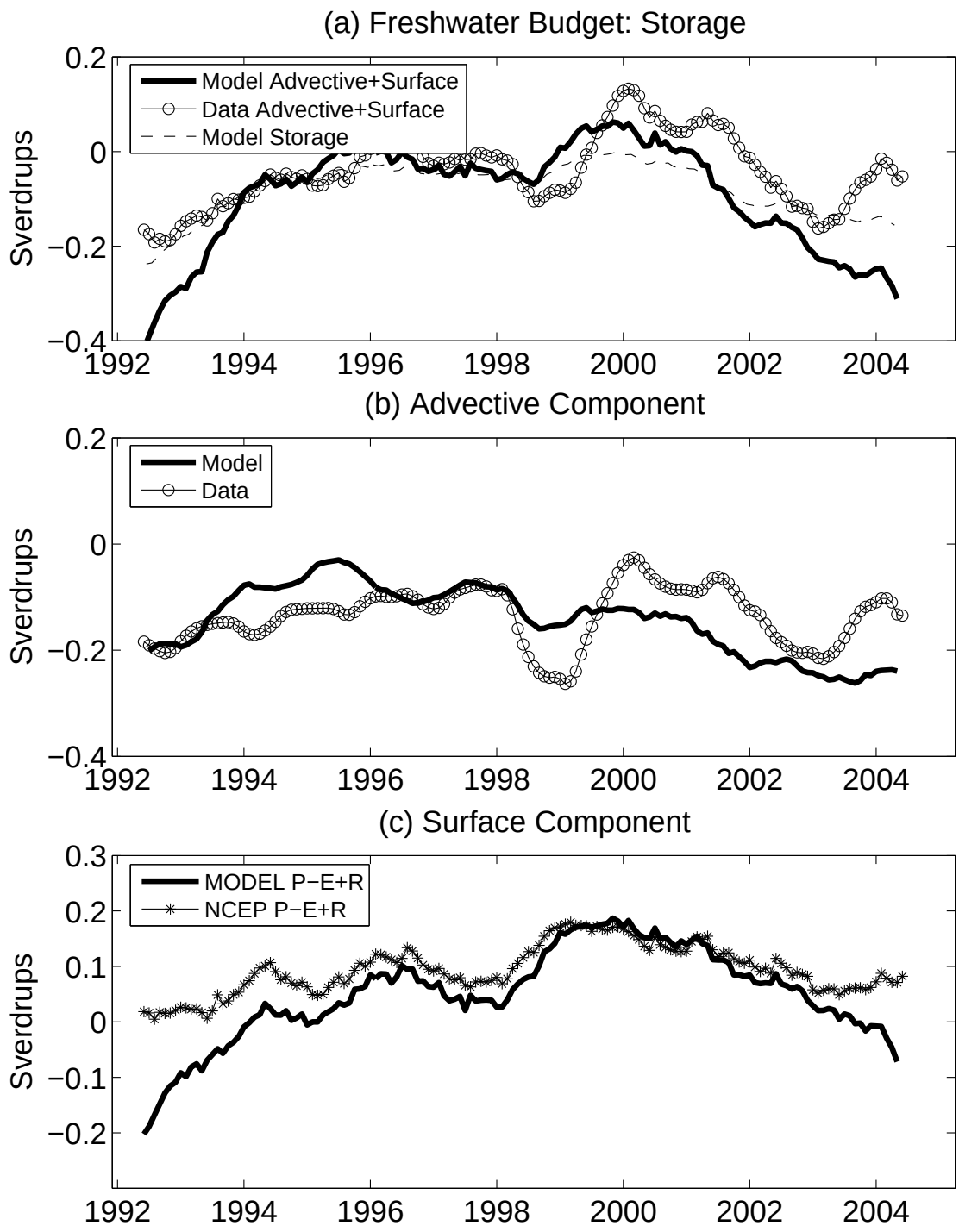

Figure 4.14: Freshwater Budget for the region north of PX37. (a) Storage components of the freshwater budget. Thick line is model advective plus surface, thin line is data advective plus surface, and dashed line is derived from the time derivative of model salt content north of PX37 (b) Advective components of freshwater transport. Thick line is from the model, thin line is from the data. (c) Surface components of freshwater flux.

calculate an independent salt content. The freshwater storage implied from model salt content has a correlation of 0.98 with the sum of model advective freshwater transport and model surface freshwater flux. This high correlation implies the self-consistency of the model. However, the magnitude of variability is smaller in the storage implied from salt content. The two time series derived from advective transport plus surface flux (model and data) are also well correlated with each other (correlation coefficient = 0.72). The mean of model advective freshwater transport plus surface flux is -0.092±0.11 Sv, while the mean of XBT-estimated advective freshwater transport plus NCEP surface flux is -0.041±0.075 Sv. Both of these imply a net freshwater export, which would mean increasing salt content in the region, but they also both have variability larger than the mean, indicating that they are statistically equivalent to zero. This indicates that while there is variability, the salt content in the North Pacific is, on average, conserved.

The advective component of the budget is shown in Figure 4.14(b). The estimates of equivalent freshwater transport from the data and the model have a correlation of 0.32. The data has signals of larger magnitude, such as an abrupt decrease in freshwater export in 1999 of almost 0.2 Sv. The main characteristic of the model estimate is a consistent increase in freshwater export from 1995 to the end of the time series. Both time series are negative throughout the time period, indicating that freshwater is exported through advection from this region.

Another aspect of the freshwater budget is revealed by examining the evolution of the salinity profiles in time. Using the same method applied previously to temperature, along-track salinity was averaged spatially and temporally to obtain a mean profile. At each time step, this mean profile was subtracted from a spatially averaged profile, to obtain a time series that shows the evolution of salinity anomaly as a function of depth and time. This was performed for the full track, and also for each of the previously defined geographical regions, to provide insight into the spatial variability of salinity. Results from model and data are shown in Figure 4.15. Unlike temperature, most of the salinity signals are stronger in the

.

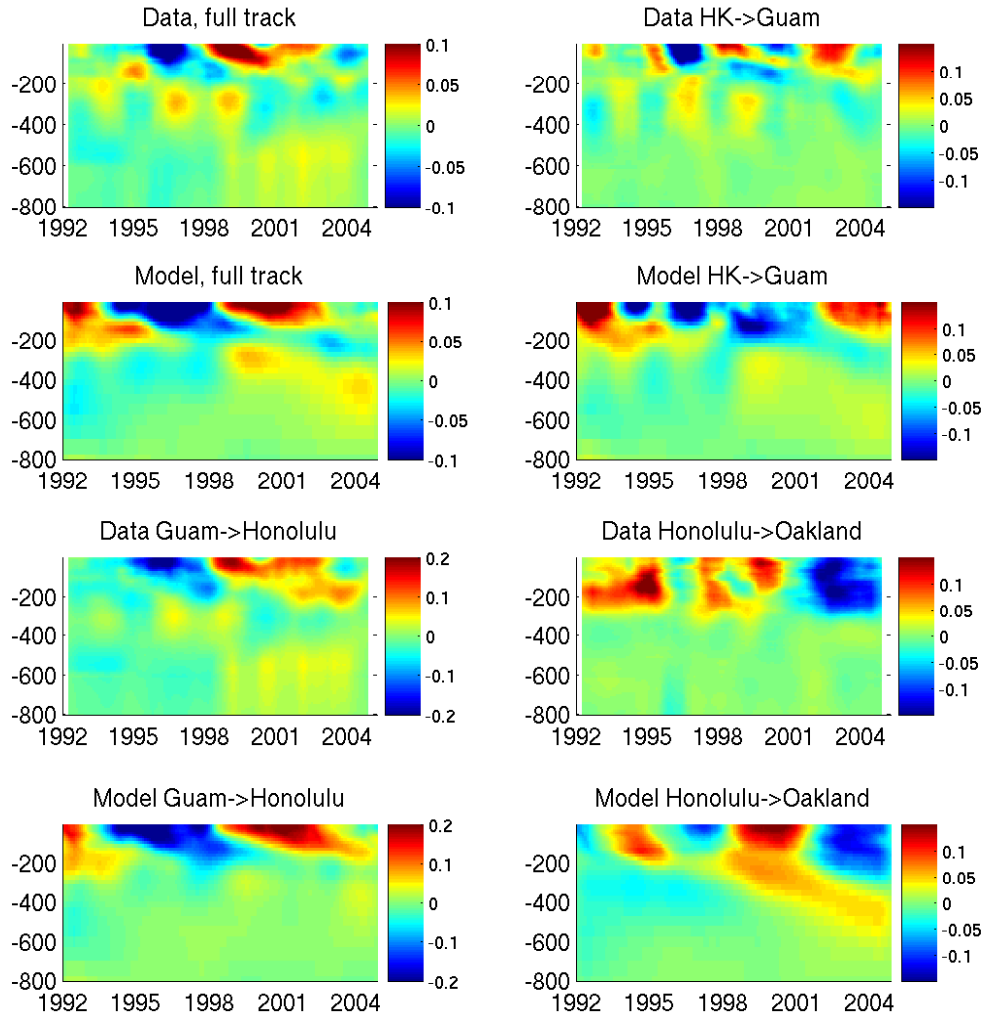

Figure 4.15: Model and data-based estimates of the time evolution of salinity anomaly as a function of depth, for the full track and for each of the geographical sections.

model than in the data. The largest signals occur between Guam and Honolulu, where there is an increase of salinity throughout the time series. This trend is the main signal when the full track is considered, as well. The increase in salinity is stronger and longer lasting in the model than in the data. Another interesting feature of salinity signals, evident in both the model and the data, is the tendency for a signal to originate at the surface and have its strongest signature there, and then to propagate to depths of 200 m or more. Particularly between Guam and Honolulu, a strong trend of increasing salinity is seen to start at the surface and then propagate down to 200 m depth. This could indicate that these signals are strongly influenced or caused by surface fluxes.

The surface component of freshwater transport is shown in Figure 4.14(c). The components of surface flux of freshwater include precipitation and runoff (both positive into the ocean) and evaporation (positive out of the ocean). The NCEP freshwater flux is positive throughout the time series, with a mean of 0.094±0.044 Sv of freshwater into the ocean. In this case the model's adjustments have been large enough to change the sign of the freshwater flux. The model mean freshwater flux of 0.050±0.083 is positive, but the variability is strong enough that it is statistically equivalent to zero. The spatial patterns of both the NCEP precipitation minus evaporation (P-E) and the adjustments to it are shown in Figure 4.16. These maps only show P-E; the runoff component is excluded. The map of freshwater flux shows the band of positive freshwater flux into the ocean from precipitation at a latitude of about 45°N from the North Pacific storm track, and a band of evaporation just south of that. In the region of interest, the adjustments from the model are opposite the signals in the original field, indicating a reduction of precipitation over the storm track and a reduction of evaporation at the latitude of PX37. In Chapter 3, it was evident that the freshwater fluxes from this model were much less structured than those from the more highly converged ECCO-GODAE model, and it bears repeating that the model used in this analysis is not fully converged. Since freshwater is a quantity that is less well-observed with

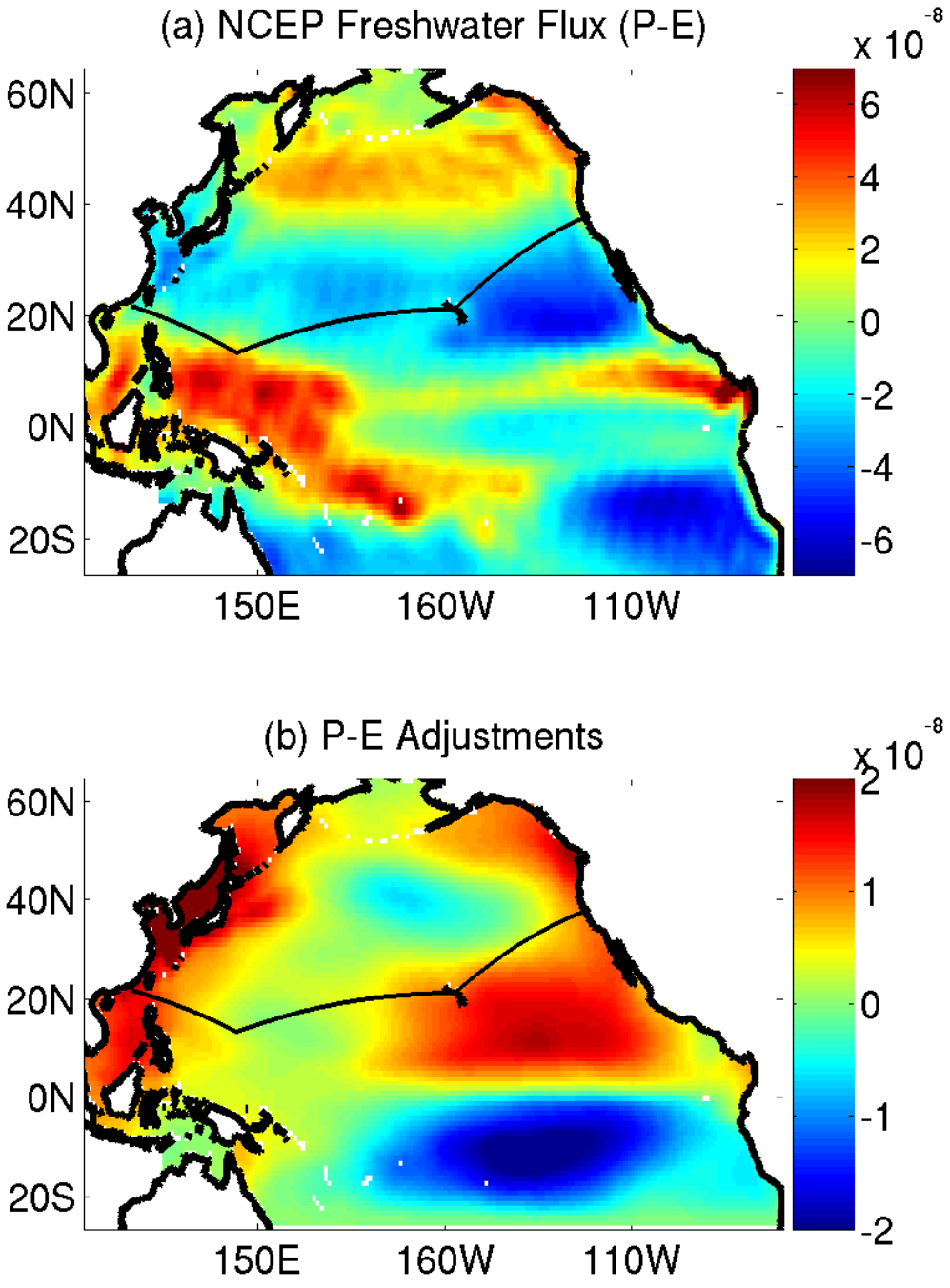

Figure 4.16: (a) Map of mean NCEP P-E (b) Map of mean adjustments to P-E made by the model.

higher error bars on both the measurements and the forcing fields, it is reasonable to think that more adjustments are necessary to bring this component of the model to full convergence. Thus far, though, it does provide a well-balanced component of the budget in Figure 4.14(a).

Overall, the freshwater budget seems to have less variability than the heat budget. The magnitudes of variability in advective transport and surface flux are the same as each other and as the magnitude of variability of freshwater storage. Additionally, the changes that do occur take place on longer time scales than in the heat budget, closer to 5 years rather than 2-4. In general, the freshwater budget seems to be much more stable than the heat budget.

4.6 Forcing

The North Pacific evidently has a relatively stable freshwater budget but a highly variable heat budget. Figure 4.6 shows significant variability in storage on a time scale of 2-4 years. As stated previously, this variability in heat storage is mainly a result of changes in advective heat transport, which are caused by changes both in the volume of transport and the temperature structure of the water being transported. Determining how these changes fit into the structure of the gyre-scale circulation could help explain the forcing behind them. To investigate the changes in volume transport, correlations between the geographical sections are considered. The volume transport between Hong Kong and Guam is highly anticorrelated with that between Guam and Honolulu. In a physical sense, this reflects the magnitude of westward transport of both the southern limb of the subtropical gyre and the North Equatorial Current (NEC) north of Guam. Because of the geography of the track, this westward transport manifests itself as northward (into the region) transport into the region between Honolulu and Guam, and corresponding southward (out of the region) transport between Guam and Hong Kong. When the total NEC transport increases, so do each of these components. As the NEC reaches the

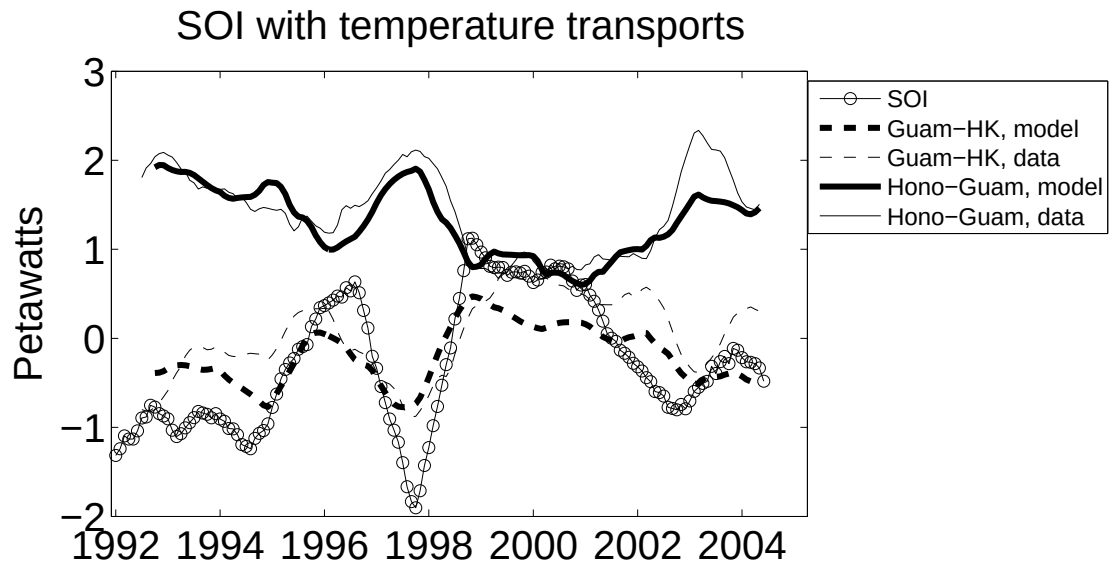

Figure 4.17: 800 m temperature transport from model and data with the SOI

western edge of the basin, it bifurcates, with transport going north in the Kuroshio or south back into the equatorial circulation system. When the NEC transport is at its largest (during El Niño events), it bifurcates at a higher latitude. This leads to a smaller transport volume in the Kuroshio (Kim et al., 2004), and a lower net northward transport west of Guam.

Volume transport is correlated with temperature transport in this case. In the high El Niño phase, the increased northward transport between Honolulu and Guam consists of warmer water. This warming is evident in the temperature profile anomalies in Figure 4.10. In the Kuroshio, the higher bifurcation latitude and corresponding smaller transport leads to less northward temperature transport. At the same time, there is more southward transport west of Guam as a result of the NEC meander. These combine to create a minimum in northward temperature transport west of Guam during high El Niño phases. East of Guam, however, the stronger, warmer NEC leads to northward temperature transport, not all of which returns back to the south at the western edge of the basin. These results are confirmed in Figure 4.17. Correlations are both visually apparent and statistically significant. For the model, correlation between the temperature transport between

Hong Kong and Guam and the Southern Oscillation Index (an index associated with El Niño) is 0.86. Temperature transport between Guam and Honolulu is strongly anticorrelated with the SOI at −0.86. In the data, correlations with the SOI are 0.76 for temperature transport between Hong Kong and Guam and −0.77 for temperature transport between Guam and Honolulu, in agreement with the model's results.

With these varying effects vying for dominance in the net advective heat budget, there is no clear correlation between the SOI and the total net heat transport. Rather, the net heat transport is a result of the extent to which these two opposite-sign results – increased northward temperature transport between Honolulu and Guam, and increased southward temperature transport between Guam and Hong Kong – cancel each other out.

The case of freshwater transport is slightly different. Because volume is not balanced in individual segments, the "equivalent freshwater transport" cannot be calculated separately for the legs of the cruise track. However, as shown in Figure 4.18(a), mean transport can be broken down into salt classes. Overall, there is southward transport in the saltiest and freshest classes, with northward transport in the mid-range salinity classes. There is a lot of variability in the high-salinity classes, as well as large discrepancies between model and data estimates. In particular, the data indicate strong northward transport at around 34.5 psu, while model components have considerably smaller magnitude. Transport with salinity below 34.0 psu, on the other hand, is consistently southward with low variability and good agreement between model and data.

Considering the geographical breakdown of these salinity classes provides further enlightenment. In this case, only two segments are used: the region west of Honolulu to Hong Kong, including the gyre-scale circulation and the Kuroshio (Figure 4.18(b)), is compared to the region between Honolulu and San Francisco, which includes the low-salinity California Current (Figure 4.18(c)). The freshest transport, directed southward, is solely from the section of the cruise track be-

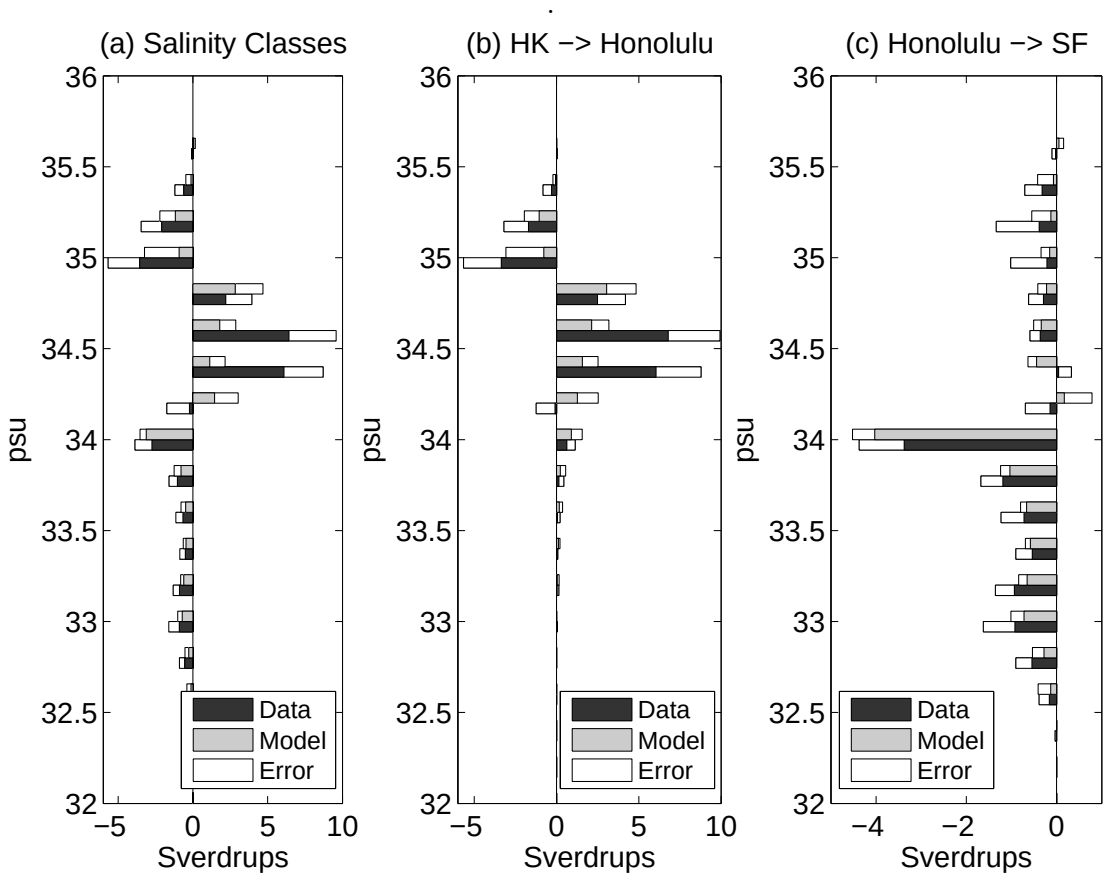

Figure 4.18: Geographical breakdown of salinity classes. Panel (a) shows transport between Hong Kong and Honolulu, panel (b) shows transport between Honolulu and San Francisco. Data transport, in dark gray, is geostrophic + Ekman. Surface temperatures and salinities are used for Ekman. Model transport, in light gray is from the full model velocity field. White indicates error bars: one standard deviation. Positive values indicate transport northward into the closed region. Classes are 0.2 psu.

tween San Francisco and Honolulu. This signal is strong and persistent, with low variability, in both the data and the model. Higher salinity transport occurs in both sections. Between Honolulu and San Francisco, most transport is southward but standard deviations are high and magnitudes are low. West of Honolulu, the data show a tendency toward southward transport in the highest salinity water and northward in slightly fresher water. All salinities are higher than the California Current, and all variabilities are high. The model estimate shows the same signals, but with lower magnitudes and higher variability. In general, except the fresh water attributed to the California Current, salt transport is characterized by high variability rather than persistent signals or well-defined structure.

4.7 Conclusions

This analysis uses 13 years of *in situ* data and output from a data-assimilating model to quantify the mean and variability of heat and freshwater transport in the North Pacific. By combining the advective transport and surface fluxes into a closed region, budgets have been calculated which demonstrate the nature and magnitude of interannual variability of temperature and salinity.

The heat budget was estimated using both a regional ocean model and data from a long time series of XBTs. The model was used to help determine the validity of assumptions about a reference velocity of zero at 800 m depth, and to determine that a barotropic transport was a reasonable method for closing the volume budget. Almost all variability takes place in the top 800 m, and the mean northward heat transport is 0.65±0.17 pW in the model and 0.90±0.14 pW in the XBT data. These are within each other's error bounds and within the range of previous estimates of northward heat transport in the North Pacific. The surface component of heat flux has also been quantified, and it is evident in the heat budget (Figure 4.6) that the variability in the advective component dominates the total storage variability. Variability in the surface component has much smaller

magnitude. The variability of the advective component, in turn, is dominated by the effects of the El Niño/Southern Oscillation (ENSO) climate phenomenon. The effect is indirect; total changes in heat transport are a result of the extent to which the gyre transport between Honolulu and Guam is cancelled out by the Kuroshio west of Guam. Each of these two components is highly correlated with ENSO.

A budget for freshwater was calculated as well. Results indicate that the salt balance in the North Pacific is stable. Variability in freshwater storage is a result of both changes in advective transport and surface flux; these components are comparable in mean and variability to each other and to the total freshwater storage. A geographical breakdown of mean salt transport indicates that the export of freshwater in the California Current is the strongest, most persistent component of the freshwater budget, and that other components have low mean magnitudes and high variability in both model estimates and data.

The agreement of the model and the data is an encouraging sign that by using the two in conjunction with each other, understanding is enhanced. Further work needs to be done to verify the freshwater budget and validate the salt content in the North Pacific, but the present work expands on previous estimates of the mean to provide estimates of variability and closed budgets including all components of transport.

Chapter 4 is in preparation for publication as Douglass, E., D. Roemmich, and D. Stammer, Interannual variability in North Pacific heat and freshwater budgets. The dissertation author was the primary investigator and author of this paper.

5

Conclusions

The large-scale circulation of the ocean is a key component in the global environment. On time scales from seasons to centuries, changes in the ocean reflect and feed back into larger scale climate changes. Seasonally, the ocean transports nutrients and heat necessary for biological productivity. These in turn influence the success of fishing industries. The Pacific Decadal Oscillation, a basin-scale signal related to both atmospheric and oceanic circulation, was first recognized as an oscillation between good salmon production years in Alaska and in the Pacific Northwest (Mantua et al., 1997). On interannual time scales, the El Niño/Southern Oscillation variability was also first recognized as an anomaly by fishermen in Peru. It is now a much-studied climate phenomenon, relating to anomalous conditions in the equatorial Pacific Ocean and having global effects. In general, interannual variability in the circulation of the Pacific Ocean has large magnitude and far-reaching effects. In addition to this, with its large heat capacity and resulting thermal inertia, the ocean responds on interdecadal time scales to the integrated effect of small changes in climate. Because of this inertia, warming of the global ocean is indicative of large-scale, long-term change. In order to understand and identify long-term changes in the ocean, variability on interannual time scales must be characterized as well.

The objective of this work is to bring together high-resolution datasets

and a coarser-resolution data-assimilating model in order to provide an improved description of the mean and time-varying circulation of the North Pacific Ocean. The data provide synoptic structural information, but are lacking in time resolution and spatial context; the model provides a smoother picture of the large-scale environment, as well as the dynamically consistent forcing fields associated with that environment. Together, they can characterize variability on many time scales.

The initial endeavor, as described in Chapter 2, focused on the time-varying circulation of the Northeast Pacific. Two high-resolution XBT lines together with the coastline of North America form an enclosed region. A global model provides context in which to analyze the circulation in this region, which encompasses the eastern portions of both the subtropical and subpolar gyres of the North Pacific. The data and model both span an 11-year period from 1992-2002, allowing for analysis of interannual variability in the strength of the currents in the region.

The difficulties encountered in this analysis are symptomatic of comparisons between model output and data. The model provides estimates of monthly means of temperature, salinity, and velocity, while the data provide semi-synoptic measurements of temperature approximately every three months. Observations have high spatial resolution along the ship track, while models offer full coverage of the region. The energetic mesoscale activity in the North Pacific aliases the *in situ* measurements, while the 1° resolution of the model does not resolve mesoscale variability, and is inadequate to truly capture sharp jet-like structures such as the Alaska Current. The nominal depth of the XBT dataset is 800 m, while the model has information to full depth. The lack of adequate salinity sampling contributes another source of error to the data. All of these issues make comparisons difficult.

Despite these problems, comparisons between model and data estimates of circulation showed similarities in magnitude and time scale of interannual variability. Correlations between the circulation in the subtropical and subpolar gyre were found, indicating that the currents had some anti-correlation rooted in the

bifurcation of the North Pacific Current, but that a stronger influence was the increase in the North Pacific Current itself and the resulting increase in the magnitude of circulation in both gyres. This was found to be a response to basin-scale wind forcing. The ability to both find similarities and determine sources of the disparities between the data and the model output is the strength of the synthesis of the two in one analysis.

The next step was to improve the state estimate itself. Several experiments were performed with the model to analyze possible areas of improvement. First, the model domain was restricted to the Pacific Ocean north of 26°S. This is advantageous in that it is less computationally demanding, and it focuses the assimilation on the area of interest. Additionally, the vertical resolution was increased from 23 vertical levels to 50. Under these new conditions, four experiments were performed. One experiment used all available data, while two others excluded subsets of the available data in order to evaluate the relative contributions of each dataset. From comparisons of these three, it was found that exclusion of either surface or subsurface data leads to a significant degradation of the final state estimate. For the best possible estimate, all available data must be included.

The final model experiment addressed the issue of the weights used for the subsurface data. Since there are fewer subsurface data than the surface data, under the standard weighting scheme, they have less influence on the final state estimate. Because these are point measurements in regions with energetic mesoscale activity, the error bars must account for representation error as well as measurement error and therefore must be relatively large. Thus, the weights on these data are low, further reducing their influence in the state estimation process. The experiment sought to determine whether increasing the weights on the subsurface data would introduce unrealistic results or have other detrimental effects on the solution provided by the model. After 30 iterations, this experiment outperforms all three other model experiments performed in the North Pacific region. It has lower model-data misfits and the largest percent decrease in total cost, but the

adjustments to the forcing are well within their error bounds. This model estimate also compares well with a global model with 177 iterations provided by the ECCO Consortium. The new estimate has a lower model-data misfit when compared to almost all the assimilated datasets, with the exception of SSH. The forcing fields look similar to those from the ECCO-GODAE solution, and the differences could result from the aforementioned differences in the model setting (resolution, extent, weighting), or could simply indicate a lack of convergence. Regardless, the results so far indicate that increasing the weights on the subsurface data had benefits that outweighed any disadvantages, and should be investigated further.

There are several opportunities for further advancement in the development of the model. Analysis of the error fields and associated weighting schemes offers ample opportunity for improvement. A first step would be error fields for subsurface data which varied by location. The error scheme for subsurface temperature and salinity varied only with depth in this analysis. Intuitively, it seems like areas such as the Kuroshio with higher mesoscale variability should have different error profiles and radii of influence than other areas. A more advanced approach would be to include full error covariances rather than the diagonal weighting matrices currently in use. This problem is computationally demanding and difficult, but full error covariances would allow each data point to influence those around it, rather than only the specific gridpoint in which it is located. This would allow the model to use these data more effectively.

A different approach to the same issue is to investigate the enhancement of weight according to data type, as we did. In our experiment, weights were 16 times the "standard" weights used by Köhl et al. (2007) in their assimilation. While it was clear that this improved the model results, this does not mean we have found the ideal weights for assimilation of subsurface data. Further experimentation is necessary to determine the most appropriate weighting scheme to maximize the influence of the subsurface data without projecting eddy noise onto the solution, and without introducing large errors into the surface fields such as SSH and SST.

The final section of this dissertation dealt with the calculation of heat and freshwater budgets for the North Pacific. This was an extension of both the previous chapters. As in Chapter 2, the focus was on interannual variability in circulation, but in this case the domain was expanded to the full North Pacific and the analysis included heat and freshwater transport as well. The state estimate used was the one developed in Chapter 3. From this combination, we attempted to characterize the interannual variability in heat and freshwater transport and storage as quantitatively as possible.

The analysis was complex, and relied on the model for resolution of issues such as determining a reference velocity for the calculation of geostrophic transport and balancing the volume transport, as is necessary for the development of an accurate budget. We were able to use the model to understand and reconcile many of the differences between the model and data estimates of transport, and to determine an appropriate balance of advective transport and surface flux that lead to time-varying estimates of heat and freshwater storage in the region. Magnitudes of variability in the heat budget are large. Advective transport varies by around 0.5 pW. Surface fluxes are more stable with smaller variability, implying that the changes in advective transport are the source of heat storage variability. Surface fluxes and advective transports varied simultaneously, such that the heat storage, the two components, had even larger variability than either component, with a range of about 0.7 pW.

Calculation of the freshwater budget presented a different set of issues. The first step was determining how to find freshwater transport from changes in the advection of salt. This is a less straightforward problem than heat transport. The calculation of an equivalent freshwater transport from changes in salinity of transport provides a mechanism for this analysis. Analysis of surface freshwater flux is straightforward, and the sum of these components leads to a storage component implied by the time rate of change of salt content in the region of interest. The freshwater budget seems to have a longer time scale of variability than the

heat budget does, varying on time scales of more than 5 years, while heat storage variability was 2-4 years. In the case of freshwater, advection and surface fluxes have approximately equal contributions to this variability.

Combining the model with the data allows further analysis of the observations, by providing a context in which to interpret them. The changes in heat transport are a physical result of the meander of currents during El Niño cycles, while longer-term changes in freshwater budgets are associated with different dynamics. The California Current, which provides the freshest component of transport, is relatively stable on interannual time scales, but the higher salinity transport is highly variable. Placing this variability in context helps to characterize it so as to distinguish it from long-term trends. Both specifically in this project and in general, the combination of data and model is helps make this analysis more complete. The model provides a more comprehensive picture of the ocean state we are analyzing, while the high spatial resolution of the data allow a better characterization of the synoptic state of the ocean. The result is a better understanding of the interannual variability in circulation and property transport in the North Pacific Ocean.

Bibliography

Bingham, F., 1998: Evidence for the Existence of a North Hawaiian Ridge Current. *J. Phys. Oceanogr.*, **28**, 991–998.

Bograd, S. J., and Lynn, R. J., 2003: Long-term Variability in the Southern California Current System. *Deep-Sea Res. II*, **50**, 2355–2370.

Bryden, H. L., Roemmich, D., and Church, J., 1991: Ocean heat transport across 24^{o}N in the Pacific. *Deep-Sea Res*, **38**(3), 297–324.

Chelton, D., Bernal, P., and McGowan, J., 1982: Large-scale Interannual Physical and Biological Interaction in the California Current. *J. Mar. Res.*, **40**(4), 1095–1125.

Chelton, D., and Davis, R., 1982: Monthly Mean Sea-level Variability Along the West Coast of North America. *J. Phys. Oceanogr.*, **12**, 757–783.

Dommenget, D., and Stammer, D., 2004: Assessing ENSO simulations and predictions using adjoint ocean state estimation. *J. Clim*, **17**(22), 4301–4315.

Ducet, N., Le Traon, P.-Y., and Reverdin, G., 2000: Global high resolution mapping of ocean circulation from TOPEX/Poseidon and ERS-1 and -2. *J. Geophys.Res.*, **105**, 19477–19498.

Freeland, H., 2002: The Heat Flux across Line-P, 1996-1999. *Atmos.-Ocean*, **40**(1), 81–89.

Ganachaud, A., and Wunsch, C., 2003: Large-Scale Ocean Heat and Freshwater Transports during the World Ocean Circulation Experiment. *J. Climate*, **16**, 696–705.

Gilson, J., Roemmich, D., Cornuelle, B., and Fu, L.-L., 1998: Relationship of TOPEX/Poseidon Altimetric Height to Steric Height and Circulation of the North Pacific. *J. Geophys.Res.*, **103**, 27947–27965.

Gouretski, V., and Koltermann, K. P., 2007: How much is the ocean really warming? *Geophys. Res. Lett.*, **34**, L01610. doi:10.1029/2006GL027834.

Hickey, B. M., 1998: *Coastal Oceanography of Western North America from the Tip of Baja California to Vancouver Island*, chapter 12, 345–393. John Wiley and Sons, Inc.

Kalnay, E., Kistler, M. K. R., Collins, W., Deaven, D., Gandin, L., Iredell, M., Saha, S., White, G., Woollen, J., Zhu, Y., Chelliah, M., Ebisuzaki, W., Higgins, W., Janowiak, J., Mo, K., Ropelewski, C., Wang, J., Leetmaa, A., Reynolds, R., Jenne, R., and Joseph, D., 1996: The NCEP/NCAR 40-year reanalysis project. *Bull. Amer. Met. Soc.*, **77**(3), 437–471.

Karl, D. M., and Lukas, R., 1996: The Hawaii Ocean Time-series (HOT) program: Background, rationale and field implementation. *Deep-Sea Res. Pt. II*, **43**(1–2), 129–156.

Kim, Y., Qu, T., Jensen, T., Miyama, T., Mitsudera, H., Kang, H.-W., and Ishida, A., 2004: Seasonal and interannual variations of the North Equatorial Current bifurcation in a high-resolution OGCM. *J. Geophys.Res.*, **109**, C03040. doi: 10.1029/2003JC002013.

Köhl, A., Stammer, D., and Cornuelle, B., 2007: Interannual to Decadal Changes in the ECCO Global Synthesis. *J. Phys. Oceanogr.*, **37**(2), 313–337.

Levitus, S., Antonov, J., and Boyer, T., 2005: Warming of the world ocean, 1955–2003. *Geophys. Res. Lett.*, **32**, L02604. doi:10.1029/2004GL021592.

Levitus, S., and Boyer, T. P., 1994: Temperatures. Vol. 4, World Ocean Atlas 1994,. *NOAA Atlas NESDIS*, 117 pp.

Levitus, S., Burgett, R., and Boyer, T. P., 1994: Salinity. Vol. 3, World Ocean Atlas 1994,. *NOAA Atlas NESDIS*, 99 pp.

Lorenz, E. N., 1956: *Empirical orthogonal functions and statistical weather prediction.* Cambridge: Massachusetts Institute of Technology.

Mantua, N., Hare, S., Zhang, Y., Wallace, J., and Francis, R., 1997: A Pacific Interdecadal Climate Oscillation with Impacts on Salmon Production. *Bull. Am. Meteorol. Soc.*, **78**, 1069–1079.

McGowan, J., Cayan, D., and Dorman, L., 1998: Climate-Ocean Variability and Ecosystem Response in the Northeast Pacific. *Science*, **281**, 210–217.

Musgrave, D., Weingartner, T., and Royer, T., 1992: Circulation and Hydrography in the Northwestern Gulf of Alaska. *Deep Sea Res.*, **39**(9), 1499–1519.

Pierce, D. W., Barnett, T. P., Tokmakian, R., Semtner, A., Maltrud, M., Lysne, J., and Craig, A., 2004: The ACPI project, element 1: Initializing a coupled climate model from observed conditions. *Climatic Change*, **62**(1–3), 13–28.

Ponte, R., Quinn, K., Wunsch, C., and Heimbach, P., 2007: A comparison of model and GRACE estimates of the large-scale seasonal cycle in ocean bottom pressure. *Geophys. Res. Lett.*, **34**(9), L09603.

Reed, R. K., 1984: Flow of the Alaskan Stream and its Variation. *Deep-Sea Res.*, **31**(4), 369–386.

Roemmich, D., Gilson, J., Cornuelle, B., and Weller, R., 2001: Mean and Time-varying Meridional Transport of Heat at the Tropical/Subtropical Boundary of the North Pacific Ocean. *J. Geophys.Res.*, **106**(C5), 8957–8970.

Royer, T. C., 1998: *Coastal Processes in the Northeast North Pacific*, chapter 13, 395–414. John Wiley and Sons, Inc.

Smith, S., Legler, D., and Verzone, K., 2001: Quantifying Uncertainties in NCEP Reanalyses Using High-Quality Research Vessel Observations. *J. Climate*, **14**, 4062–4072.

Stammer, D., Ueyoshi, K., Köhl, A., Large, W. B., Josey, S., and Wunsch, C., 2004: Estimating Air-Sea Fluxes of Heat, Freshwater, and Momentum Through Global Ocean Data Assimilation. *J. Geophys.Res.*, **109**(C9), C05023. doi: 10.1029/2003JC002082.

Stammer, D., Wunsch, C., Fukumori, I., and Marshall, J., 2002a: State Estimation Improves Prospects for Ocean Research. *EOS Trans. Amer. Geophys. Union*, **83**(27), 289–295.

Stammer, D., Wunsch, C., Giering, R., Eckert, C., Heimbach, P., Marotzke, J., Adcroft, A., Hill, C. N., and Marshall, J., 2002b: The Global Ocean Circulation During 1992–1997, Estimated From Ocean Observations and a General Circulation Model. *J. Geophys.Res.*, **107**(C9), 3118. doi:10.1029/2001JC000888.

Stammer, D., Wunsch, C., Giering, R., Eckert, C., Heimbach, P., Marotzke, J., Adcroft, A., Hill, C. N., and Marshall, J., 2003: Volume, Heat and Freshwater Transports of the Global Ocean Circulation 1993–2000, Estimated from a General Circulation Model Constrained by WOCE Data. *J. Geophys.Res.*, **108**(C9), 3007. doi:10.1029/2001JC001115.

Tabata, S., Thomas, B., and Ramsden, D., 1986: Annual and Interannual Variability of Steric Sea Level along Line P in the Northeast Pacific Ocean. *J. Phys. Oceanogr.*, **16**, 1378–1398.

Trenberth, K., and Shea, D., 1987: On the evolution of the Southern Oscillation. *Mon. Weather Rev.*, **115**, 3078–3096.

Wang, Y., Jan, S., and Wang, D., 2003: Transports and Tidal Current Estimates in the Taiwan Strait from shipboard ADCP observations (1999-2001). *Estuar. Coast. Shelf S.*, **57**, 193–199.

Whitney, F., and Freeland, H., 1999: Variability in Upper-Ocean Properties in the N. E. Pacific Ocean. *Deep-Sea Res. II*, **46**(11-12), 2351–2370.

Wijffels, S., Firing, E., and Bryden, H., 1994: Direct Observations of the Ekman Balance at 10°N in the Pacific. *J. Phys. Oceanogr.*, **24**, 1666–1679.

Wijffels, S., Willis, J., Domingues, C., Barker, P., White, N., Gronell, A., Ridgway, K., and Church, J., ????: Changing eXpendable Bathythermograph Fall-rates and their Impact on Estimates of Thermosteric Sea Level Rise. Submitted.

Willis, J. K., Roemmich, D., and Cornuelle, B., 2004: Interannual variability in upper-ocean heat content, temperature, and thermosteric expansion on global scales. *J. Geophys.Res.*, **109**, C12036. doi:10.1029/2003JC002260.

Wunsch, C., 1978: The North Atlantic General Circulation West of 50^o W Determined by Inverse Methods. *Rev. Geophys. Space GE*, **16**(4), 583–620.

Wunsch, C., and Heimbach, P., 2007: Practical global oceanic state estimation. *Physica D*, **230**(1–2), 197–208.